Self-assembly of Intrinsically Disordered Peptide Amphiphiles

Tamara Ehm

Munich 2023

Self-assembly of Intrinsically Disordered Peptide Amphiphiles

Tamara Ehm

Dissertation as a cotutelle agreement

handed in to the deanship of the Faculty of Physics

of the Ludwig-Maximilians-Universität and

to the Senate of Tel Aviv University

The work was carried out under the supervision of

Prof. Dr. Roy Beck-Barkai and

Prof. Dr. Joachim O. Rädler

Tamara Ehm

Submitted on 29th of June 2022 to the deanship of LMU in Munich

and sent for submission to the senate of Tel Aviv University in Tel Aviv

Selbstorganisation von Intrinsisch Ungeordneten Peptidamphiphilen

Tamara Ehm

Dissertation

an der Fakultät für Physik

der Ludwig-Maximilians-Universität

München

vorgelegt von

Tamara Ehm

aus München

München, den 29.06.2022

Information for defense at LMU:

Erstgutachter: Prof. Dr. Joachim O. Rädler

Zweitgutachter: Prof. Dr. Roy Beck-Barkai

Tag der mündlichen Prüfung: 10.8.2022

Contents

Abstract

Intrinsically disordered peptide amphiphiles (IDPAs) are a novel class of molecules with great potential if incorporated into nanocarriers. IDPAs combine hydrocarbon chains that originate from natural lipids and polypeptide chains composed of sequences that do not fold into a static structure but remain intrinsically disordered, fluctuating between various conformations. This amphiphilic structure makes IDPA self-assemble into mesophases or aggregates in solution. The possible sequence variations are vast, and their influence on the self-assembly structures has hardly been explored. In my Ph.D., I studied how to decode the impact on sequence composition and conformation and provide the basis for future applications and implementations of IDPAs. I worked on four different IDPAs that differ in their amino acid sequences. We used SAXS, TEM, and turbidity measurements to analyze the nanoscopic self-assembled structures. We showed that permutations and the sequence's charge pattern remarkably alter the headgroup's conformation. Consequently, pH-dependent phase transitions between spherical, cylindrical micelles and condensed hexagonal phases are related to the sequence variation. We demonstrated that even a single amino acid mutation could tune the phase transition. Last, we showed that our system should phase transition for IDPAs that can be enzymatically cleaved. Altogether, we demonstrated that IDPAs enable many applications for lipid nanoparticle systems to add multiple functionalities by incorporating IDPAs with desired properties. For most experiments, I used small-angle X-ray scattering (SAXS). To enable measurement under multiple conditions with ONE single probe, we developed a 3D printed sample chamber made of cyclic olefin copolymers (COC), including COC X-ray windows providing ultra-low SAXS background. The chamber's design enables both in-situ buffer exchange

and optical transmission spectroscopy. It is thus suitable for many more applications. The design consists of a membrane insert for in-situ dialysis of the 100 μl sample volume against a reservoir. We demonstrated the chamber used by measuring our IDPA system at various pHs and polymer systems as a function of salt concentration. Our chamber's design makes in-situ measurements at in-house sources possible. This design is proved useful and is in regular use in our lab at LMU for pH-dependent experiments. In my Ph.D. project, I studied the self-assembly of tunable IDPA and their properties under various environmental conditions. We developed a 3D printed chamber for in-situ dialysis to measure these conditions on one probe.

Abstract in German

Zusammenfassung

Intrinsisch ungeordnete Peptidamphiphile (IDPAs) sind eine neue Art von Molekülen und haben großes Potenzial als Bestandteile von Nanopartikeln eingesetzt zu werden. IDPAs kombinieren Kohlenwasserstoffketten und Polypeptidketten. Die Peptide bestehen aus Aminosäuresequenzen, die sich nicht zu einer statischen Struktur falten, sondern in sich ungeordnet bleiben und zwischen verschiedenen Konformationen fluktuieren. Aufgrund dieser amphiphilen Struktur können sich IDPAs in Lösung selbst zu Mesophasen oder Aggregaten assemblieren. Die möglichen Sequenzvariationen sind enorm, und ihr Einfluss auf die Selbstorganisationsstrukturen ist kaum erforscht.

In meiner Doktorarbeit untersuchte ich, wie die Auswirkungen auf die Sequenzzusammensetzung und Konformation entschlüsselt werden können, um eine Grundlage für zukünftige Anwendungen und Implementierungen von IDPAs zu schaffen. Ich habe an vier verschiedenen IDPAs gearbeitet, die sich in ihren Aminosäuresequenzen unterscheiden. Wir verwendeten Kleinwinkelröntgenstreuung (SAXS), TEM und Transmissionsmessungen, um die nanoskopischen, selbstorganisierten Strukturen zu analysieren. Wir konnten zeigen, dass Permutationen und das Ladungsmuster der Sequenz die Konformation der Kopfgruppe erheblich verändern. Folglich sind pH-abhängige Phasenübergänge zwischen sphärischen, zylindrischen Mizellen und kondensierten hexagonalen Phasen mit der Sequenzvariation verbunden. Wir konnten nachweisen, dass sogar eine einzige Aminosäuremutation den Phasenübergang beeinflussen kann. Schließlich haben wir gezeigt, dass unser System für IDPAs, die enzymatisch gespalten werden können, einen Phasenübergang er-

möglicht. Insgesamt konnten wir zeigen, dass IDPAs viele Anwendungen für Lipid-Nanopartikelsysteme ermöglichen, wenn gewünschte Eigenschaften in die Sequenz eingebaut werden.

Für die meisten Experimente habe ich SAXS verwendet. Um Messungen unter verschiedenen Bedingungen mit EINER einzigen Probe zu ermöglichen, entwickelten wir eine 3D-gedruckte Probenkammer aus zyklischen Olefin-Copolymeren (COC), einschließlich COC-Röntgenfenstern, die einen extrem niedrigen SAXS Hintergrund haben. Das Design der Kammer ermöglicht sowohl den In-situ-Pufferaustausch als auch die optische Transmissionsspektroskopie. Sie ist daher für viele weitere Anwendungen geeignet. Das Design besteht aus einem Membraneinsatz für die In-situ-Dialyse des 100 μl großen Probenvolumens gegen ein Reservoir. Wir haben die Kammer getestet, indem wir unser IDPA-System bei verschiedenen pH-Werten und Polymersystemen in Abhängigkeit von der Salzkonzentration gemessen haben. Unsere Kammer wird inzwischen in unserem Labor an der LMU regelmäßig für pH-abhängige Experimente verwendet.

In meinem Promotionsprojekt untersuchte ich die Selbstorganisation von IDPAs und ihre Eigenschaften unter verschiedenen Umweltbedingungen. Wir haben eine 3D-gedruckte Kammer für die In-situ-Dialyse entwickelt, um unter verschiedenen Bedingungen mit einer Probe messen zu können.

Chapter 1

Introduction

"Science is not a boy's game, it's not a girl's game. It's everyone's game. It's about where we are and where we're going." Nichelle Nichols

1.1 Proteins

Proteins are a cornerstone of life through their various functions in organisms. They support the metabolism by providing structural support and acting as enzymes, carriers, and hormones. In the 19th century, researchers believed that one substance was the essence of all proteins. That explains the origin of the word "protein" - in old greek, "proteios" for "fundamental" and "priority." In 1902 it was shown proteinogenic amino acids are the building blocks of proteins [1]. Amino acid chains can be two or more than 1000 amino acids long (Fig. 1.1) [1].

Proteins are nature's machines within the cells. Before a cell expresses a protein, the genetic code on the DNA is transcribed into RNA with DNA polymerases. The RNA is then spliced, and non-coding sequences are eliminated. Next, the RNA is transferred into the cytosol and transcribed into amino acids chain by the Ribosome. Here, the combination of 3 nucleotides encodes for one amino acid. The amino acids are joined by peptide bonds and then form small peptides or larger proteins (Fig. 1.2). Proteins can be modified after translation by adding small molecules like phosphate groups. This posttranslational modification often happens at the endoplasmatic

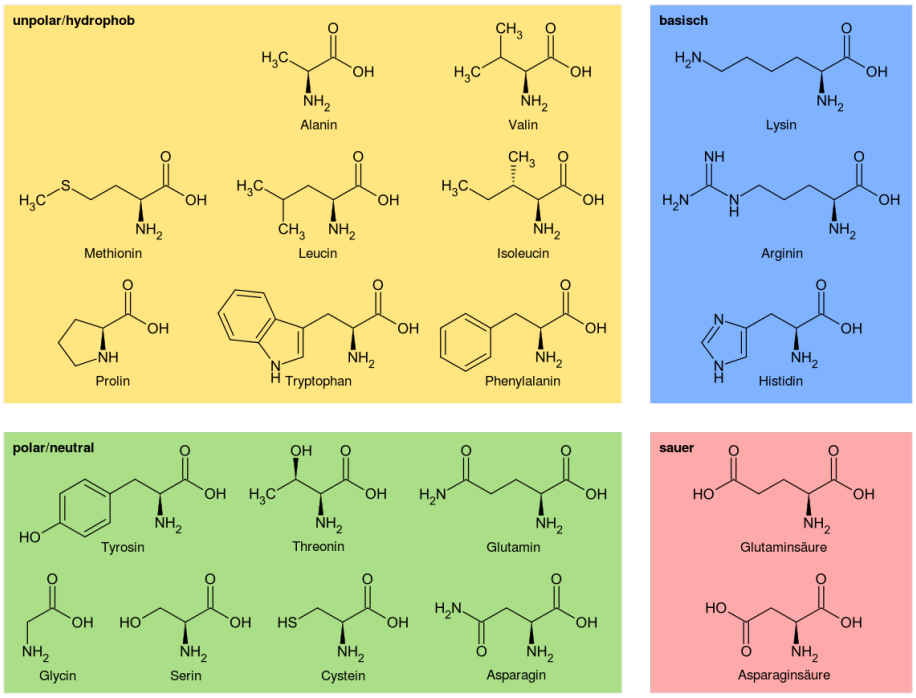

Figure 1.1: **Chemical structure of amino acids.** Amino acids can be classified by their charge at physiological *p*H (neutral, positive, negative) and hydrophobicity. Figure free from copyright.

reticulum or the Golgi apparatus [1].

Precisely 20 years after the finding the building blocks of proteins, a Danish scientist, Kaj Ulrik Linderstrøm-Lang, explained the concept of protein secondary structure for the first time [2]. The two most common secondary structural elements are α-helices and β-sheets. They are maintained by the pattern of hydrogen bonds between the amino hydrogen and carboxyl oxygen atoms in the peptide backbone. One way of analyzing the peptide backbone is the so called Ramachandran diagram, developed in 1963 by G. N. Ramachandran, C. Ramakrishnan, and V. Sasisekharan. Here the energetically allowed regions for backbone dihedral angles are visualized (Fig. 1.3a). There are typical diffuse locations on the two-dimensional plot for α-helices and β-sheets (Fig. 1.3b) [3,4].

Groups of amino acids, partially or fully in secondary structures, can form tertiary structures; there are four types of tertiary interactions: hydrophobic interactions, hydrogen bonds, salt bridges, and sulfur-sulfur covalent bonds [5]. If subunits are packed into a macromolecular arrangement, we can call this a quaternary structure(Fig. 1.4). For a a lot of proteins the structure directly encodes

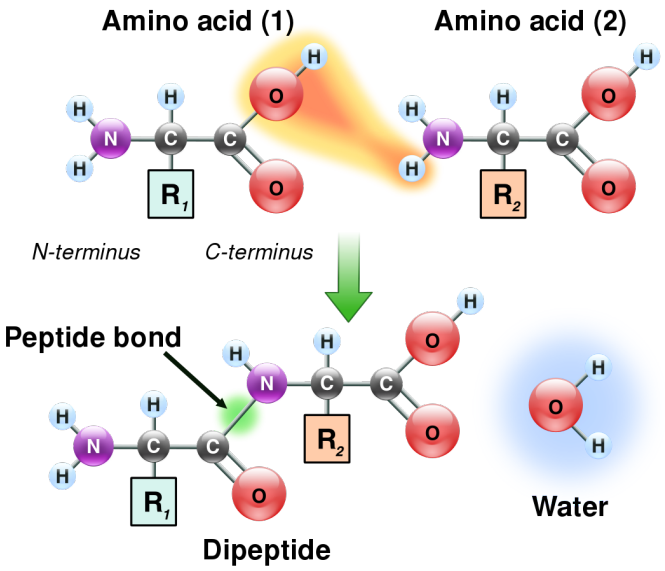

Figure 1.2: **Peptide Bond Formation.** In the condensation reaction, amine and carboxylic acid groups of adjacent amino acids form a peptide bond by creating one water molecule. Figure free from copyright.

functions: this is called the conventional sequence structure function paradigm.

One prominent example is Hemoglobin consisting of two pairs of subunits, an α- and a β-chain, each consisting of 141 and 146 amino acids, respectively. All units are bound together by hydrophobic interactions, hydrogen bonding, and ion pairs between oppositely charged amino acid side chains. Each unit can bind one O_2 molecule, whereas upon binding the conformation of the other subunits changes, causing an allosteric effect (Fig. 1.5) [6]. The Hemoglobin is an example demonstrating how protein's functionality is linked to structural rearrangement due to binding to additional factor.

In addition, proteins conformation and function can occur due to alteration in the environmental conditions. As some amino acids can get (de)protonated with changing pH, their attraction/repulsion to other amino acids (groups) can change. Such a change in the attraction/repulsion between the amino-acids can thus lead to macroscopic conformational changes. This often small change can drastically alter the (enzymatic) behavior of the protein and thus significantly impact the protein [6]. For example, light can change the conformation of photoresponsive chemical groups that undergo cis/trans isomerization [8].

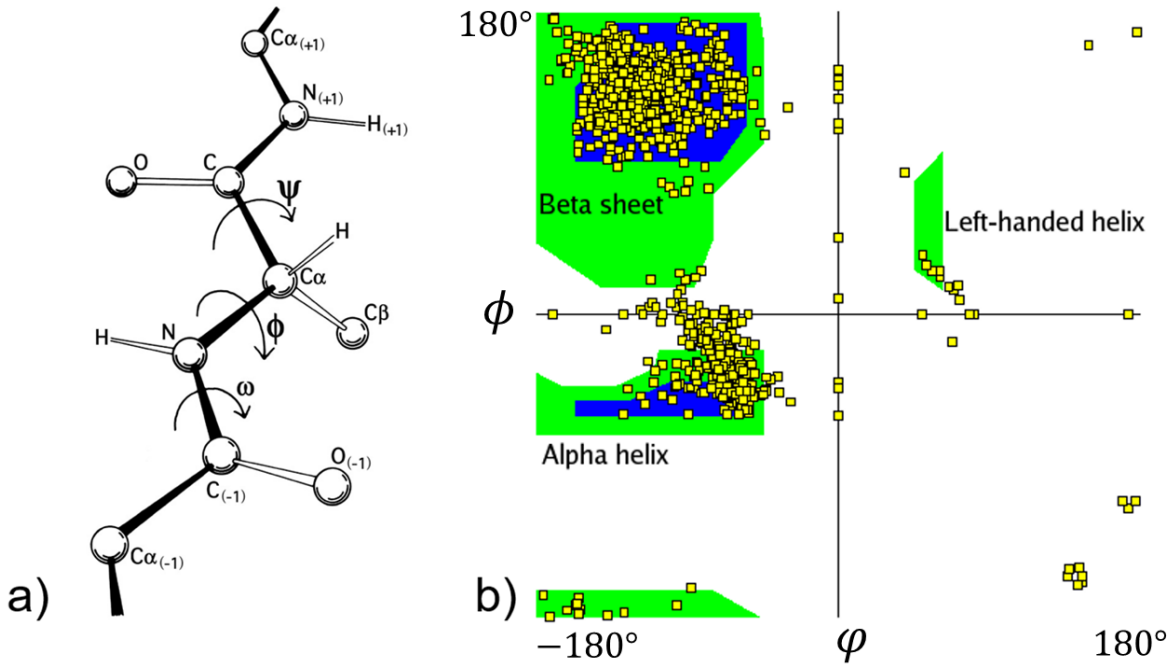

Figure 1.3: **Ramachandran digram.** a) Backbone dihedral angles, figure by Dcrjsr 2011, figure used with permission under license CC BY-SA 4.0. b) Typical Ramachandran diagram for secondary structures, figure by Opabinia regalis 2006, figure used with permission under license CC BY-SA 4.0.

1.2 Intrinsically disordered proteins

Intrinsically disordered proteins (IDPs) violate the conventional sequence structure function paradigm, since they have amino acid sequences that do not lead to singular, stable 3D structures[1]. The rate at which IDPs are discovered and characterized continues to increase, constituting the fastest-growing area of proteomics [10–12].

IDPs' essential elements are intrinsically disordered peptide regions, which show structural flexibility and plasticity [13, 14] (Fig.1.7). IDPs spontaneously fluctuate between many conformations in their native form. Remarkably, the disorder does not lead to dysfunction as with denatured folded proteins. In fact, unlike denatured proteins, recent evidence strongly suggests that multiple biological functions stem from such structural plasticity. Proteins with intrinsically disordered regions are involved in a range of cellular functions, including transcription, translation, signaling, and regulation of protein assembly [15]. The lack of a secondary ordered structure suggests poly-

[1]The content of this introductory part is based on our recently published review article in Ref. [9].

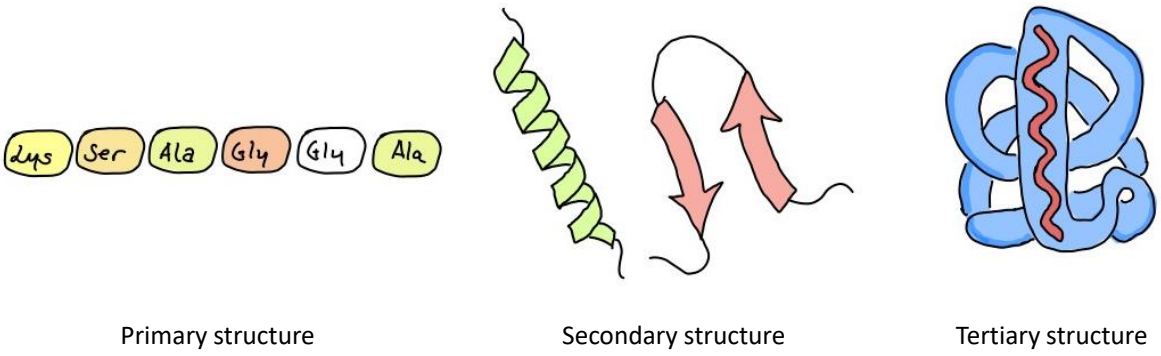

Figure 1.4: **Conventional protein structures.** Amino acids chain form primary structures. Secondary structures are formed by α-helices and β-sheets. Tertiary interactions can be hydrophobic interactions, hydrogen bonds, salt bridges, and sulfur-sulfur covalent bonds.

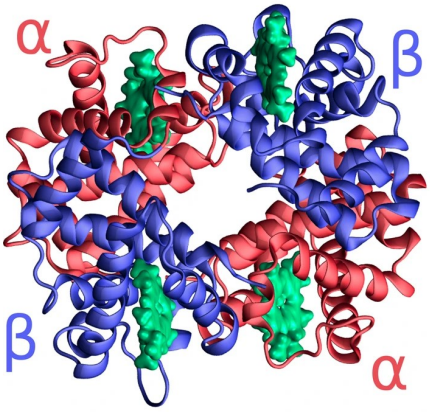

Figure 1.5: **Haemoglobin structure.** Molecule consists of 2 α-chains (red) and 2 β-chains (blue) with 4 heme groups (green), each capable of binding one $_2$ molecule. Figure is adapted with permission from Ref. [7], licensed under CC BY 4.0.

meric types of interactions with weak local electrostatic or hydrophilic interactions, which are yet poorly understood [16].

Prostate-associated gene 4 (PAGE4) is an example for an IDP benefiting from its structural plasticity. PAGE4 is implicated in human prostate cancer. Several computational and experimental analysis suggest that PAGE4 is expected to be highly disordered but possess several regions with a somewhat increased propensity to order. Therefore, PAGE4 disorder is not complete randomness, known from polymer physics models as random walks in 3D space without any structural preferences. The disorder rather shows a diversity of metastable states that can be stabilized by binding

to interaction partners. For PAGE4, these binding partners are, for example, protein kinases that phosphorylate amino acids of PAGE4. The phosphorylation results in an increase or decrease of the protein's compactness depending on the phosphorylation site. Thus PAGE4, and other IDPs, undergo conformational changes upon interacting with relevant binding partners and accordingly alter their functionality [17].

The intrinsically disordered regions provide a significant functional advantage for IDPs, enabling them to interact with a broad range of binding partners [18, 19]. For example, the protein-protein interaction network of Saccharomyces cerevisiae, a species of yeast, has many interaction partners. It is indicated that besides repeated domains, long disordered regions, which are common in date hubs, are critical for flexible binding [20].

What amino acids make IDPs?

Several conserved motifs are known to induce secondary structures, while other amino acids are primarily found in disordered regions [21]. In general, we can determine "order-promoting" (cysteine, tryptophan, tyrosine, isoleucine, phenylalanine, valine, leucine, histidine, threonine, asparagine) and "disorder-promoting" residues (aspartic acid, methionine, lysine, arginine, serine, glutamine, proline, glutamic acid) [22]. This classification fits to the current pictures of highly dynamic structures of IDPs that do not form stable hydrophobic cores and expose most of their amino acids to the solvent. In addition, proline plays a unique role. Because of its chemical structure proline does not contain a backbone amide hydrogen atoms at physiological pH and therefore does not form stabilizing hydrogen bonds in α-helices, or β-sheets. Thus, proline is commonly found at the end of α-helices or in loop regions, rather than in middle of secondary structures [21].

But what makes an IDP an IDP?

To explain what makes an IDP and IDP, we can ask ourselves the other way around: what makes proteins fold? The answer to the latter lies in the interaction of amino acids with their aqueous surrounding and neighbouring residues. Apolar, hydrophobic amino acids are prone to avoid the

contact with water molecules and will rather collapse to a structure. On the other side, polar, charged and hydrophilic residues tend to present themselves on the outside of the protein structure (Fig. 1.6, and Refs. [23–28]). Uversky et. al. presented an empirical evidence showing that IDPs are charged and hydrophilic (Fig. 1.6a). Supporting this view is the comparison between the occurrence of the 20 proteogenic amino acids in disordered and ordered proteins from protein databases. Using the PDB and DisProt for the relevant databases, it was shown that most of the charged and polar amino acids occur in disordered polypeptide regions (Fig. 1.6b).

Unlike structured proteins, IDPs lack secondary, tertiary, or quarternary structures. Thus, their backbone conformations are heterogeneous in space, and in the Ramachandra diagram, the typical plots are shifting. So far, no statistical mapping of the available Ramachandran space of each amino acid in terms of conformational propensity and thus induction of disorder was shown [29].

We can distinguish between three classes of IDP compositional classes: polar, polyampholytes, and polyelectrolytes [30, 31]. All classes of IDPs are rather hydrophilic and made out of polar or charged amino acids (Fig. 1.6). Polar IDPs lack charged, hydrophobic, and proline residues, but contain polar amino acids. While polyelectrolytes have an excess of one type of charge, polyampholytes have roughly equivalent fractions of opposite charges. Both can be either weak or strong depending on the fraction of charged residues: $(\text{Glu-Lys})_{25}$ is a strong synthetic polyampholytic IDP while the disordered region of the catecholamine sulfotransferase, DP00011, is rather a weak polyampholytic IDP [32]. The degree of expression of the polyelectrolytes/ polyampholytes, of course, goes with their solubility and their tendency to interact with binding partners [30].

What makes IDPs special?

Lots of structured protein are understood to follow the "lock-and-key" principle whereas one enzyme fits exactly to a receptor region. Structural proteins are keys that fit to one lock, while IDPs serve as "master-keys" than can open multiple locks [18]. This concept can be understood as the following: the classical structure-function paradigm tells us that there is well defined Enzyme-substrate complex in 3D space, where the enzyme is a rather rigid negative of the substrate (Fig.

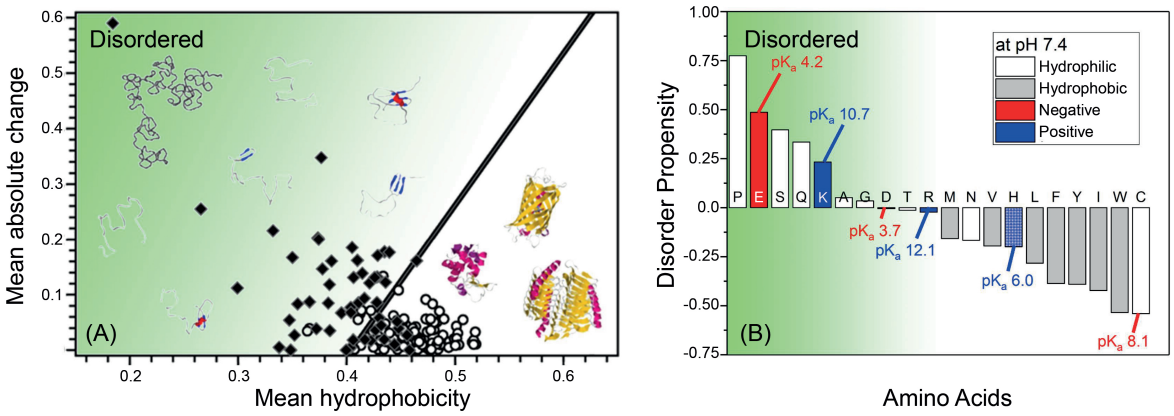

Figure 1.6: **The role of charge, hydrophobicity and amino acid residue in IDPs.** (A) Nearly 250 folded (the open circles) and nearly 90 natively unfolded proteins (the black diamonds) demonstrate that IDPs are charged and hydrophilic. The solid line sets an illustrative border between IDPs and compact globular proteins. The y-axis shows the summed charges over all amino acids of the protein. (B) The contribution of each amino acid in promoting disorder. Disordered propensity is evaluated from the fractional difference of amino acids composition of IDPs in the DisProt database and a completely ordered proteins from the protein-database (PDB). Figure is from our open access review in Ref. [9].

1.7. In contrast, the "induced-fit" model based on the observations that some enzymes could act on differently shaped substrates [33] can be applied to IDPs [34]. Thus, unlike structural proteins, IDPs can interact with multiple binding partners. Importantly, in many cases the interaction of IDPs with another molecule indicates a order-to-disorder transition of a specific motif.

An example is binding of the the KIX domain of a general transcriptional coactivator CREB-binding protein (CBP) with intrinsically disordered phosphorylated kinase-inducible (pKI) domain of the cAMP-response element binding (CREB) protein. This process involves conformational selection and the induced fit mechanism. The binding mechanism of KIX to pKI was compared to another to transcirption factor (c-Myb), interacts with KIX at the same site as pKI domian but via a different binding mechanism that involves elements of conformational selection and induced fit [35].

Another essential feature of IDPs is their prevalence as flexible linkers. In Calmodulin (CaM), which serves for extracellularly induced Ca^{2+} signaling within the cytosol, there is a disordered re-

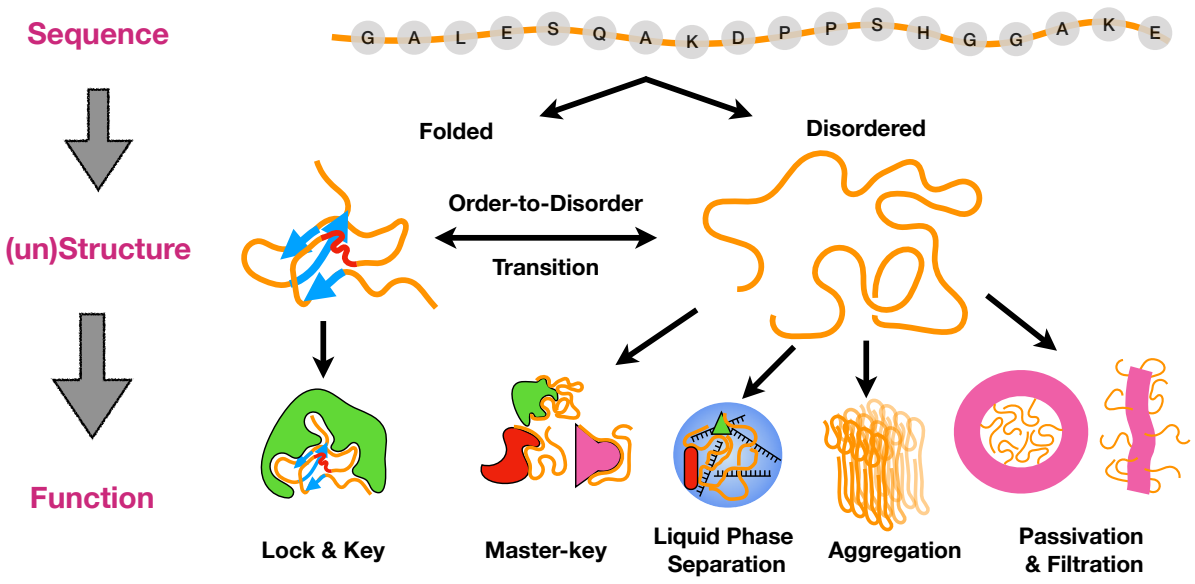

Figure 1.7: **Contemporary sequence-function paradigm.** The folded and disordered conformations, and the transition between the two, lead to biological function. The figure is adapted from our open access review in Ref. [9]

gion as a hinge-like in a helical linker between the two main domains. The X-ray crystal structure of CaM is dumbbell-like with two homologous globular domains. The disordered hinge can facilitate binding. The flexible domain allows additional interaction confirmation as the molecular can sample through various conformations relative to the binding surface. After binding, the flexible linker allows multiple separations of the two domains [36].

How can we characterize IDPs?

In contrast to structural proteins that show one minimum in the energy landscape and therefore appear in one conformational state in a specific environment, IDPs show a multi funnel structure for the energy landscape. These competing low-energy structures result not in a singular structure but rather in an average of possible dimensions and population of the ensemble of conformations [37]. Thus, X-ray crystallography as the standard technique to determine protein structure is not appropriate for studying IDP structures.

NMR spectroscopy, in contrast, can determine IDP dynamics and structure [38] by probing conformational preferences at residue level. But the hydrogen chemical shift signal used in traditional

NMR is, in many cases, insufficient the signal-to-noise ratio for IDP characterization. Alternativliy techniques, such as paramagnetic relaxation enhancement (PRE) [39] offer new alternatives to charachterize IDP structures due to its improved signal-to-noise ratio.

In PRE, paramagnetic spin labels are added to proteins. This affects the chemical shift and the transverse relaxation rate signal between the unpaired electron and NMR active nuclei on the basis of the distance between them [39]. For example, the PRE signal and ^{15}N relaxation data were analyzed to quantify the interaction between the IDP osteopontin and heparin [40]. When heparin binds, osteopontin largely remains in a disordered state and undergoes structural/dynamical adaption which is mainly mediated by electrostatic interactions.

In addition to NMR, small-angle X-ray scattering (SAXS) can report three-dimensional space sampled by disordered states. Therefore combining NMR and SAXS is beneficial to get a complete overview of IDP structure and conformation.

Also computer simulations can analyse disorder based on the amino acid sequence. [41]. One prominent example for computer analysis is Iupred [42]. Here the energy resulting from inter-residue interactions from the local amino acid compositions are calculated to predict if regions do have a well-defined 3D structure under native conditions. RONN is an AI based alternative to Iupred and uses neural network trained on disordered proteins. None of the available methods for disorder prediction can be taken as fully reliable on its own, so it is always beneficial to use an appropriate combination of methods [41]. A detailed overview of some of these techniques used in this thesis is given in the methods section 2.5.2.

Additionally to techniques that analyze each amino acid's propensity to induce disorder, some databases use known sequences. The disordered protein database (Disport) and the crystal protein database (PDB) are examples. These platforms give an overview of known IDP regions [21] and their occurrence in disordered proteins.

Where does IDPs' plasticity play a role?

IDPs, by definition, fluctuate between a large ensemble of possible conformations [13, 27, 36, 43, 44]. Importantly, due to their plasticity the strength of interaction is limited: if the interaction is larger than the thermal energy of the IDPs it would force them to a specific conformation and basically "destroy" their disorders.

But the plasticity enables features that ordered proteins cannot provide. Thus IDPs can trigger various pathways in biology: IDPs play a central role in the ordered assembly of macromolecular machines such as the ribosome. Additionally they are part of the organization of chromatin, of the assembly and disassembly of microfilaments and microtubules, of transport through the nuclear pore, in binding and transport of small molecules and in functioning of protein and RNA chaperones [45]. IDPs can also serve as flexible "entropic" linkers that separate functional protein domains [45–49](Fig. 1.7.

One important class of molecules with a high proportion of disordered regions are cytoskeleton proteins, including neurofilament (NF) proteins, α-internexin, vimentin, microtubule-associated protein 2 (MAP2), and tau [23, 50–54]. Here, disordered regions promote assembly of the proteins in a hydrogel network [23, 54, 55]. The structure and size of the hydrogel influences the mechanics of axons and has a direct effects on the electrical conduction [51, 54, 56–58].

Additionally, IDPs can regulate protein-protein/DNA networks or the transition to an ordered structure as a response to an external stimuli, e.g, an enzyme [9, 59, 60]. IDPs cannot just trigger biological functionality upon binding but also be fictionalized themselves with disorder-to-order transition [61].

An example is the regulation of glucose homeostasis by human pancreatic glucokinase (GCK) enzyme. GCK itself has a disordered region that can associate with glucose at high glucose concentration and undergoes a disordered-to-ordered transition and vice versa at low glucose concentration. This disorder transition shapes the kinetic cooperativity of the enzyme, dependent on the local concentration of glucose [62] (see Fig. 1.8 for detailed process).

Last, IDPs can drive liquid-liquid phase separation between mostly IDPs and RNA in membrane-

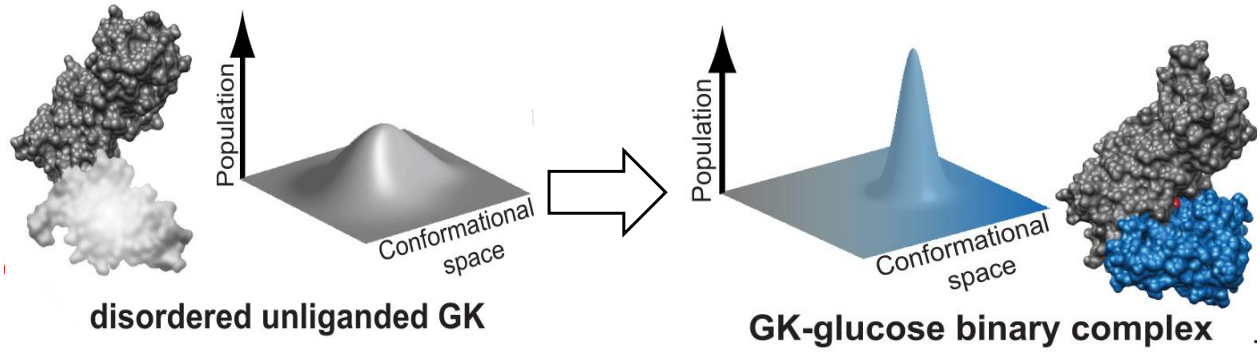

Figure 1.8: **Mechanism of GCK disorder to order transition.** a) GCK is a disordered protein, having multiple conformational ensembles as shown in the flat energy landscape. b) If a glucose/activator binds, a order-disorder transition for GCK's disordered region is promoted. This results in narrowing of conformational distribution. Figure is adapted with permission from Ref. [62] under CC BY license.

less organelles [44, 47, 63]. This mechanism is poorly understood, but it often contains multiple repetitive sequences, facilitating multivalent, weak interactions with their partners to form the condensates; as mentioned before, such interactions are typical for IDPs.

Which role do IPDs play in diseases?

Structural plasticity confers relevant biological function to IDPs - and dysfunction when mutations are present. In fact almost half of the proteins associated with diseases are disordered (Fig. 1.9). Mutations in disordered regions can result in numerous diseases - e.g., Alzheimer's and Parkinson's. Here, associated proteins, Amyloid-β, and α-synuclein can form toxic oligomers, amyloid fibrils, and other types of aggregates [64, 65]. Also, in diseases, signaling of disordered regions can play a role, as in the recently emerged coronavirus (SARS-CoV-19). A disordered region in the nucleocapsid is encoded in the genome. This region is essential to bind to the RNA and can interact with several proteins [66, 67] (Fig. 1.10).

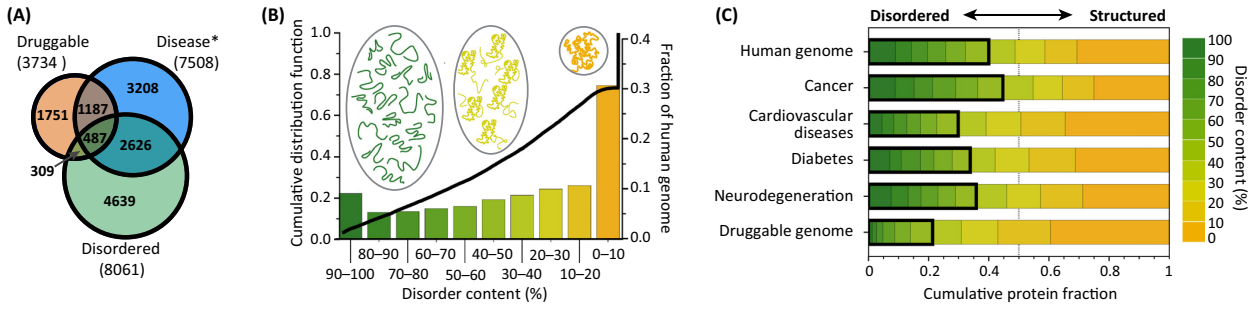

Figure 1.9: Disordered proteins link to human diseases. (A) Venn diagram of three types of proteins: those that interact with drugs; those that are related to disease; and those that are disordered. (B) The fraction of humans proteins encoded by the human genome (right axis) binned according to their content of structural disorder. The black line is the cumulative distribution function (left axis). (C) Amount of disorder in different protein categories. The figure is from our open access review in Ref. [9].

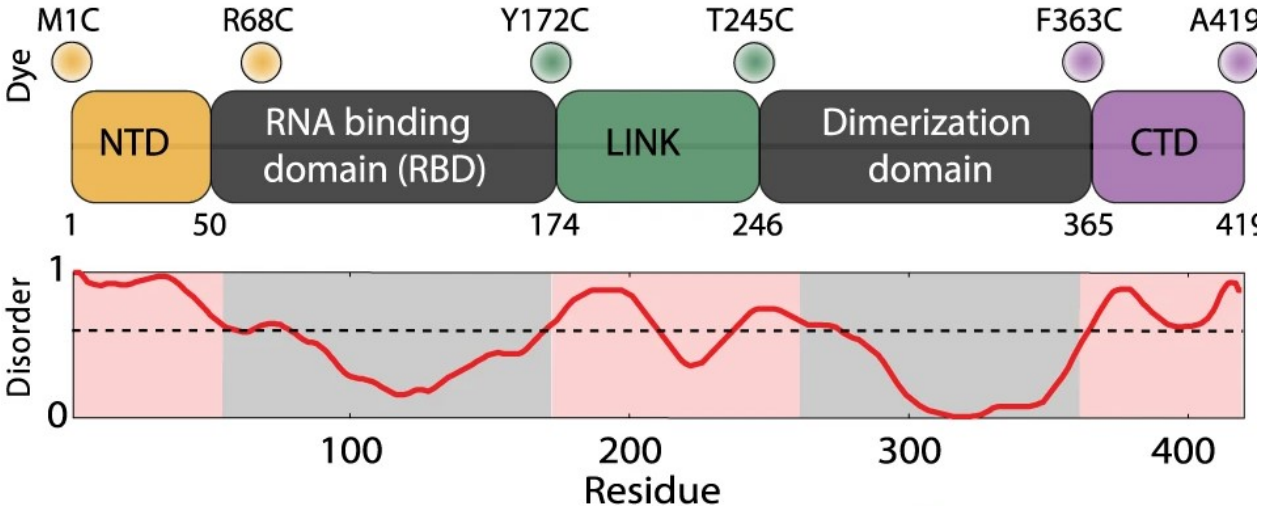

Figure 1.10: **Disordered regions of the SARS-CoV-2 N protein.** Disorder analysis was done with IUPred2A by the authors. Protein–protein and protein–RNA interaction are predicted for the three disordered regions. Figure is adapted with permission from Ref. [67] under license CC BY 4.0.

Can we engineer IDPs?

IDPs play a significant role in various biological signaling processes, and their engagement often results in phase transitions [68, 69]. Thus, changing the IDP sequence can result in the different physical behavior of the phase change and be engineered to the experimenters' needs. IDPs make versatile building blocks in the design of supramolecular self-assembling biomaterials with a precise control over architecture and functionality.

One of the first experiments that showed this behavior was done with elastin-like polypeptides, which are based on the repeating sequence of tropoelastin. Here, the choice of molecular building blocks determines their self-organization into higher-ordered structures like cylinders or micelles and networks like fibers or tubes and finally, functionalized macroscopic hydrogels. These structures are not just highly adaptable but also show thermal stability at room temperature. There is a wide range of applications of these hydrogels, ranging from drug delivery to tissue engineering applications [70].

Thus elastin-like polypeptides can be conjugated to functionalized molecules. After injection they form hydrogels and can be activated with an external stimulus, for example with UV light. Recent impressive experiments by the Chilkoti group showed liquid-liquid phase transition of an artificial IDP made of a repetitive octamer peptide sequence originated from Drosophila melanogaster Rec-1 resilin [71]. The phase transition temperature was drastically changed when changing one (!) amino acid or changing the number of repeats. Additionally, they showed that the sequence controls the temperature-ramp hysteresis phenomena: when the sequence is flipped from N- to C-terminal, the temperature ramp is changed [72].

1.3 Peptide Amphiphiles

Amphiphiles are molecules made out of a hydrophobic and a hydrophilic domains. Due to the geometry amphiphiles self-assemble in aqueous solution with the hydrophilic part pointing toward the outside, and the hydrophobic towards the inside of the self-assembled structures. Lipids are the

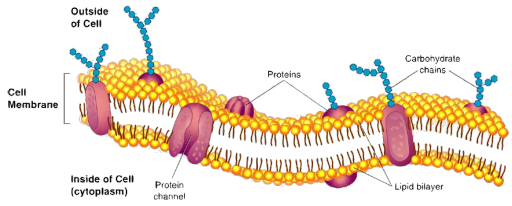

Figure 1.11: **Lipids as part of cell membrane.** Lipids contain hydrophilic head and hydrophobic tail group. Due to the amphiphilic structure lipids can form membranes in solution. Figure free from copyright.

most occurring amphiphile in nature. Due to their amphiphilic structure, lipids play an essential role in any kind of compartment separation in biology, drug design, or cosmetics [73].

In lipids the hydrophobic part is often a double or single chain of hydrocarbons and the hydrophilic group can be any small polar or charged molecule, for example a phosphoric acid diester group or a sphingosin for membrane lipids [74] (Fig. 1.11). Lipids had been the inspiration to design and produce functional synthetic peptide amphiphiles (PAs). Here, the hydrophilic part is a small peptide synthesized to a hydrocarbon chain. The first publication in synthetic PAs by Berndt et. al. in 1995 [75] presented PAs that form a monolayer at the air-water interface. The PAs were This was the start for a wave of new functional molecules.

How do PAs self-assemble?

Due to their amphiphilic nature, PAs are expected to form nanoscopic mesophases in an aqueous solution spontaneously. Their mesoscopic morphology is, to a first approximation, determined by the volumetric ratio of the hydrophilic head group to the hydrophobic tail as described by the so-called packing parameter, $p = \frac{v}{la_0}$, here v is the volume of the core, l the chain length and a_0 the headgroup area. [74] (Fig. 1.12 and 1.13 for illustration) [74].

The hydrocarbon tails are expected to promote the propensity of PAs' self-assembly in aqueous solutions into mesophases (Fig. 1.13). The most common structures for amphiphilic structures reported are dispersed micellar: spherical, elongated worm- and rod-like or condensed structures, including lamellar, hexagonal, cubic, and bi-continuous mesophases. Typical interactions associated with these self-assemblies are Van der Waals bonds, hydrogen bonds, and entropic forces [76–79].

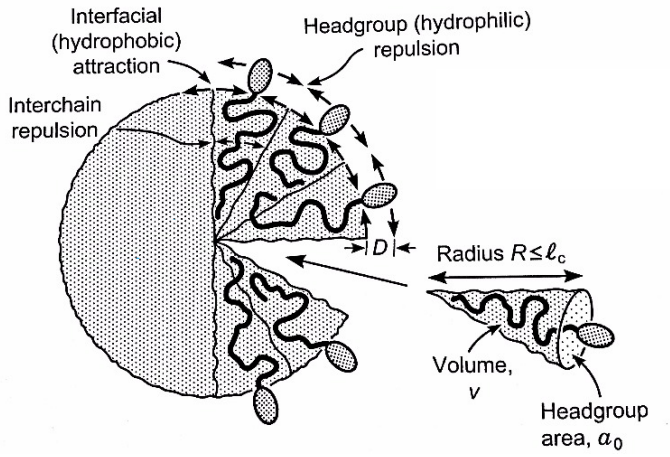

Figure 1.12: **Variables for packing parameter determination.** Packing of lipids aggregates is dependent on the volume of the core, v, the chain length, l and the headgroup area a_0. The major forces that govern the self-assembly are headgroup repulsion, repulsion between the chains and hydrophobic attraction. Adapted figure with permission and content from Israelachvili [74].

What is the typical design of PAs?

Various studies presented self-assembly and applications of peptide amphiphiles (PAs) [77, 79, 81, 82]. For example, Niece et. al. produced a nanofiber by synthesizing differently charged PAs. The PAs self-assemble into nanofibers with a diameter of approximately $7nm$ due to electrostatic interactions [80] (Fig. 1.14). PAs have a very confined hydrophilic and hydrophobic domain, making their design relatively straightforward and providing high solubility in water. Often PAs are made out of 4 structural key entities (Fig. 1.14a): Of course, there is the hydrophobic domain, one or more hydrocarbon chains. Second, there is a short sequence capable of forming intermolecular hydrogen bonding. The third region contains charged amino acids to enhance water solubiliy. For functionality, region four has a reactive sequence that can interact with cells or proteins [79]. PAs can form fibers, ribbons, or aggregates depending on the molecule design and solution conditions [77].

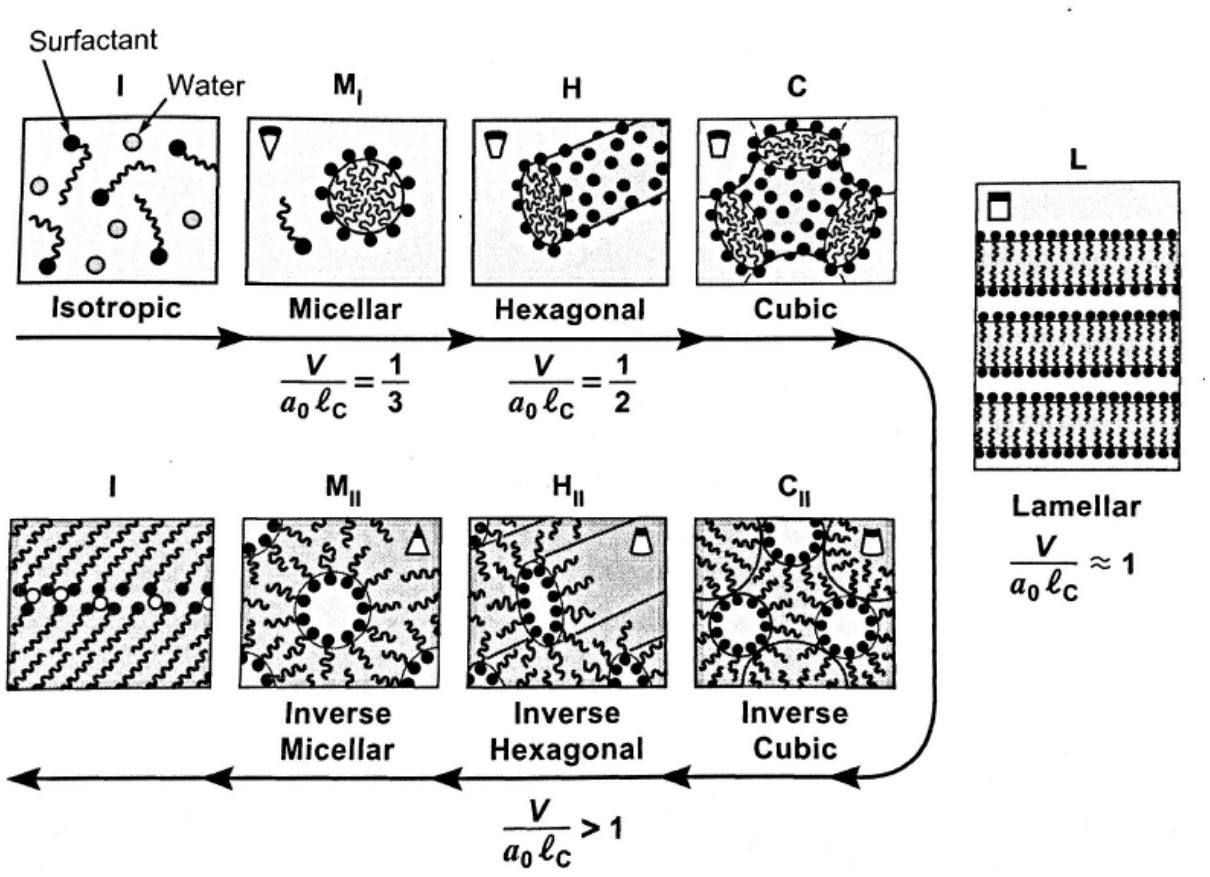

Figure 1.13: **Packing parameter for different mesophases.** Different types of mesophases dependent on the lipid's packing parameter. M for micellar, H for hexagonal (cylinders), C for cubic, L for lamellar, subscripts I for normal and II for inverted. Adapted figure with permission and content from Israelachvili [74].

Where can we use PAs?

Previously several applications in medicine, cosmetics, engineering, and drug delivery has been demonstrated using PAs. [76–79] (Fig. 1.15. Depending on the molecular design, the self-assembly can range from ribbons in twist, flat or helical form to nanofibers or tubes and spherical aggregates. These structures can further make gels or macromolecular networks that have a wide range of applications (Fig. 1.15) [77].

For example, it was shown that cylindrical nanostructures could target arterial injury and thus be used for vascular diseases [84] (Fig. 1.16). Interestingly targeted nanospheres were not efficient,

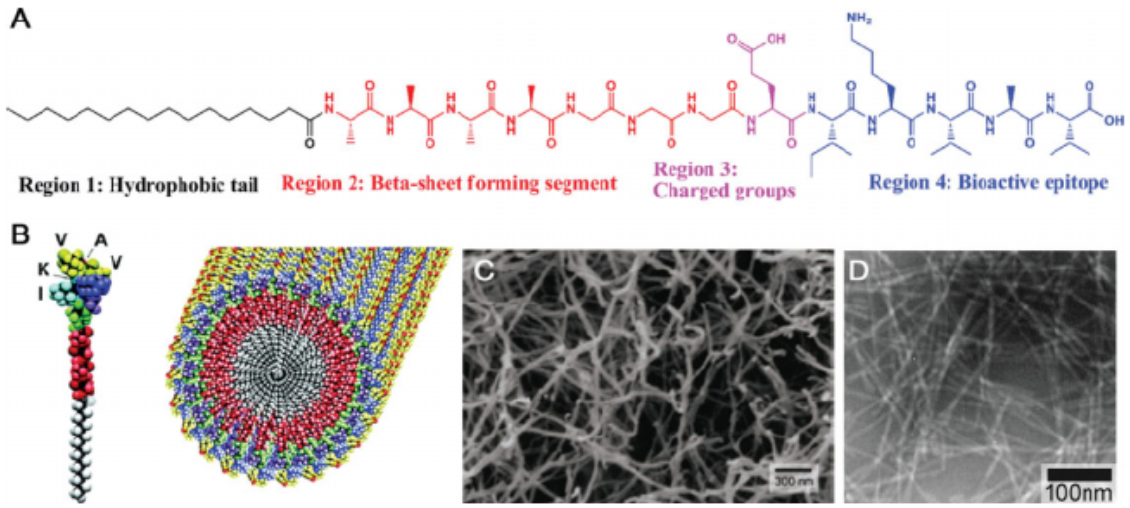

Figure 1.14: **PA with four rationally designed chemical parts.** a) PA design with 4 regions. b) Schematic representation for Nanofibers c) TEM pictures of fibers. Fig is adapted with permission from Ref. [80].

just like non-targeted PAs. Thus, sequence design is essential for signaling and functional self-assembly.

In addition PA nanofibers ~~was~~were demonstrated as potential biodegradable carriers for drug delivery [76]. The PAs contained lysine ε-amine-derivatized hydrazide systematically placed at four different positions along the peptide backbone (Fig. 1.17). Release of a fluorescent dye that formed hydrazones with the hydrazide was probed. It was found that the release rate is directly connected to the fluorophore mobility, which is influenced by the packing density, degree of order in the hydrophobic PA core, and the β-sheet character of the peptide [76].

As a another example, a mimic of the extracellular matrix (ECM) with PAs as an alternative to scaffolds made from collagen polymers was demonstrated. In nature, the ECM is a three-dimensional network consisting of extracellular macromolecules and minerals, such as collagen, enzymes, glycoproteins, and hydroxyapatite, that provide structural and biochemical support to surrounding cells. An essential property of the ECM is its ability for degradation by cell-mediated enzymes, which allows cells to create a pathway migration. A network with PA was made and incubated with a type IV collagenase enzyme. The Gels lost 50 % of their weight in the presence of the enzyme in one week and were degraded entirely in one month (Fig. 1.18). Thus it was demon-

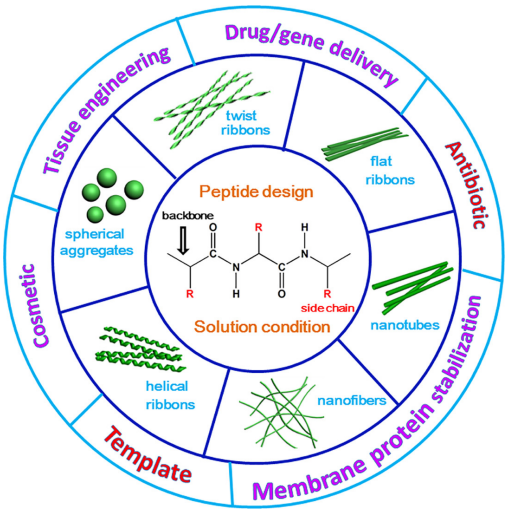

Figure 1.15: **Schematic representation of PA self-assembly.** Peptide design and solution condition determine self-assembly. The outer circle gives an overview where PAs have already been implemented. Fig. is adapted with permission from Ref. [83].

strated that PA networks could mimic this behavior and are an appropriate platform for dynamic studies of the ECM [85].

1.4 Intrinsically Disordered Peptide Amphiphilic

PAs are great candidates for nanocarriers and a promising platform for studying biological networks. Up to now, almost all hydrophilic headgroups in PAs are made by structure peptides inspired by nature [86–88].

Using IDPs instead of structural polypeptides adds a great functional advantage to structural plasticity discussed previously. The lipid-like intrinsically disordered peptide amphiphiles (IDPAs) can be engineered to a large scale of different mesophases. And additionally, IDPAs can interact much more flexibly with the environment than conventional PAs. Thus IDPAs are~~is~~ promising candidates for highly adaptive nanocarriers [89].

On the other hand, amphiphilic systems with IDPs as functional headgroups can be used to study IDPs themselves. As molecular spacing and surface interactions are very accurately accessible using scattering techniques, electrostatic interaction between neighboring IDPs can be exam-

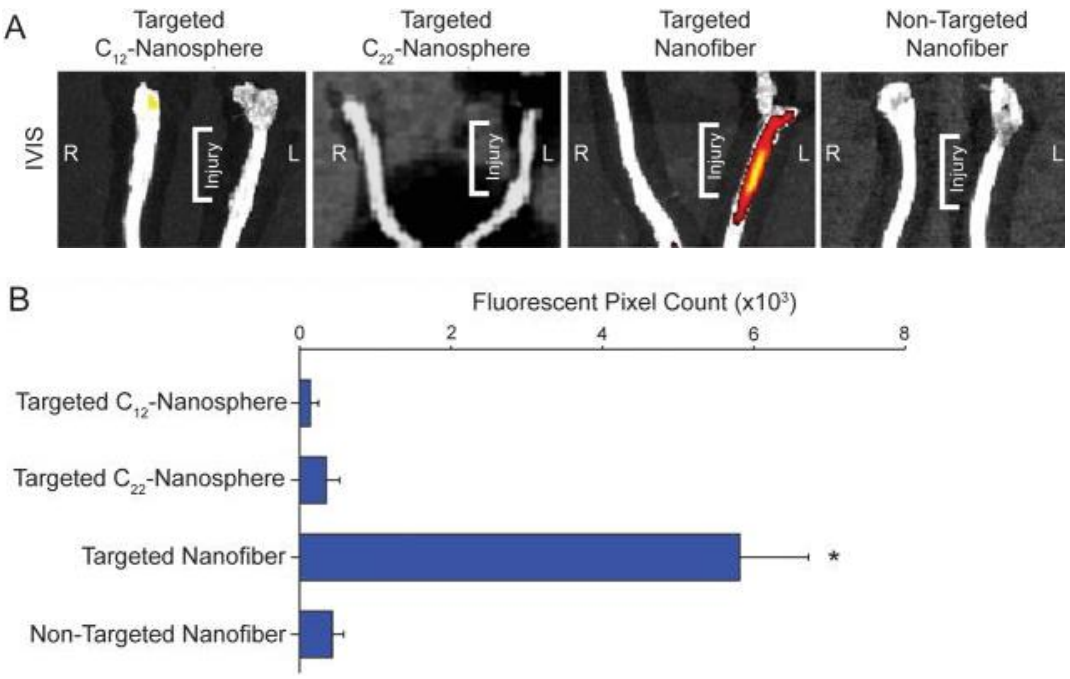

Figure 1.16: **Functionlized PAs for vascular disease treatment.** PAs were fluorescent labeled to track down their position in vivo a) Fluorescent image of injured and uninjured carotid arteries b) Positive fluorescent signal from the arterial cross-sections. Fig. is used with permission from Ref. [84].

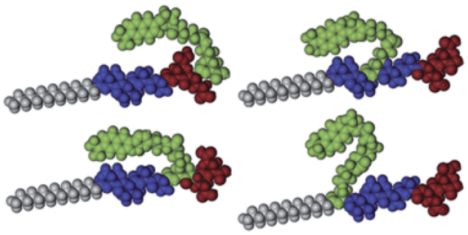

Figure 1.17: **PA design for functionalized nano fiber.** Lysine ε-amine-derivatized hydrazide (green molecule) is placed at 4 different positions in the peptide backbone, directly influencing drug release rate. Figure is adapted with permission from Ref. [76].

ined, and open questions from biology answered [89].

Where can we use IDPAs?

Since they hold a lipid anchor, IDPAs are easily incorporated into biological and pharmaceutical lipid membranes. In principle, this allows to graft properties of IDPs to lipid-based nanocarriers

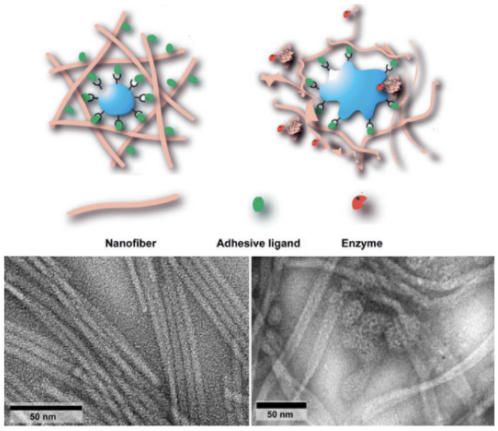

Figure 1.18: **Synthetic ECM.** top: Schematic represantion of ECM modell with cell before (left) and after (right) enzymatic reaction. bottom: TEM pictures of synthetic PA matrix before (left) and after 10 days of incubation with collagenase enzyme (right). Figure is adapted with permission from Ref. [85]

instead of using PEG lipids. For example, recombinant biopolymers made of proline/alanine-rich sequences (PAS) exhibit random coil behavior in aqueous solution and similar properties as the chemical polymer poly-ethylene glycol (PEG) [90].

IDPAs~~Intrinsically Disordered Peptide Amphiphiles~~ are ideal for tailoring properties of drug nanocarriers. In particular, IDPAs are readily combined with lipid-based delivery systems. However, the sequence design of IDPAs to tune the interaction of nanoparticles with each other and with living cells has been little explored in a systematic manner [89].

What do we know about IDPAs' self-assembly?

The self-assembly of IDPAs into mesophases facilitates the study of interactions by measuring structural parameters of salt, pH, and temperature. This is important as IDPAs have an excellent potential for surface modification of lipid-based nanoparticles in nanomedicine and pharmaceutical applications.

Very little has been published about IDPA self-assembly [89, 90]. But lipid derivatives with brush-like hydrophilic components, similar to IDPAs, such as PEG-lipids, were studied both experimentally and theoretically [91, 92]. Such studies elucidated the role of chain entropy and conformation of polymeric head groups in steric repulsion. The flexible brush-like conformation of

PEG-lipid headgroups is known to reduce protein adsorption and enhance the circulation time of lipid vesicles in the blood due [91, 92].

The situation, however, is more complicated in the case of IDPAs, which contain hydrophobic, hydrophilic, and charged amino acids. While their sequence may encode the inability to fold into a well-defined 3D structure and hence are predominately polymeric by nature, there are conformational subclasses that have only recently been described and started to be interrogated for functionality [30]. Most notably, in ampholytic sequences, oppositely charged residues will attract and form transient bridges.

1.5 Small Angle X-ray Scattering

In my research I wanted to study IDPAs' self-assembly in a systematic and precise manner. Their structures are in the range of some nanometers [89] and thus to small for optical microscopy.

Apart from the high resolution, the key advantage of Small Angle X-ray Scattering (SAXS) is its ability to resolve structures in solution under physiological conditions without the need for crystallization, or external tagging. SAXS does not need markers or other modifications of the sample itself or its environment, that might change the original structure. Thus, X-ray scattering doesn't need these disruptive factors and is an important tool in structural characterization of biological systems [93–96].

This makes SAXS a powerful technique for studying soft matter, and biological materials at the nanometer scale [97–102]. Both our labs in TAU and LMU are experienced in SAXS [23, 51, 98, 99, 103, 104] as a technique to study nanometer sized structures, especially in solution. SAXS is often used to determine the structural properties of amphiphilic systems [105–107]. Due to IDPAs' high monodispersity, SAXS is the ideal technique for determining properties at the Angstrom level.

In SAXS a sample gets illuminated by a monochromatic X-ray beam and scatters on a detector. The detector is a 2D camera that records the scattered X-ray intensity. The scattering pattern involves both the contribution from the structure itself and the surrounding solvent. Therefore, to

record the particles of interest, the scattered intensity of the background needs to be measured and subtracted from the original signal.

How are X-rays generated?

For the first time described 1895 by Wilhelm Conrad Röntgen, X-rays are indispensable in science. X-rays are photons, electromagentic waves, with wavelengths ranging ranging from 10 picometers to 10 nanometers, corresponding to energies in the range 145 eV to 124 keV where the energy (E) is given by:

$$E = \hbar v = \hbar c/\lambda, \tag{1.1}$$

where $\hbar$ is the dirac constant, v is the velocity of the particle, h is the planck constat, c is the velocity of light and λ is the wavelength of the particle.~~Here,.....add~~

One classical way to produce X-rays is to bombard high energy electrons on a metal anode. One ends up with two kinds of X-ray spectra:

- Continuous spectrum: deceleration of electrons causes bremsstrahlung due to energy conservation.
- Discrete spectrum: the accelerated electrons kick out an inner-shell electron. When an electron from an other shell goes back to the vacant shell, discrete radiation is emitted. Depending on the anode material, these discrete spectra differ. The so called K_α energy for copper is 8.0 keV, corresponding to a wavelength of 1.54 Å, and for molybdänum it is 17.4 keV, corresponding to a wavelength of 0.71 Å. To create a monochromatic beam the X-ray spectra is filtered and the monochromatic K_α beam is transmitted to the sample.

Another possibility to obtain X-rays are synchrotron radiation facilities. In synchrotons, bremsstrahlung is generated by charged particles (electrons or positrons), that are forced to ~~build~~ a circular orbit by magnets. Electrons are accelerated at a bending magnet, X-rays are emitted tangentially to the plane of the electron beam. The energy of the X-rays ranges from $4keV < E < 80keV$. Third generation synchrotons (e.g. the European Synchrotron Radiation Facility) operate so called undulators

or wigglers (alternating magnetic dipoles) that cause oscillations of the penetrating electron beam resulting in continuous bremsstrahlung [108].

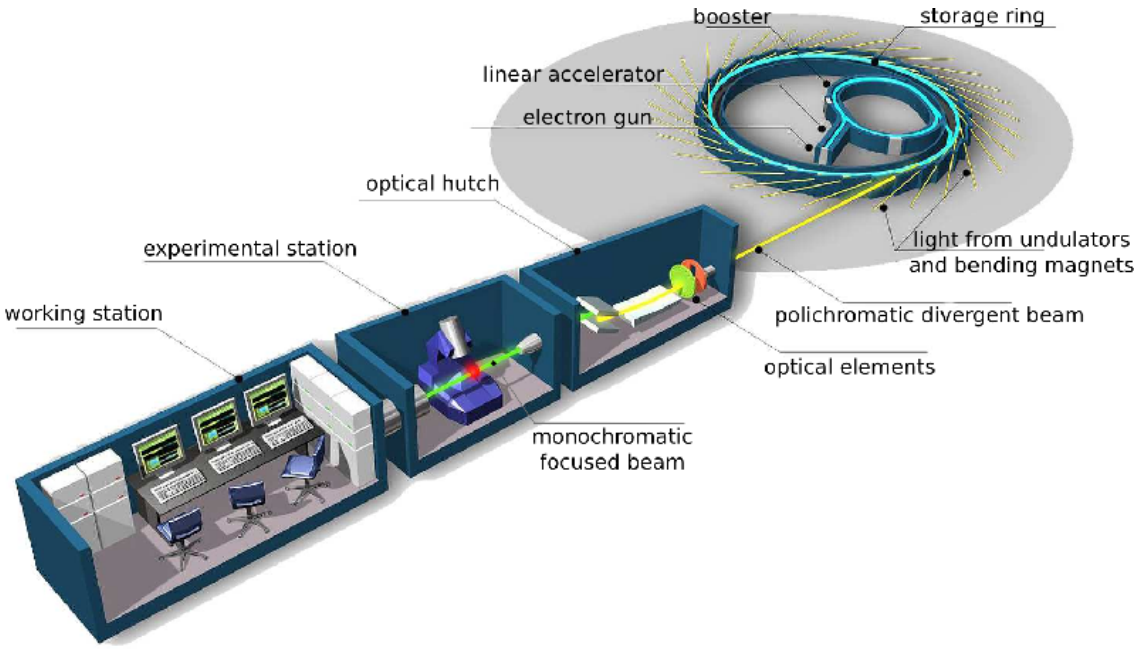

Figure 1.19: **SAXS at synchrotron beamlines.** Charged particles are accelerated in a storage ring an X-rays are generated. Polychromatic beam is filtered and can be used for SAXS experiments in the experimenting hutch. Figure is from synchrotron SOLEIL.

How does X-ray scattering work?

In SAXS systems, an intense monochromatic X-ray beam is produced and collimated to hit the investigated sample. Depending on the energy, some of the X-rays are absorbed in the sample and the rest are scattered depending on the local electron density distribution of the sample [108]. For my experiments, the scattered X-ray intensities are recorded on a 2D pixel detector (Fig. 1.20).

When X-rays are scattered on particles, they interfere with the incident beam and produce radial interference patterns depending on the observation angle 2θ, the orientation, and the inter-particle distances.

For nanoparticles randomly orientated in space, the intensity SAXS profile is independent of the vertical orientation to the incident beam. Thus, the scattering can be described by a 1D intensity profile via azimuthal integration. In such cases, the intensity is mostly presented as a function of

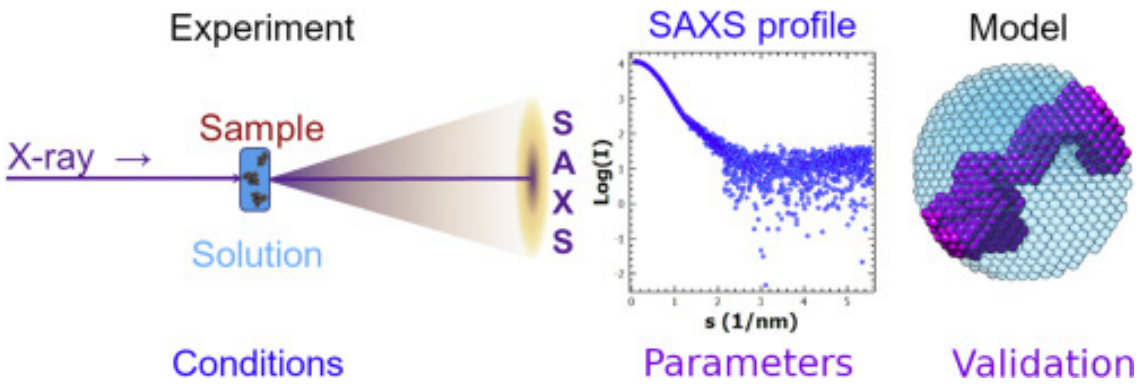

Figure 1.20: **SAXS principle.** X-rays are scattered on a sample in solution and scattering profile is recorded by a 2D detector. Intensity is radially integrated and ~~analyzed~~fitted to the right parameters to a model to get information about the sample's conformation in solution. Model can be validated and changed after fit to get a more realistic result. Figure is used with permission from Ref. [109] under license CC BY 4.0.

the scattering vector amplitude $|q|$:

$$|q| = \frac{4\pi}{\lambda} sin(\theta), \tag{1.2}$$

where λ is the wavelength of the incident beam. Samples dispersed in solution must be measured with a liquid sample holder. Thus, not just the scattering of the sample itself but also the background of the surrounding solution and chamber window are recorded. By subtracting the additionally measured background signal from the sample signal (taking into account the absorbance difference), the scattering of the particles can be isolated. The detector records the interference amplitude of all X-rays scattered by the electrons of the particles.

Where is the information of our sample?

The fundamental quantity is the Fourier transform $A(q)$ of the electron density (i.e., the number of electrons per unit volume, $\rho(r)$):

$$A(q) = \int \rho(r) e^{iqr} dV \left(\sum_{n=1}^{N} e^{iqR_i}\right), \tag{1.3}$$

where V is the volume of each particle, q is the scattering vector, r is the radius, R_i is the lattice distance vector, if the samples are arranged in a lattice, and N the number of particles. Following,

the scattered intensity is defined as the square of $A(q)$:

$$I(q) = A(q)^2 = |F(q)^2|S(q), \tag{1.4}$$

where $F(q)$ denotesis the form factor and $S(q)$ is the structure factor. Suppose experimenters can estimate the suitable form and structure factor insight about actual state electron density distribution, and thus geometrical arrangement can be extracted.

For dilute samples, we expect no inter-particle interaction or periodicity. This leads to $S(q) = 1$ and thus the intensity equals the form factor squared. For polydisperse systems, the form factors of all particle sizes need to be summed, which will limit our possibility of extracting useful structural information.

Form factor Analysis

Form factors of monodisperse isotropic spherical particles can be represented in spherical coordinates. A simple sphere [110] with a uniform electron density is described by:

$$F_{sphere}(q,r) = \frac{4}{3}\pi r^3 \Delta\rho(r) \frac{3((sin(qr) - qr\,cos(r))}{qr}, \tag{1.5}$$

where q is the scattering vector, r is the radius and $\Delta\rho$ the electron density difference between scatterer and solvent. For cylinders the form factor with radius R, length Ł and electron density contrast $\Delta\rho$ is:

$$F_{cyl}(q,\alpha) = 2\Delta\rho V \frac{sin(\frac{1}{2}qL\,cos(\alpha))}{\frac{1}{2}qL\,cos(\alpha)} \frac{J_1(qr\,sin(\alpha)}{qr\,sin(\alpha)}, \tag{1.6}$$

where J_1 is the first order Bessel function of the first kind [110], r is the radius and α is the angle between the principal axis and incident beam. However, for cylinders measured in solution with no preferred orientation, we need to average the form factor over all possible orientations:

$$< F_{cyl}(q)^2 > = \int_0^{\pi/2} F_{cyl}^2(q,\alpha) \sin\alpha d\alpha, \tag{1.7}$$

Natural systems often require more complex form factors that can be calculated using the above approach. For example, systems with an ellipsoidal structure can be fitted with an adapted spherical form factor or flexible~~;~~, worm-like structures can be fitted with a cylindrical form factor with an additional flexibility term.

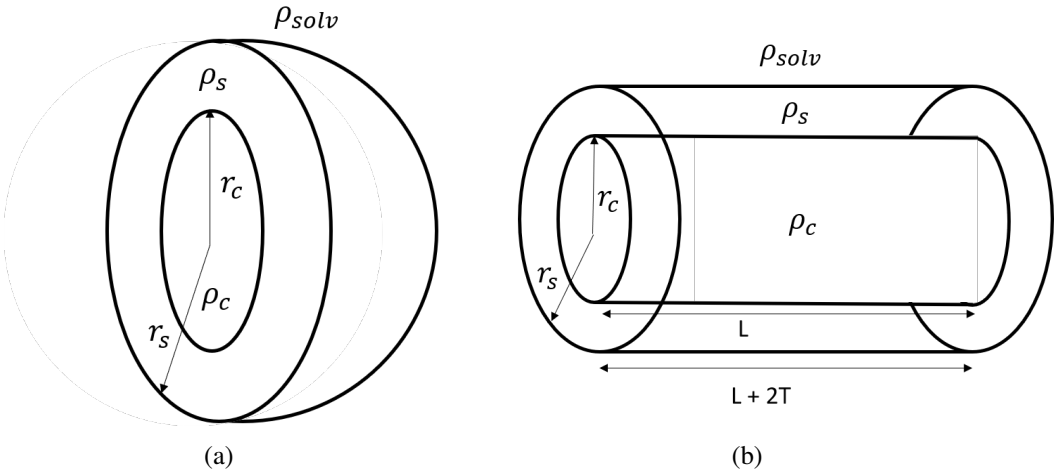

Figure 1.21: **Schematics for form factor.** (a) Core-shell sphere (b) Core-shell cylinder

Structure factor analysis

Aggregating samples or particles in high concentration can show interaction.~~The interaction is the the structure factor in the SAXS fit and can be described by:~~

The intensity will be the product of this structure factor $S(\vec{q})$ and the square of the form factor $F(\vec{q})$:

$$I(\vec{q}) = N|F(\vec{q})|^2 S(\vec{q}), \tag{1.8}$$

where N denotes the number of particles.

A beautiful example to show how form and structure factor are combined analysis is the self-assembly of Sodium Dodecyl Sulfate (SDS). SDS is an amphiphilic molecule that self-assemble into an ellipsoidal micelle with the following form-factor:

$$F(q,\alpha) = N(SLD_2 - SLD_1)V_1 f(q,R_1,R_1x_1,\alpha) + (SLD_2 - SLD_s)V_2 f(q,R_1+R_2,R_1x_1+R_2x_2,\alpha), \tag{1.9}$$

where

$$f(q,R_e,R_p,\alpha) = 3\frac{\sin(r(R_e,R_p,\alpha)) - \cos(r(R_e,R_p,\alpha))}{(qr(R_e,R_p,\alpha))^3} \tag{1.10}$$

and

$$r(R_e,\alpha) = [R_e^2\sin(\alpha)^2 + R_e^2\sin(\alpha)^2]^{\frac{1}{2}}. \tag{1.11}$$

SLD_1 and SLD_2 are the scattering length densities of the core and the the tails and R_1 and R_2 and V_1 and V_2 the corresponding radii and volumes. α is the angle between the axis of the ellipsoid, R_p is the polar radius along the rotational axis of the ellipsoid, R_e is the equatorial radius perpendicular to the rotational axis of the ellipsoid (Fig. 1.23).

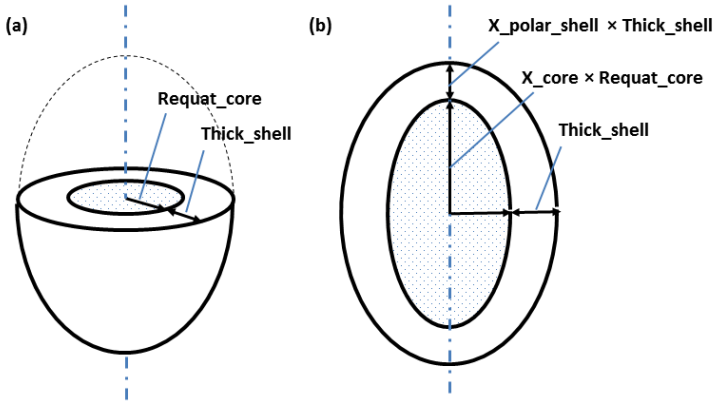

Figure 1.22: **llustration of fitting model for ellipsoidal SDS micelles.** The micelles contain a core and a shell with radii R1 and R2. Each radius can be scaled by x1 and x2, deforming the spherical shape into an ellipsoidal one. Fig. is adapted from website, http://www.sasview.org, visited last 6.6.2022.

As demonstrated in Fig. 1.23 for SDS, a structure factor model of charged particles can be used [111]. When multiplying the structure factor and the form factor ~~metioned~~mentioned above, the structure factor attenuates the high rise of the ~~structure factor~~data in the low q range so that the fit matches the data (Fig. 1.23).

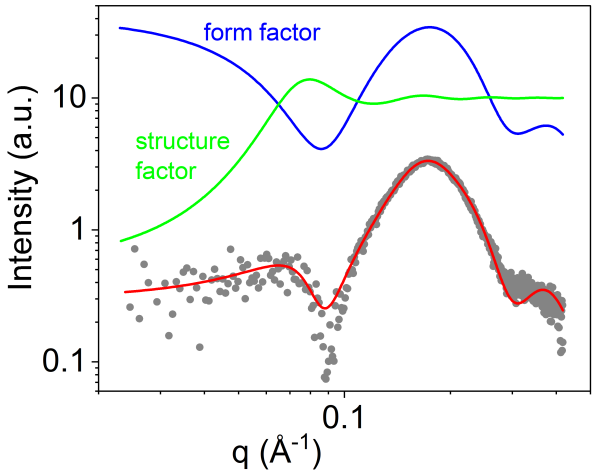

Figure 1.23: **Fit for SDS micelles.** Red curves represents product of ellipsoidal form (blue) and structure factor (green) for scattering data of $10mg/ml$ SDS in milliQ. Data set off for clarity. SASview was used for fitting. Data is taken in our in-house apparatus at LMU with an exposure time of 20min.

SAXS with crystals

One example for interparticle interference are crystal structures. If X-rays of wavelength λ are scattered on a crystal with a spacing of d between the lattice plane, constructive interference occurs under the following Bragg's law:

$$n\lambda = 2d\sin(\theta), \tag{1.12}$$

in which n is a positive integer and determines the order of diffraction. To understand the structural organization, I will recall the concept of the reciprocal lattice.

Ewald presented a way of showing lattice planes in a well-arranged form. It makes visualizing planes in real space easier by representing them in reciprocal space. In real space we have $\vec{a}_1, \vec{a}_2, \vec{a}_3$ as space lattice vectors and a set of atomic basic coordinates. Every atom in the crystal lattice can be reached by a linear combination of these vectors. The unit cell has the volume $V_z = (\vec{a}_1 \times \vec{a}_2) \cdot \vec{a}_3$. The reciprocal lattice has its reciprocal lattice vectors, $\vec{b}_1, \vec{b}_2, \vec{b}_3$. They fulfill this condition:

$$\vec{a}_i \vec{b}_j = 2\pi\delta_{ij}, \tag{1.13}$$

where δ_{ij} is the kronecker delta function. One can determine the reciprocal lattice vectors from real

space vectors by:

$$\vec{b_1} = \frac{2\pi}{V_Z}(\vec{a_2} \times \vec{a_3}), \quad \vec{b_2} = \frac{2\pi}{V_Z}(\vec{a_3} \times \vec{a_1}), \quad \vec{b_3} = \frac{2\pi}{V_Z}(\vec{a_1} \times \vec{a_2}). \tag{1.14}$$

The Miller indices, h,k,l are describing any coordinate in reciprocal space:

$$\vec{G} = h\vec{b_1} + k\vec{b_2} + l\vec{b_3}. \tag{1.15}$$

Lattice planes in reciprocal space can now be described with the miller indices (hkl), as well as directions of lattice vectors with $[hkl]$.

Diffraction condition in reciprocal space

We can use the reciprocal space in order to predict interference. A diffraction maximum occurs if the momentum transfer vector $\vec{q}$ is equal to a reciprocal vector of the crystal, $\vec{q} = \vec{G}$. Thus, if we know the real space vectors and use equ.s 1.14 and 1.15, we can calculate the scattering vector $\vec{q}$ and know where we expect diffraction peaks. Alternatively, if we know the scattering vectors $\vec{q}$, we can relate them to the lattice and observe the structure. We defined the exact peak positions by fitting them into a Lorentzian function.

Structure	Ratio q/q^*	Miller indices
Lamellar	$1:2:3:4$	(100) (200) (300) (400)
Hexagonal	$1:\sqrt{3}:\sqrt{4}:\sqrt{5}$	(10) (11) (20) (21)
Face Centered Cubic	$\sqrt{3}:\sqrt{4}:\sqrt{8}:\sqrt{11}$	(111) (200) (220) (311)
Body Centered Cubic	$\sqrt{2}:\sqrt{4}:\sqrt{6}:\sqrt{8}$	(110) (200) (211) (220)

Table 1.1: **Peak position relationships for crystalline phases.** Peak positions relative to the first one at q^* and miller indices for peaks. The ratios give the relative distances between $\vec{q}$-peaks in phase space if the particles are organized in the structure.

Kratky Analysis

Form- and structure factor gives information about overall self-assembly, while experimenters of IDP and IDPA are often interested in the flexibility of samples.

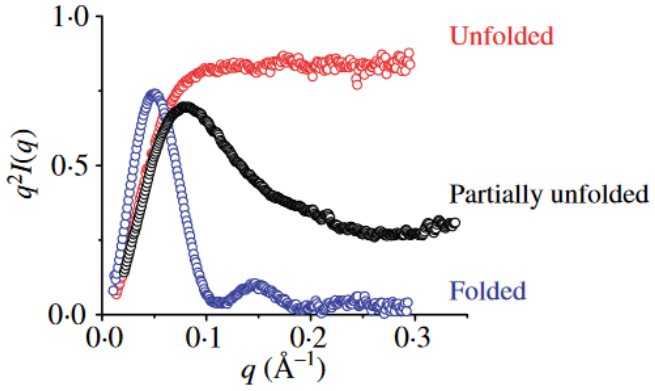

Figure 1.24: **Kratky plots.** $I(q)q^2$ is plotted against q. Plateau for high q point towards flexibles samples, while bell-shaped curves stand for rather unflexible ones. Figure adapted with permission from Ref. [113].

Using Kratky analysis, we can extract information about the degree of (un)folding of flexible, e.g., IDP, samples. In Kratky plots $I(q)q^2$ is plotted against q, when normalized, $q^2I(q)/I(0)$ against q.

The peak shape allows us to verify the conformation. Kratky plots that show a plateau for high q point towards flexible and/or disordered samples, while bell-shaped curves stand for rather unflexible and/or ordered ones (Fig. 1.24) [112].

Pair distance distribution function

For non-interacting particles, there is a relation between the Intensity $I(q)$ and the pair distribution $P(r)$:

$$I(q) = \int_0^{d_{max}} P(r)\frac{sin(qr)}{qr}dr, \tag{1.16}$$

where d_{max} is the maximal dimension of the scattered particle, regardless of the form and structure factor. Even though this is a direct way of calculating $P(r)$ it is not practical in reality, as $I(q)$ is resolution limited, not unique and just available for a confined q-range. An additional approach estimates $P(r)$ by iterativly ~~ind~~and the $P(r)$ that yields the optimal fit to the $I(q)$ profile [112].

The distribution function is described in real space and reaches zero for the maximum dimen-

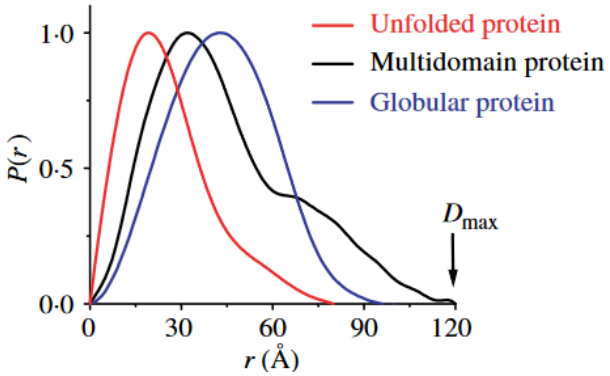

Figure 1.25: **PDDF plots.** Paired distances of scatteres determine maximal dimensions D_{max} of particles. Different geometries show various qualitative features. Figure adapted with permission from Ref. [113].

sion of the particle. In the case of a smooth sphere, this maximum dimension should be a relatively similar value to the radius of the particle (Fig. 1.25) [112].

Radius of gyration

Next to the pair distance distribution, one can use the radius of gyration, R_g, to determine particle dimension. In the R_g analysis, we are using just the very small q region for $q \to 0$:.

$$I_{q\to 0} = I_0 \exp(-\frac{1}{3} q^2 R_g^2), \tag{1.17}$$

where I_0 is the intensity at $q = 0$. When $\ln I$ is plotted against q^2 one gets a straight slope with slope $-R_g/3$. This accounts for $qR_g < 1.3$ [112].

How do we measure?

When measuring with SAXS, a big challenge is the design of a sample chamber that is on the one side suitable for the experiments' conditions, like temperature or sample volume, and on the other side provides reproducible measurements.

To this end, fluid samples are traditionally filled in X-ray capillaries made of quartz glass. Samples are sealed and placed under equilibrated conditions in a high-flux X-ray beam at the syn-

chrotron or in-house X-ray sources. Quartz capillaries suffer from curvature; therefore, precise positioning is crucial for replicable results. When repeated measurements at different time delays should be conducted, an open system is required,e.g., a time-resolved stop-flow and flow-through experiment in microfluidic channels [114–117].

Structural changes in scattering can also be measured by rinsing in a buffer within the microfluidic device and thus gradually changing the local concentration of, e.g., salt or *p*H [118, 119]. A disadvantage of flow systems is that they cannot handle liquid crystalline or viscous mesophases, like lipid membrane systems or aggregated samples. They are helpful, however, in studying the dynamics of aggregation, which are typically carried out in microfluidic devices with merging channels that allow continuous mixing [120]. In these devices a precisely positioned X-ray beam must capture the temporal-spatial relationship of chemical and physical reactions [121]. In our LMU in-house setup, we were using a sample chamber made out of plastic with a glued Kapton foil (Fig. 1.26).

Figure 1.26: **Sample chamber for our in-house source at LMU.** Sample is filled with a pipette throw a small hole in the top. Kapton is glued to the plastic chamber.

There are already various approaches for innovative X-ray chambers: There are microfluidic chambers made out of polymer materials, in particular, the amorphous and optically transparent cyclic olefin copolymer (COC) [121–125]. Here, an X-ray transparent chip allows for in-situ sample mixing during SAXS measurements.

1.6 3D Printing

Additive manufacturing or 3D printing opens an entirely new world for sample chamber fabrication. 3D printing is fast, cheap, and easily adaptable. The process in 3D printing is relatively straightforward: Model design with CAD software (e.g., Autodesk), rendering for 3D printing (e.g., with CURA), and print.

The very first person in additive manufacturing is Hideo Kodama. In 1980 he created his first 3D object: he used polymers that could be hardened or polymerized upon UV exposure. Just three year later, 1983, Chuck Hill presented the technology of Stereolithography: photopolymers are used that harden under light and are initially in liquid forms, such as epoxy resin. During printing, the top layer is cured, and the platform of the 3D printer then moves down by one layer thickness so that the entire model is again covered with a layer of the photopolymer. This is now cured again with the laser at the points required for the model and so on and so. However, since these areas are not freely exposed in the plastic bath, the printing of support structures is necessary for this printing process. The printing process is relatively accurate, but the photopolymers react to UV radiation and are not remarkably durable. These days, this technique evolved with new resin materials that are more UV stable (Fig. 1.27) [126].

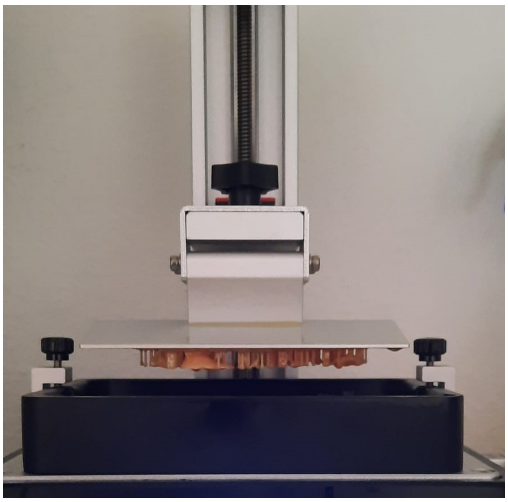

Figure 1.27: **Resin printer** Model is printed sheet for sheet via laser curing of photopolymer.

In fused deposition modeling (FDM) a plastic filament is heated briefly above its melting point.

It is then applied layer by layer with a heated nozzle to the already printed model. The plastic then hardens as it cools. acrylonitrile butadiene styrene and polylactide is the most common plastics. However, more exotic materials can also be used, such as COC, (see Fig. 1.28 for our in-house COC printer), and even filaments with metal exist.

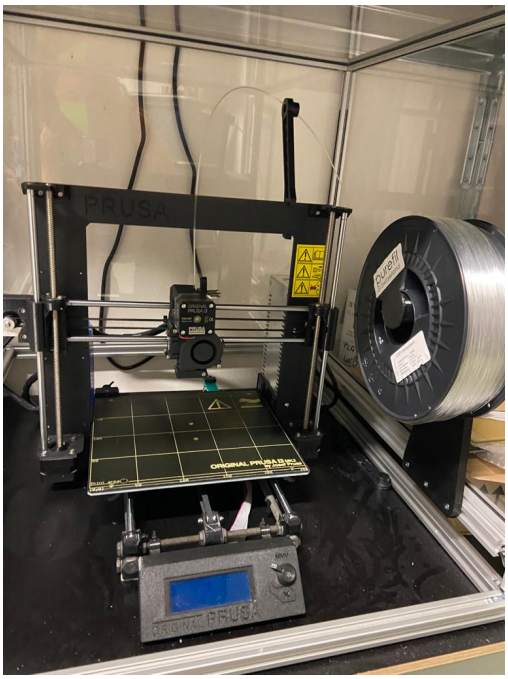

Figure 1.28: **COC 3D printer from our lab at LMU.**

With FDM, overhang parts must also be printed with support structures. In the printed parts, the individual layers stand out much more than in printed parts with SLA, which means that the quality of the surface is comparatively lower. The biggest challenge in 3D printing with FDM is designing the model so that support structures are not disturbing the final result in adapting the printing temperature and speed to the filament material.

Chapter 2

Material and Methods

This chapter gives an overview of the experimental and computational methods used in this work.

2.1 IPDA preparation

All peptides were purchased and synthesized via solid-phase synthesis by LifeTein. Amino acids are assembled from the C-terminal to the N-terminal while the peptide remains anchored to insoluble solid resin support. The process involves repeated coupling cycles, deprotection, and washing (Fig. 2.1).

The hydrophobic domain has either single or double hydrocarbon chains. After adding the last amino acid and deprotection, the fatty acid chain was conjugated to the deprotected amine. Double chain PDAs were prepared by conjugation of Fmoc-Lys(Fmoc)-OH, followed by cleavage of the two Fmoc protecting groups and conjugation of the two tails.

The IDPA or peptide powder was first fluidized in purified water (milli-Q) at twice the desired concentration. The solution was then titrated with NaOH to a *p*H where the solution became more homogeneous (preferably a *p*H where the IDPAs are soluble in water). Titration was monitored using a small *p*H probe. Following titration, 50 μl of the solution was combined with 50 μl of 2X buffer of choice, to achieve a *p*H in the vicinity to the desired one. The 2X buffers Acetic Acid (*p*H 3-4.5), MES *p*H (5-6.5) and MOPS (*p*H 7-7.5), were prepared at 200 mM, so as to achieve a final

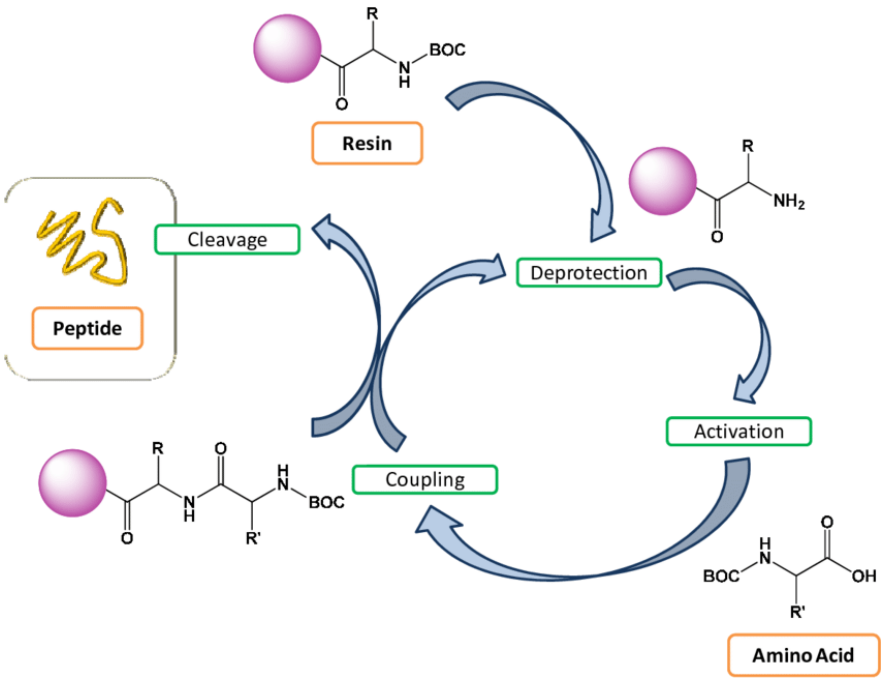

Figure 2.1: **Schematic representation of solid-phase peptide synthesis.** Amino acids are synthesized from the C-terminal to the N-terminal. Fig. is adapted unter license CC BY 3.0 from Ref. [127].

buffer molarity of 100 mM after mixing with IDPA or peptide solution 1:1 (vol:vol).

2.2 Small Angle X-ray Scattering

2D images from our in-house SAXS systems were integrated using the in-house developed software SAXSi [58]. Here, sample to detector distance is calibrated with the well know material AgBh. After integration all samples are scaled by transmission and the appropriate background (buffer without sample) was subtracted.

SAXS data was then fitted with the Software X+ developed by the Raviv lab [128]. This software allows to analyse integrated curves of biological material in a geometrical conformation with various layer of different electron densities. The thickness and electron density of each layer are the fitting parameters for the form factor. Also, polydispersity, as Gaussian curves, of one size parameter at a time can be taken into account. The basic algorithm for fitting is Levenberg–Marquardt algorithm [129] in a further developed form and combined with the Moore–Penrose pseudo-inverse

[130] and singular value decomposition [131] to improve fitting stability and the rainfall algorithm, a nature-inspired optimization algorithm. To optimize a function, a rainfall algorithm mimics the movement of water drops generated during rainfall. In SAXS, fitting with the rainfall algorithm is implemented to overcome convergence on local minima [128].

2.3 IDP charge caluclation

Very important for our research was the calculation of *p*H dependent charge distribution of IDPs. For a first approximation we summed for each *p*H value, over the charges of all amino acid:

$$c_{pH} = \sum_{i=1}^{n} c_{pH}^{i}, \tag{2.1}$$

where c_{pH}^{i} is the charge of each amino acid at the calculated *p*H. Local effects can change this naive picture. For example, hydrolyzed samples can cause local pH changes resulting in changed enzymatic behavior of the protein [132].

2.4 IDP disorder analysis

Due to IDPs' structural flexibility, various techniques and analyses are targeting representative parameters of the protein's conformational ensemble [133]. In the following, I will introduce several experimental and computational techniques targeting the nanoscopic dimensions of IDPs.

2.5 FRET

Förster resonance energy transfer (FRET) can be used to determine distance-dependent dipole-dipole interactions between probes. In FRET, a donor chromophore is excited and then does not excite a photon during relaxation but transfers its energy via dipole-dipole coupling to an acceptor chromophore, which then relaxes and excites a photon (Fig. 3.13).

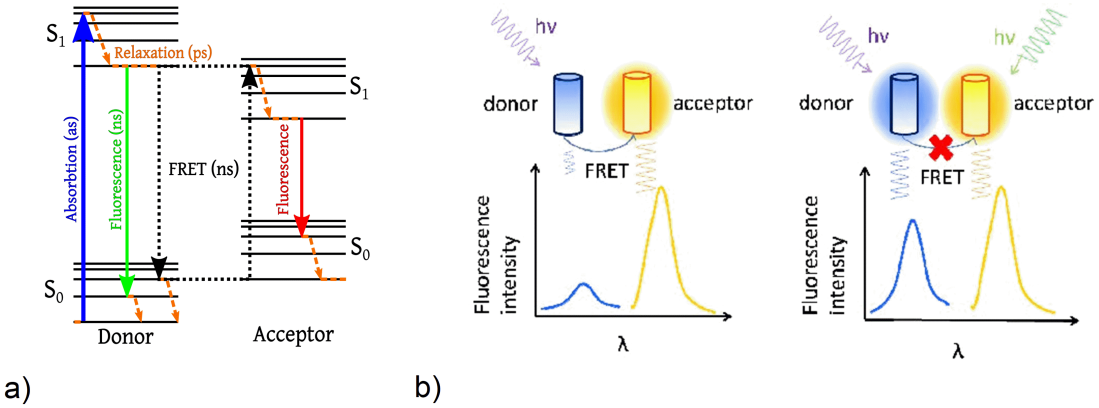

Figure 2.2: **Principle of FRET.** a) Jablonski diagram showing energy transfer from acceptor to donor molecule b) Dependency on molecular distances: close molecules show high energy transfer (left), while molecules, that are further apart show low energy transfer. Fig. is adapted with permission from Ref. [134] under license CC BY.

This process is susceptible to small changes in the distance (typically in the range of $1-10$ nm) as the energy transfer E is inversely proportional to the sixth power of the distance r [135, 136]:

$$E = \frac{1}{1 + r/R_0^6}, \tag{2.2}$$

where R_0 is the so-called Förster distance of this pair of donor and acceptor - the distance where the energy transfer efficiency is 50%.

In our experiments, we used FRET to determine if IDPs' conformations change when they get conjugated to hydrocarbon chains. We used a Cary Eclipse fluorescence spectrophotometer (Agilent Technologies, Santa Clara, CA). Measurements were done in a 1 cm quartz cuvette at 10 μM concentrations in 100 mM buffer at 25C°. Excitation spectra of IDP and IDPA included donor and acceptor (DA) spectra and acceptor only (AO) spectra. The samples were excited over the range of 250–330 nm (bandwidth 2.5 nm), and the emission was set to 350 nm (bandwidth 20.0 nm). The excitation spectra were normalized at 290-295 nm (no Tyr absorption). The level of energy transfer, E, between the donor and the acceptor, Y and W, respectively, was determined by the difference in integrated intensity at 270-285 nm and using YW dipeptide as a reference for 100% energy transfer. Buffer and background signals were routinely measured and subtracted.

Distance, r, was calculate using $E = R_0/(R_0 + r)$ while the Förster radius, R_0, was set as 15 Å.

2.5.1 Circular dichroism measurements

Circular dichroism (CD) were used for IDP disorder analysis. The measurements were performed using a commercially available spectrometer (Applied Photophysics Chirascan). The samples are added to a glass cuvette with a $1mm$ path length. Phosphate buffer was used to achieve a concentration of $0.1\frac{mg}{ml}$. The measurements were performed with phosphate buffer because the buffers used for the X-ray scattering experiments (mainly MOPS and MES) have high absorption at the relevant CD wavelengths. The wavelength range of $190-260nm$ was measured in $1-nm$ steps with 0.5 seconds per point. Three measurements were performed for each probe, and the mean value was calculated.

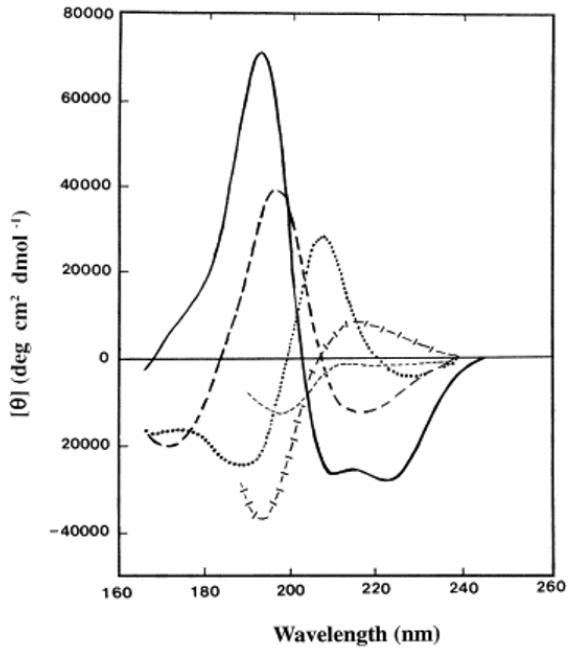

Figure 2.3: **CD spectra associated with protein structures.** Solid line corresponds to α-helix, long dashed line to antiparallel β-sheet, dotted line β-turn, crossed dashed line to extended 3_1-helix or poly II helix and short, dashed line to irregular structure, like IDPs. Figure is used with permission from Ref. [137]

2.5.2 Computational methods

The disorder can also be analyzed computationally. Different software use an energy estimation to determine if specific regions can bind and thus are prone to be disordered. The basic principle lies in calculating intramolecular statistical potentials between amino acids within the protein.

IUPred2

IUPred2 [42, 138] uses an energy estimation method. The principal lies in the 20×20 energy predictor matrix P_{ij} that shows the statistical potential for the 20 amino acid to connect with each other in a globular protein. :

$$e_i^k = \sum_{j=1}^{20} P_{ij} c_j^k, \tag{2.3}$$

where e_i^k is the energy of the residue in position k of type i. The equation calculates for each position k the sum of for all elements j in the amino acid composition vector c_j for all types i. Its parameters were optimized to minimize the difference between energies estimated from the amino acid composition vector and the energies calculated from the known structure for each residue in the dataset of proteins. With the energy estimation, we can now calculate an approximation of the pairwise energy for each residue without relying on the structure and separate between ordered and disordered sequences: The energies are averaged over a window of 21 residues and transformed into a score between 0 and 1, where 0.5 marks the threshold for disordered sequences (false positive rate 5%).

ANCHOR2

As IUPred2, ANCHOR2 [42, 139] also uses an energy estimation method and adds two more terms to the energy estimation: the interaction of the residues with the globular protein and the local environment. Thus, ANCHOR2 combines the disordering tendency calculated by Iurpred with the sensitivity to the environment of the protein and can predict if a specific region is disordered in isolation but can undergo disorder-to-order transition upon binding- without even knowing the

possible binding partners. ANCHOR2 calculates a score S_k:

$$S_k = (E_{gain} - E_{gain,0})(I_k - I_0), \tag{2.4}$$

where the averaged IUPred2 score I_k is multiplied with the energy residue gain, $E_{gain} - E_{gain,})$, made through interactions with an averaged ordered surface. Here, $E_{gain,0}$ and I_0 determine the minimum energy gain and minimum average disorder tendency a residue has to have to be a disordered binding site.

CIDER

CIDER stands for Classification of Intrinsically Disordered Ensemble Regions and was developed by the Pappu lab [140]. It is a tool to check critical parameters of disordered sequences quickly - it is mostly interesting for polyampholytic IDPs.

They introduced the so called patterning parameter κ to characterizes sequences based on the linear distribution of oppositely charged residues. To calculate κ the sequence must be divided into N_{blob} blobs, whereas a blob refers to the number of residues beyond which the balance of chain–chain, chain–solvent, and solvent– solvent energies is of order kT (k is Boltzmann's constant and T the temperature). First we need to calculate the charge asymmetry for the entire sequence,

$$\sigma_i = \frac{(f_+ - f_-)_i^2}{(f_+ + f_-)_i}, \tag{2.5}$$

and for each blob i in the sequence of interest by

$$\sigma_i = \frac{(f_+ - f_-)_i^2}{(f_+ + f_-)_i}, \tag{2.6}$$

where f_+/f_- is the number of positively/negatively charged amino acids. Now the squared devia-

tion of each σ_i from σ is calculated by

$$\delta = \frac{\sum_{i_i}^{N_{blob}} (\sigma_i - \sigma)^2}{N_{blob}} \tag{2.7}$$

.

For different variants of the sequence δ will differ. With the maximum value δ, we can than define

$$\kappa = \frac{\delta}{\delta_{max}}. \tag{2.8}$$

κ is calculated for blob sizes of 5 and 6; the average is calculated. Low values of κ point toward well-mixed sequence variants, and $lim_{\kappa \to 1}$ indicates that oppositely charged residues are segregated in the linear sequence.

2.6 Cryo-TEM

Dry state transmission electron microscopy (TEM) provides insight into the size and shape of individual particles. The basic principle of TEM is the same as for optical microscopes: a light/electron beam gets shined on the sample, and the sample structure and morphology are determined by the specific absorption and transmission of particular waves. The significant difference is that light microscopes use light rays to focus and produce an image, while the TEM uses a beam of electrons to focus on the specimen to create an image.

In traditional TEM, the samples need to be dried for measurements. But this dried-out technique is prone to artifacts [141].

A more complete and accurate view of the system can be achieved with cryogenic (cryo) TEM. In cryo-TEM, an aqueous sample is vitrified in solution, thereby avoiding artifacts introduced by drying. Unfortunately, cryo-TEM again fails to provide any information about dynamics; rather, it necessarily images the specimen in a vitrified, frozen state. At best, static intermediates of an evolving system can be viewed. However, direct insight into nanoscopic dynamics can be gained

from liquid cell TEM (LCTEM) [141]. We have partnered up with the Gianneschi lab from North Western University. The group is specialized in LCTEM, an in-situ imaging technique that enables direct visualization of hydrated nano-materials and their dynamics through real-time videography.

For our experiments,~~cryogenic TEM~~ cryo-TEM specimens were prepared using an FEI Vitrobot by blotting in 95% humidity and subsequently plunging lacey carbon grids into liquid ethane. Images were taken for cryo-TEM using a JEOL 1230 transmission electron microscope operating at 120 keV equipped with a Gatan camera.

SAXS measurements

SAXS data can be either taken in-house or at synchrotron beamlines. There are a few things that synchrotron beamlines generally do better than in-house sources, but the most important are higher flux and better collimation. This results in shorter exposure time and better resolution.

Synchrotron beamlines

We did our experiments at Diamond Light Source (Didcot, UK), DESY (Hamburg, Germany), and SOLEIL (Paris, France). For liquid samples, these synchrotrons have robotic sample exchargers that automatically load the temperature controlled fluid sample from a PCR tube to a flow cell made out of a quartz capillary (Fig. 2.4). The flow cell is stable, thus fluctuations in background subtraction are minimized.

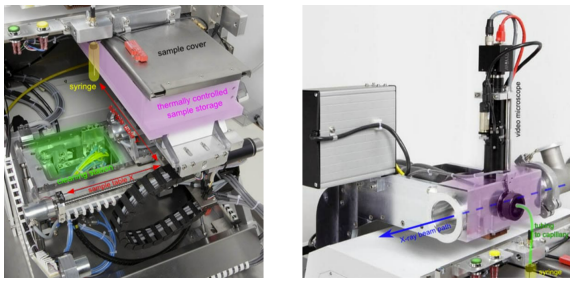

Figure 2.4: **Arinax sample robot.** The sample robot allows sample storage at controlled temperature and automatic loading. Flow cell stays stable, thus background subtraction is optimized. Figure is from webpage https://www.arinax.com/biosaxs-automatic-sample-changer-robot/ accessed last on the 27th of Jun3 2022.

In-house apparatus

A significant drawback of synchrotrons is the long time between experiments and beamtime application. One usually needs to apply for a beam time and then gets a slot at least half a year in advance for beam time of around one to five days. This makes automatic measurements or time-resolved measurements over days unrealistic. For that, an in-house apparatus is a good alternative.

Our in-house SAXS system at LMU consists of a Mo GeniX3D microfocus X-ray tube (Xenocs SA, Sassenage, France) combined with FOX2D single reflection optics delivering a monochromatic and highly stable beam with an X-ray energy of $17.4keV$. At the sample stage, the flux is typically around 2.5×10^6 photons/s. For collimation the beam enters an $82cm$ long, fully evacuated collimation path closed by a 25 μm thick Kapton foil at the end. Collimation is achieved by integrating two partially motorized scatter fewer aperture slits (Xenocs SA, Sassenage, France), one upstream right at the mirror and the second at the tube exit. The sample stage is positioned 5 cm before the collimation path exits (detailed picture of in-house apparatus in fig. 2.5).

At Tel Aviv, measurements were performed with a Genix3D (Xenocs) low divergence Cu Kα radiation source (wavelength of λ = 1.54) and scatter-less slits setup. Two-dimensional scattering data with a wave vector amplitude, q, range of 0.1-3.3 $^{-1}$ and at a sample-to-detector distance of about 1000mm were collected with a Pilatus 300k detector. The exact sample to detector position was calibrated using Silver behenate powder. For both in-house systems, the 2D diffraction data were radially integrated using data reduction software (SAXSi) developed in Beck's lab [58].

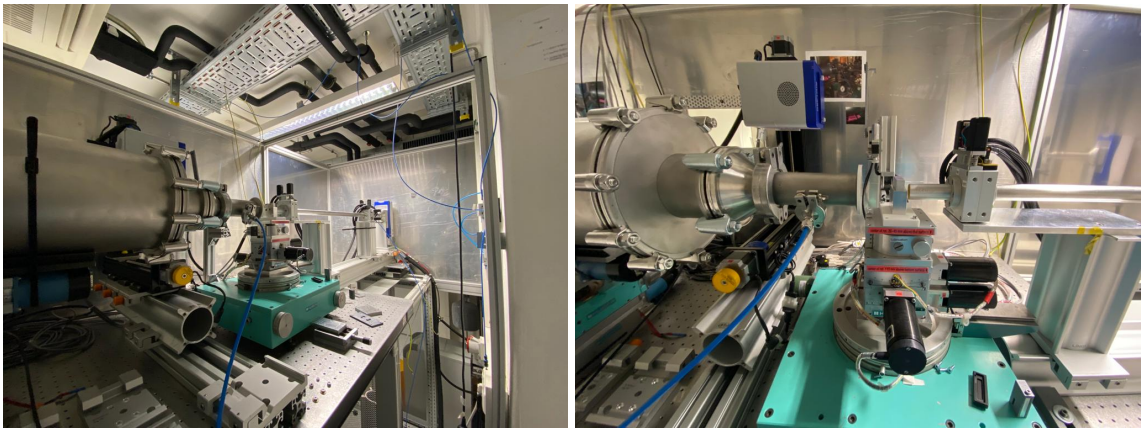

Figure 2.5: **Photos of our in-house apparatus at LMU.**

Chapter 3

Results

The main research focus was ~~on investigating~~to investigate the pH-dependent self-assembly of intrinsically disordered peptide amphiphiles using small-angle X-ray scattering to provide a molecular platform for the design of transformative nanocarriers [89]. The idea is to assemble a system where we can analyze self-assembly down to a single amino acid. We did not just want to show a static method but developed a dialysis chamber that allowed in-situ buffers.

3.1 Order from the disorder with intrinsically disordered peptide amphiphiles

Before my project, I contributed to various studies with amphiphiles. Parts of the intrinsically disordered carboxy tail-domain of neurofilament-low (NF-L) protein, found in the cytoskeleton of nerve cells [99, 101, 142, 143] is the critical building block of all of our IDPAs. In our first IDPA project[1], we used this IDP sequence to create an IDPA where an aromatic branching unit caps the N-terminus of the IDP sequence and allows the branching into two different types of architectures containing either two or four hydrocarbon tails (2×12, 4×7). Using turbidity, cryo-TEM (Fig. 3.1) and Small-angle X-ray Scattering (SAXS) we showed that these IDPAs form very monodisperse

[1] The content of this chapter is based on our recently published article in Ref. [89]

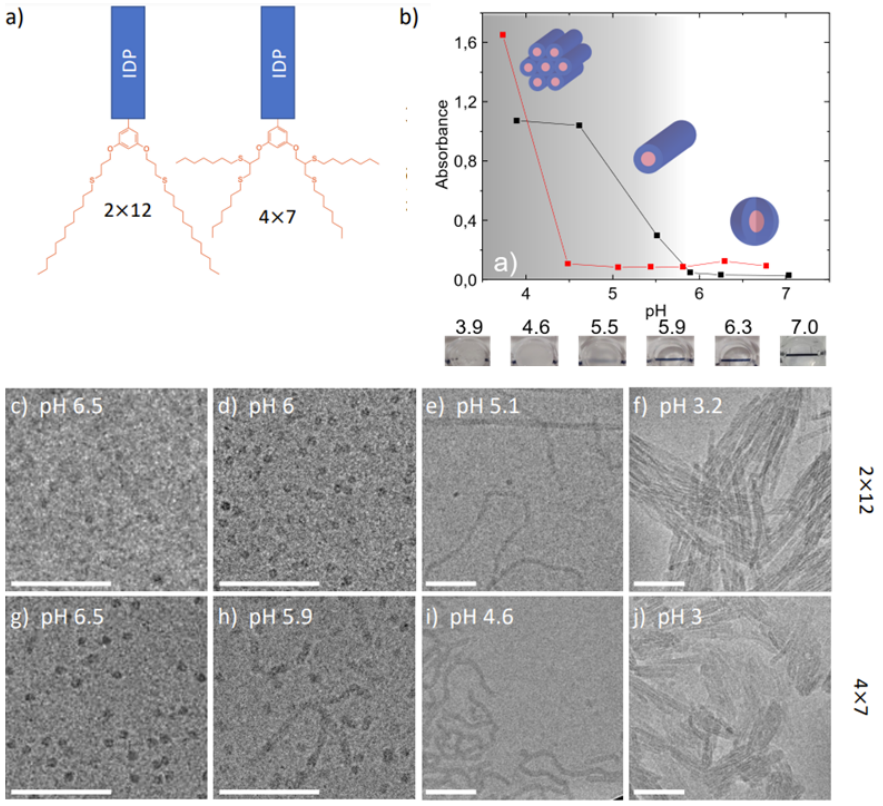

Figure 3.1: **Self-assembly of IDPA in mesophases.** (a) Schematics of the IDPAs with two tail variants (2×12 and 4×7) and the one-letter IDP's sequences used in this study. (b) Turbidity measurement of 4×7 (black) and 2×12 (red). Results show an increase in turbidity when lowering the pH, indicating a transition into large assemblies. (c-j) *IDPA1* Cryo-TEM images showing of self-assembly of (c-f) 2×12 and (g-j) 4×7 at various marked pHs. Cryo-TEM images show (c,d,g) spherical micelles at low pH, (e,h,i) coexistence with worm-like micelles at intermediate pH, and (f,j) aggregated micellar rods at low *p*H. All images were taken at 10 mg/ml IDPAs' concentration. Scale bar is 100 nm. Figure is adapted from [89].

particles and undergo a pH-dependent sharp phase transition from micellar low-dispersity spheres to extremely elongated wormlike micelles.

Cryo-TEM measurments of the 2×12 showed spherical micelles at *p*H 6.5 and 6 and worm-like micelles for *p*H 5.1 that aggregated at *p*H 3.2. The 4×7 variant also formed spherical micelles for high *p*H (6.5), a coexistence region with worm-like and spherical micelles at intermediate pH (5.9), and (aggregated) micellar rods at low *p*H (*p*H 4.6 and 3) (Fig. 3.1). Turbidity measurements supported the Cryo-TEM image results. The absorbance increased when lowering *p*H indicating a transition into large assemblies (Fig.3.1).

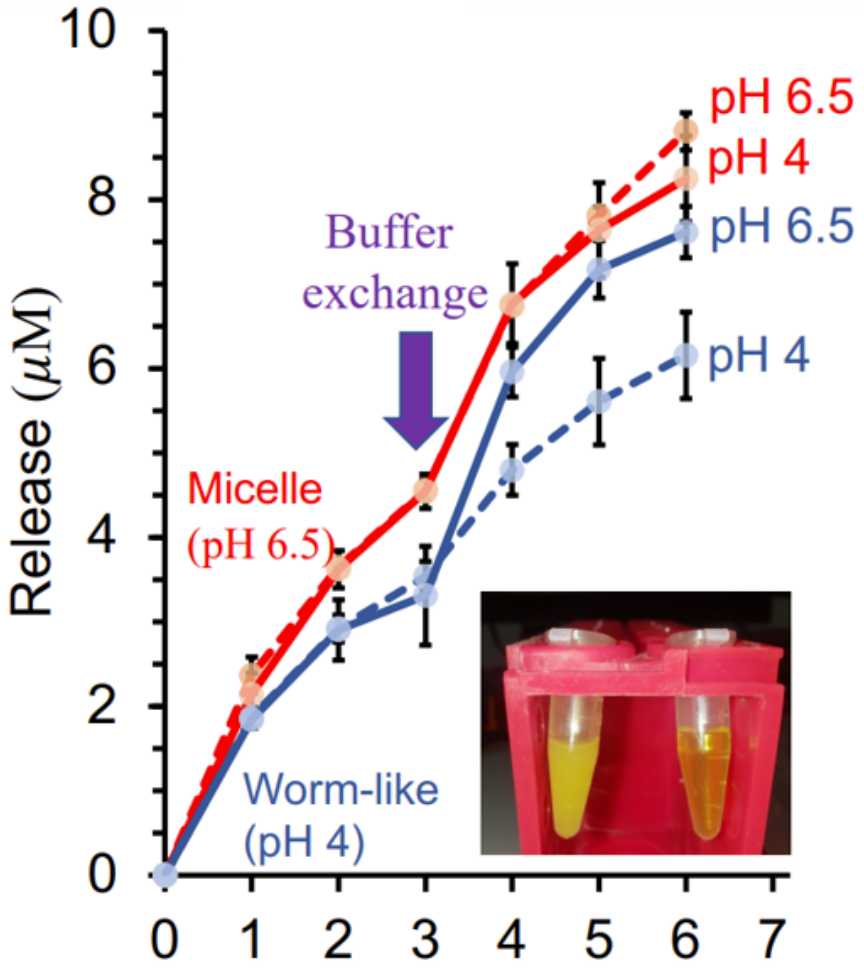

Figure 3.2: **Dye release experiment.** Accumulative released dye concentration for IDPAs, blue and red data-points represent a baseline *p*H for the experiments of 6.5 and 4, respectively. After 3 h, the buffer was exchanged either to induce structural mesophase transition via pH trigger (solid lines), or to identical and fresh buffer (dashed line).Figure is adapted from [89].

Additionally, we verified their potential to be used as a mechanism to design hold-and-release charges. To verify that we did an encapsulation experiment using a hydrophobic dye encapsulated in the IDPA micelles. Upon *p*H change from *p*H 4 to 6.5 the IDPAs transitioned from micelles to worm-like micelle and vice versa resulting in a dye release. The increased free dye concentration changed the optical absorbance of the solution (Fig 3.2.

3.2 Self-Assembly of Tunable Intrinsically Disordered Peptide Amphihphiles

In our next project we designed various IDPAs with different chain lengths that are entirely synthesized on a commercially available system.[2] A peptide sequence inspired by the disordered regions of neurofilament low protein was systematically altered to study how the interplay of hydrophobic tail(s) architecture and polypeptide headgroup conformation dictates the self-assembly process.

3.3 IDPA design

In total, we designed and commercially synthesized five different sequences, termed IDPA1, 2, 3, 4 and 4Δ conjugated to various hydrocarbon chains. We used common linear fatty acid chain lengths: 12 (Lauric acid), 14 (Myristic acid), 16 (Palmitic acid), and 18 (Stearic acid) carbons (see table 3.1). The IDPAs are synthesized using an automated solid-phase synthesizer. The peptide sequences are 18 amino acids long, containing protonable residues and hydrophilic amino acids (Fig. 3.3.)

Like in our previous work [89] IDPA1's 2×12's primary sequence (Fig. 3.5) is inspired by the intrinsically disordered carboxy tail-domain of neurofilament-low (NF-L) protein, found in the cytoskeleton of nerve cells [99, 101, 142, 143]. IDPA1 was synthesized with one or two aliphatic tails with three different tail lengths (2×12, 2×14, 2×16 and 1×14,1×16, and 1×18) to investigate the influence of the hydrocarbon tail domain (table 3.1). In IDPA2 2×12, we used the same amino acids as in IDPA1 2×12 but placed all negative (positive) charged ones bunched at the amine (carboxyl) terminus. Both IDPAs have 11 chargeable residues ($NCPR \approx 6$ at physiological pH). Thus electrostatic interaction are prone to play an important role. The isoelectric point for both IDPAs is calculated at *p*H 3.8. At approximately *p*H 5.5 aspartic and glutamic acid get protonated, resulting in a drastic decrease in net charge and the total number of charged residues (Fig. 3.5).

We wanted to understand how one amino acid mutation can influence this intermediate *p*H

[2] The content of this chapter is based on our submitted article in Ref. [144]

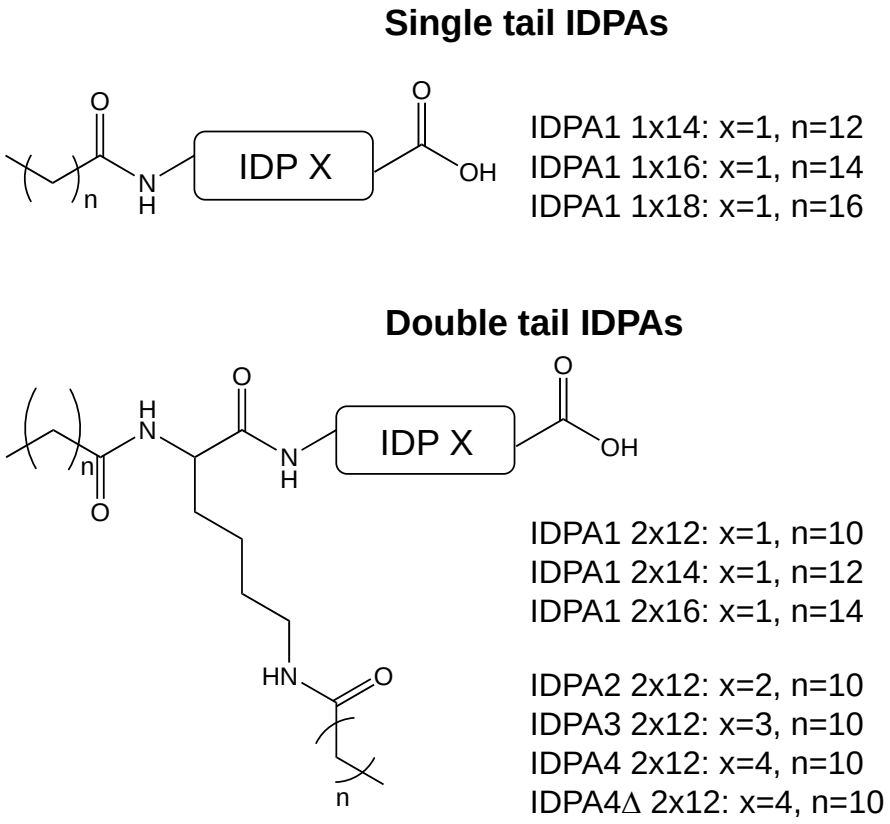

Figure 3.3: **Chemical structures for double and single tailed IDPAs.** IDP X stands for different sequences that were attached to various single and double tailed hydrocarbon tails.

region. Therefore, in IDPA3 2×12 we replaced the positively charged histidine at position 10 of IDPA1 2×12 with neutrally charged glycine (Fig. 3.5).

Our last IDP sequence was meant to show the potential of our IDPA system as agent reactive biomolecules. IDPA4 2×12 has a cleavage site that the MMP-9 matrixin enzyme can cut. Matrixin is a class of enzyme that belong to the zinc-metalloproteinases family involved in the degradation of the extracellular matrix [145]. To test cleavage success we ran an HPLC on IDP4 and IDP4δ to determine their retention times. (Buffer: 200 mM NaCl, 50 mM TRIS, 5 mM CaCl2, 1 mM ZnCl2, *p*H = 7.5, peptide conc. = 85μM, enzyme conc. = 0.85μM, total Volume = 100 μl, MMP-9 Enzyme: lot # 09051736)). We treated the peptide solution with MMP-9 enzyme and HPLC was obtained at 24 hrs and 6 days. Control samples without addition of MMP-9 were also run to

check for non-specific cleavage over the reaction time. Indeed, upon incubation with the MMP-9 enzyme, the IDPA is cleaved with a shortened peptide sequence (Supplementary Fig. 3.4). We term the remaining amphiphile, which includes the hydrophobic domain, as IDPA4Δ 2×12 and the cleaved peptide as IDP4δ (Fig. 3.5).

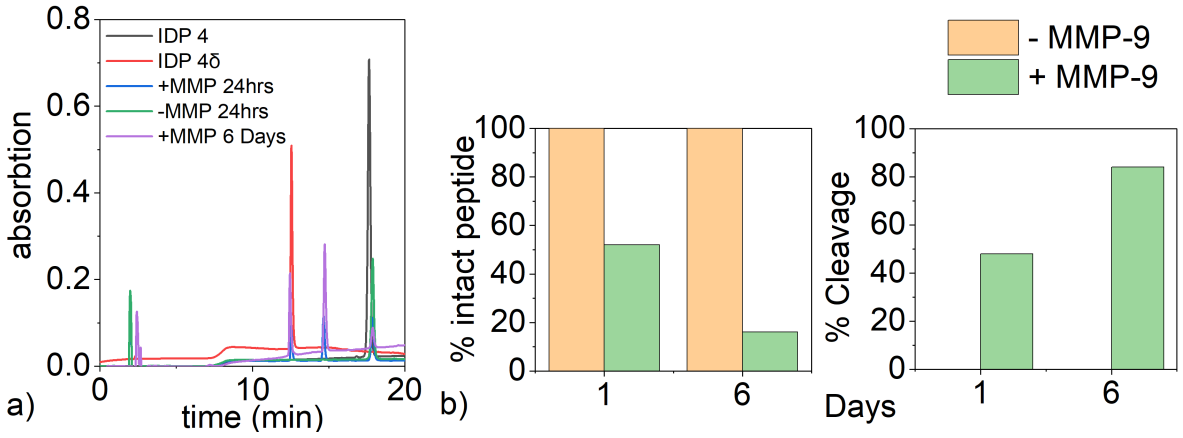

Figure 3.4: **Enzymatic cleavage with MMP-9 Enzyme.** a) HPLC retention times for IDP4 treated with MMP-9 at different time spots and IDP4δ as reference b). b) Diagram for intact and cleaved peptides after 1 and 6 days.

Name	Sequence	Tail Numbers	Total MW	isolelectric point
IDPA1 2×12	GDGEEGASRHEYEGKEAE	2×12	2442.69	*p*H 3.8
IDPA1 2×14	GDGEEGASRHEYEGKEAE	2×14	2498.79	*p*H 3.8
IDPA1 2×16	GDGEEGASRHEYEGKEAE	2×16	3554.89	*p*H 3.8
IDPA1 1×14	GDGEEGASRHEYEGKEAE	1×14	2160.26	*p*H 3.8
IDPA1 1×16	GDGEEGASRHEYEGKEAE	1×16	2188.31	*p*H 3.8
IDPA1 1×18	GDGEEGASRHEYEGKEAE	1×18	2216.38	*p*H 3.8
IDPA2 2×12	DEEEEEEGGGASYGARHK	2×12	2442.69	*p*H 3.8
IDPA3 2×12	GDGEEGASRGEYEGKEAE	2×12	2362.60	*p*H 3.8
IDPA4 2×12	WAGGASGPLGLAGYDEERE	2×12	2427.81	*p*H 3.6
IDPA4 2×12	WAGGASGPLG	2×12	1364.72	x

Table 3.1: **Key parameters and notation for IDPAs**

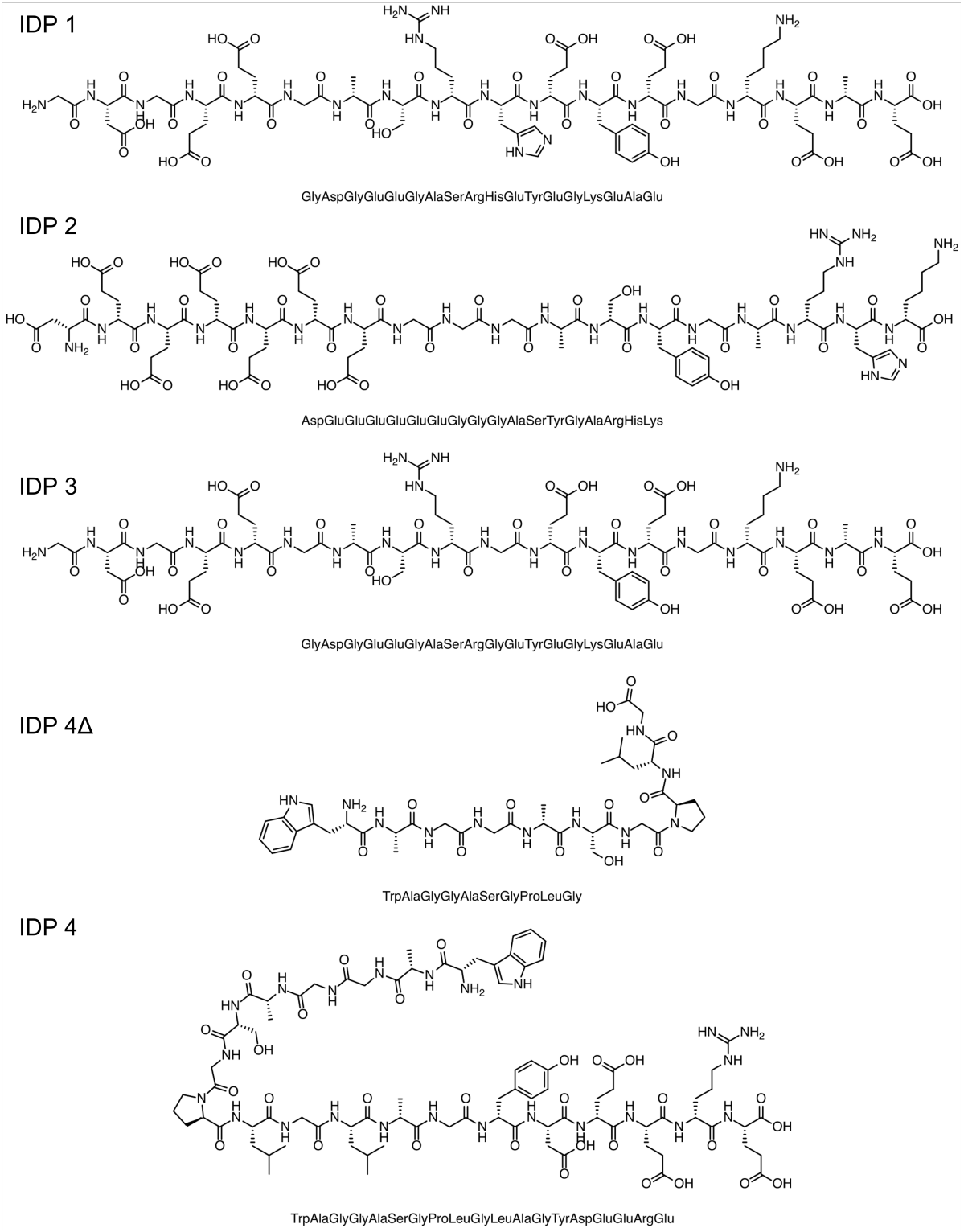

Figure 3.5: **Molecular structure for peptide sequences.** Structures are shown for IDP 1, 2, 3, 4Δ and 4, below three letter code.

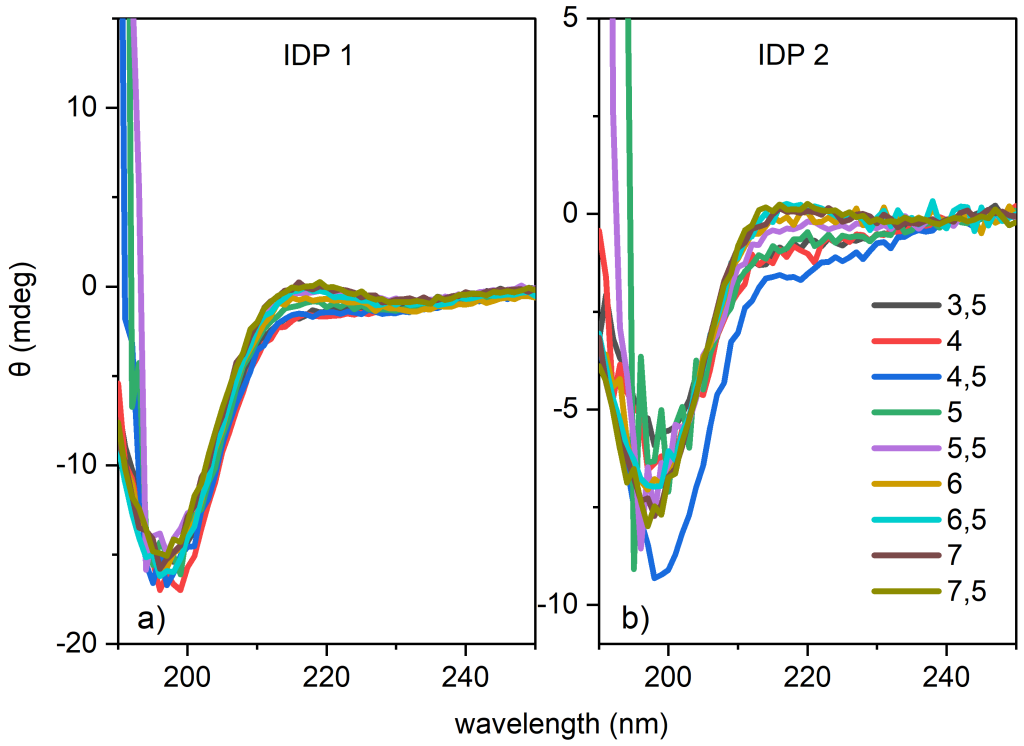

Figure 3.6: **CD measurements showing random coil spectrum.**

3.3.1 IDPA disorder analysis

We used various techniques to determine the disorder of the hydrophilic IDPs. Experimentally, CD was used to determine the disorder for various *p*Hs for IDP1 and 2. The peptide was measured in the presence of 10mM sodium acetate and sodium phosphate buffer for *p*H 3.5-7.5, respectively. The signal presents a random coil spectrum for all IDPs indicating unstructured (disordered) peptides and no secondary structure for relevant *p*Hs.

Computationally, we evaluated the probability of the IDPs to be disordered using IUPred2/ANCHOR2 [139], Dis*p*Hred [146], and Cider [140]. ~~We assumed that the disorder analysis of the pure IDPs without the hydrophobic tails is a good approximation for the whole IDPAs.~~

IUPred2/ANCHOR2 [42] confirmed high probability for disorder for IDP1-3 (Fig. 3.7, 3.8, 3.9). Exchanging one amino acid (histidine to glycine at position 10) changes disorder predictions - especially at the vicinity of the isoelectric point, there is an indication for some ordering for IDP3.

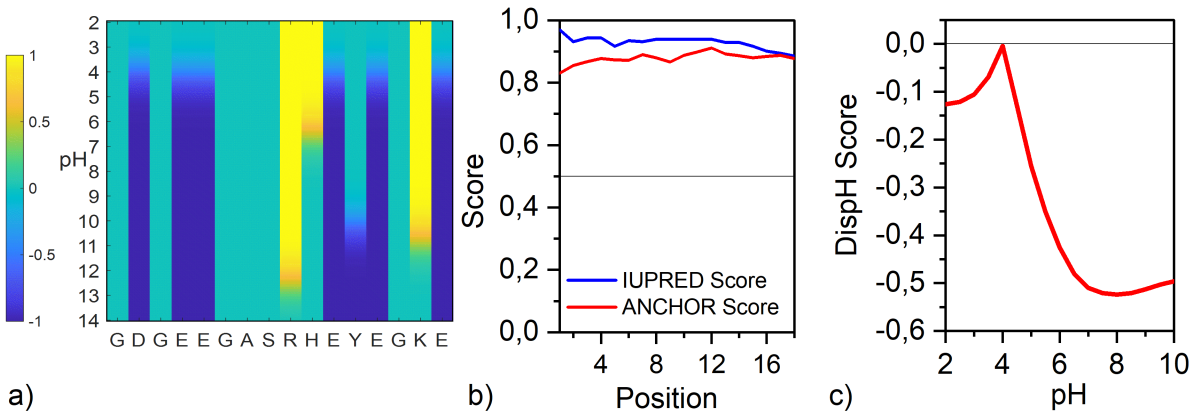

Figure 3.7: **Charge and disorder analysis for IDP1.** a) Charge state for each amino acid at different pHs. b) Iupred/Anchor analysis shows disorder tendency (threshold: 0.5) for IDP [42], further analysis with Netsurf supports this statement [147]. (c) *p*H dependent disorder analysis with DispHred [148] predicts disorder tendency for all pHs.

IDP4 is predicted to be disordered for all pHs (Fig. 3.10), and the cleaved IDP4Δ is marginally disordered for all pHs (Fig. 3.10) - in this sequence, no amino acid can get protonated.

Additionally, we calculated κ for the CIDER analysis for IDP1 and 2. For IDP1, we got relatively low values of κ that point toward well-mixed sequence variants, and IDP2 relatively high values indicating that oppositely charged residues are segregated in the sequence (Fig 3.12).

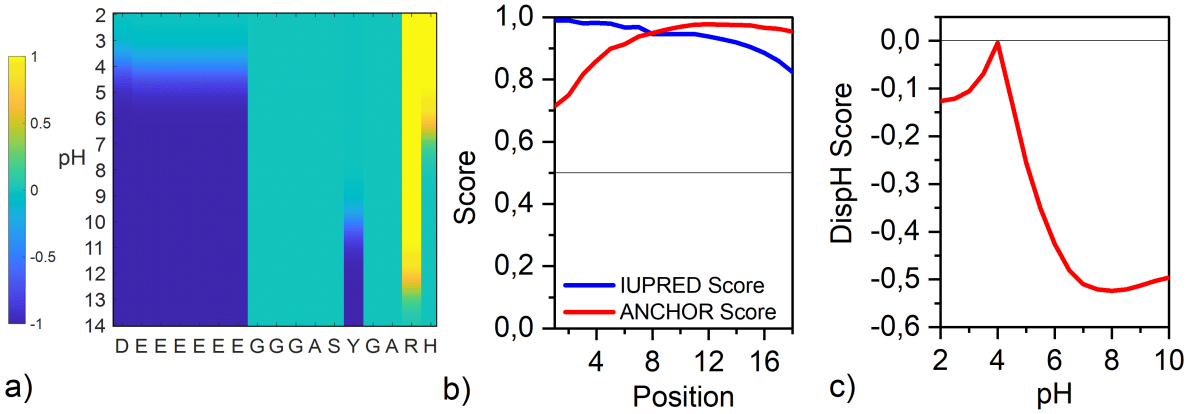

Figure 3.8: **Charge and disorder analysis for IDP2.**a) Charge state for each amino acid at different pHs. b) Iupred/Anchor analysis shows disorder tendency (threshold: 0.5) for IDP [42], furher analyis with Netsurf supports this statement [147]. (c) *p*H dependent disorder analysis with DispHred [148] predicts disorder tendency for all pHs.

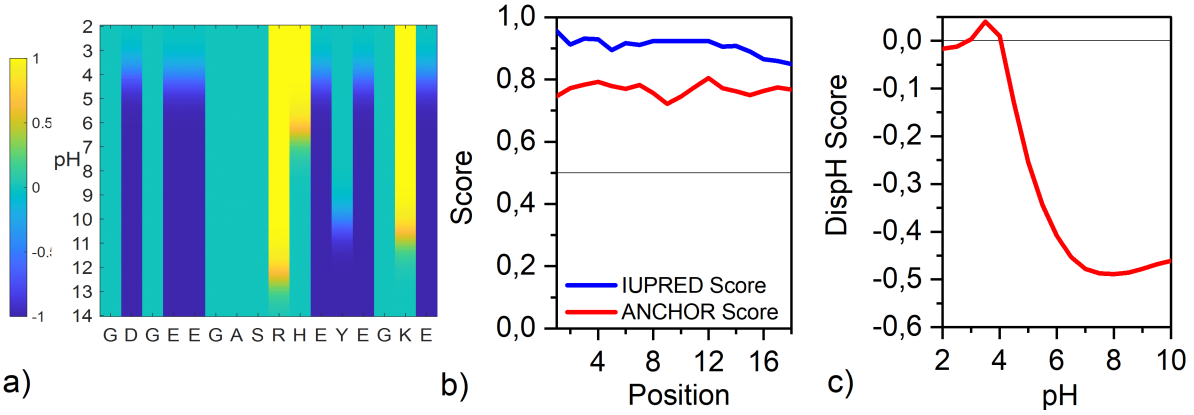

Figure 3.9: **Charge and disorder analysis for IDP3.** a) Charge state for each amino acid at different pHs. b) Iupred/Anchor analysis shows disorder tendency (threshold: 0.5) for IDP [42], furher analyis with Netsurf supports this statement [147]. (c) *p*H dependent disorder analysis with DispHred [148] indicates ina possible ordering and lack of disorder the vicinity of the isoelectric point.

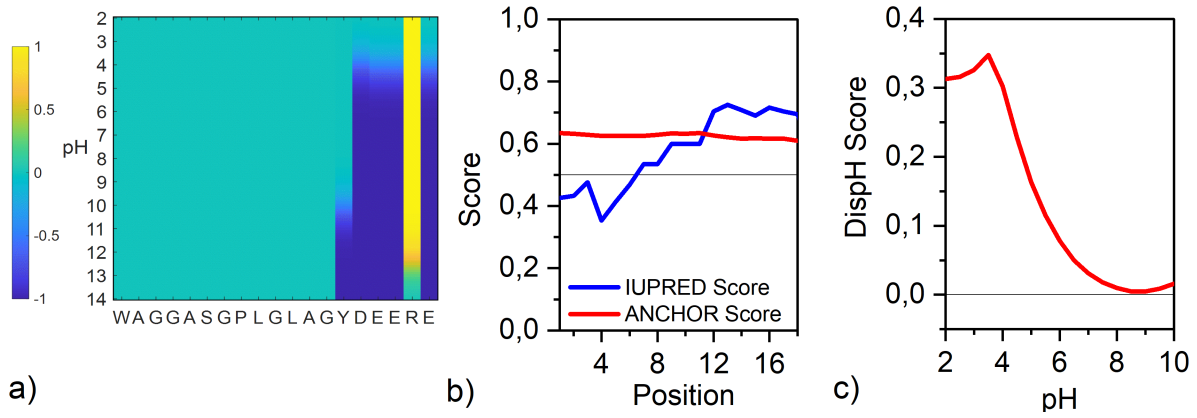

Figure 3.10: **Charge and disorder analysis for IDP4.** a) Charge state for each amino acid at different pHs. b) Iupred/Anchor analysis shows that IDP is on the threshold to be disordered [42], furher analyis with Netsurf supports this statement [147]. (c) *p*H dependent disorder analysis with DispHred [148] predicts no disorder tendency for all pHs.

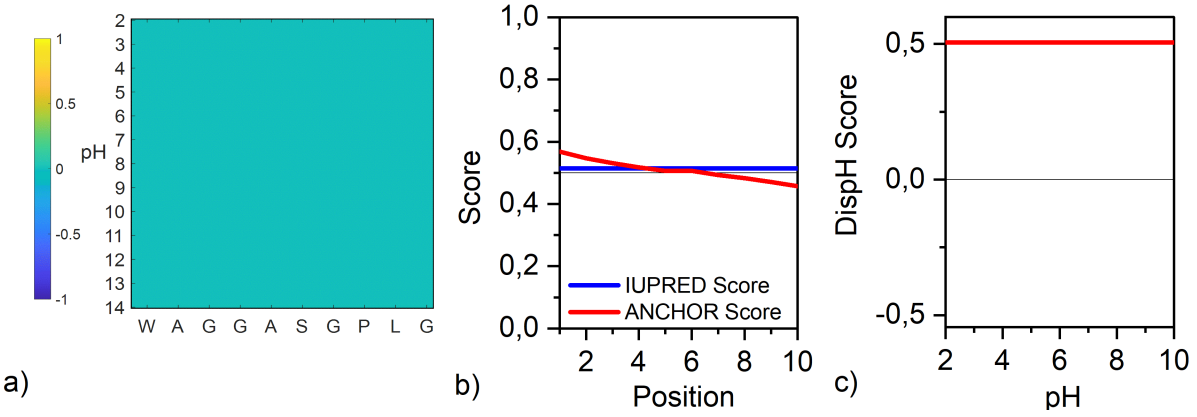

Figure 3.11: **Charge and disorder analysis for IDP4Δ.** a) Charge state for each amino acid at different pHs. b) Iupred/Anchor analysis shows disorder tendency (threshold: 0.5) for amino acids after the cleavage site [42], furher analyis with Netsurf supports this statement [147]. (c) *p*H dependent disorder analysis with DispHred [148] predicts disorder tendency for all pHs except in the vicinty of the isoelectric point.

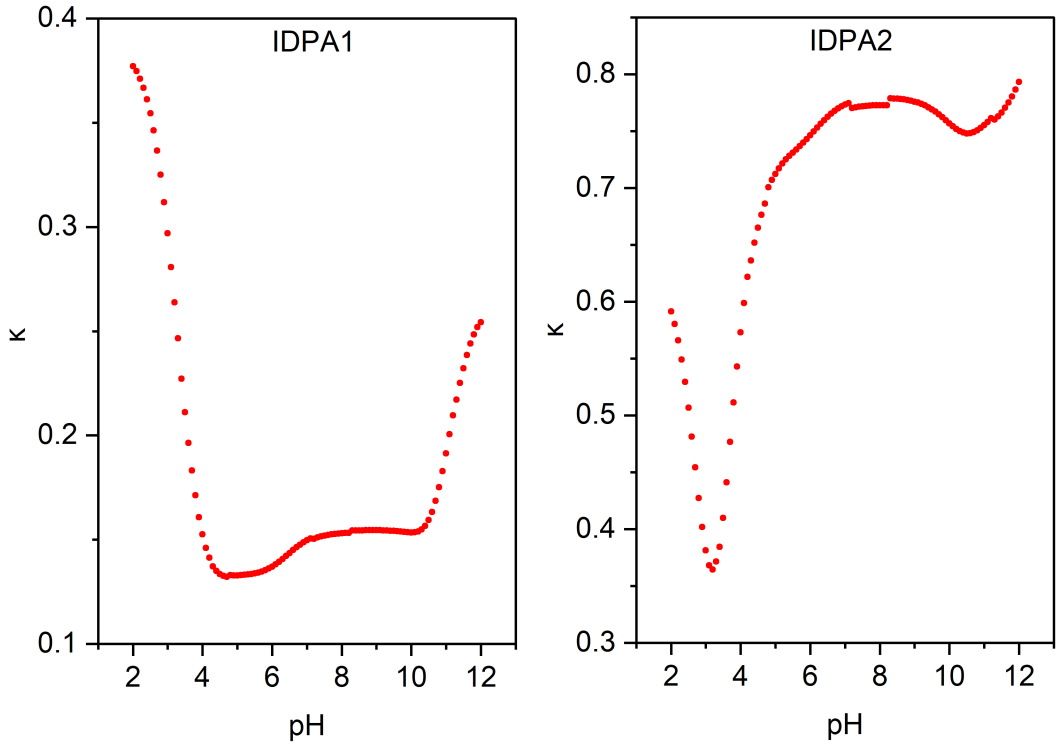

Figure 3.12: **κ for IDP1 and 2 at various pHs.** IDP1 has small κ values under 0.4 for all *p*H pointing towards counterbalance between intrachain electrostatic repulsion and attractions,, while IDP2's $\kappa > 0.4$ for all pHs. Data is produced using formulas presented Das et. al, 2013 [32]

We need to point out that the disorder analysis is done on the sequence alone and not on the full IDPA. We assumed this is a good approximation for confirming the IDPs when conjugated to the hydrocarbon chains. We verified that by measuring the distance of Tyr at position 14 and Trp at position 1 of IDP4 and IDPA4 2×12 using FRET and found no difference between them (Fig. 3.13).

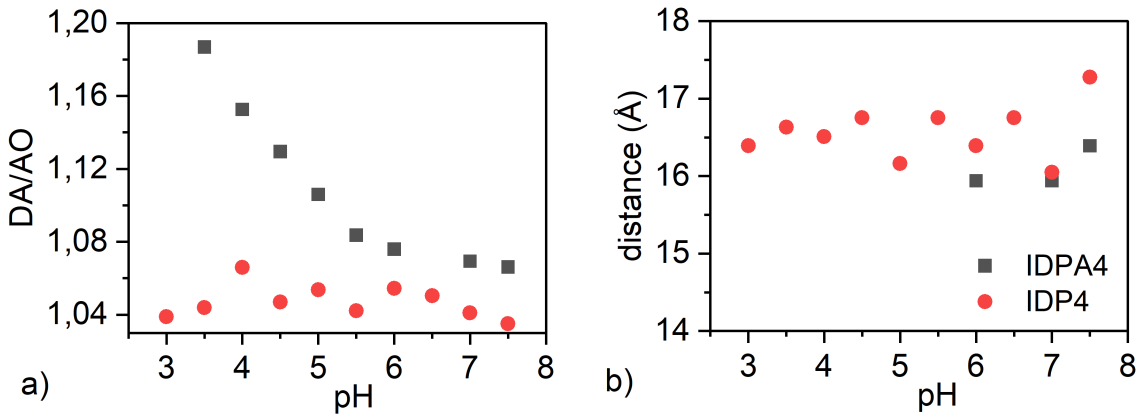

Figure 3.13: **FRET measurements of IDP4 and IDPA4 2×12.** a) Fluorescence spectra for IDP4 and IDPA4 2×12 b) Extracted distances show that the distance between Tyr at position 14 and Trp at position one is not changing through the *p*H range of 3.5 – 7.5. A small decrease in the distance was found in IDPA4 2×12 compared to IDP4 at *p*H 6.5-7.5. We could not calculate the energy transfer at the lower *p*H of IDPA4 2×12 due to a change in the spectrum profile of the WY dipeptide reference. Nevertheless, an increase in the fluorescence spectra for IDPA4 2×12 was seen in the lower *p*H of 3.5-6.5, suggesting a decrease in the donor-acceptor mean distance.

3.3.2 Micellar structures at high *p*H

The structures of IDPA1 and 2 2×12 were compared at high *p*H (6.5). Both amphiphiles are forming micellar structures but with different radii at this *p*H. Their micellar systems were determined using SAXS. A core-shell model for spheres was used to fit the SAXS data. We found that IDPA2 2×12 has a significantly smaller radius (IDPA1 2×12: 3.6nm, IDPA 2 2×12: 2.1nm) and assumed, due to the same hydrophobic domain, the difference in radii is thus originating from a smaller peptide shell (IDPA1 2×12: 2.2.nm, IDPA 2 2×12: 0.9nm, see Fig. 3.14a lower inset). Additionally we performed PDDF analysis to confirm this hypothesis (Fig. 3.14 upper inset).

The significantly larger peptide shell of IDPA1 2×12 shows that sequence ordering plays a dominant role here, as IDPA1 and 2 2×12 have the same amino acids. Here, charges are either homogeneously distributed throughout the sequence (IDPA1 2×12), or all positive/negative charges are on one end. Thus, we propose that the compactness of IDPA2 2×12's shell can be explained by electrostatic interactions of these to oppositely charged ends and result in some transient back folding (Fig. 3.14b). Analysis of κ for both IDPAs support this hypothesis. Thus, we showed

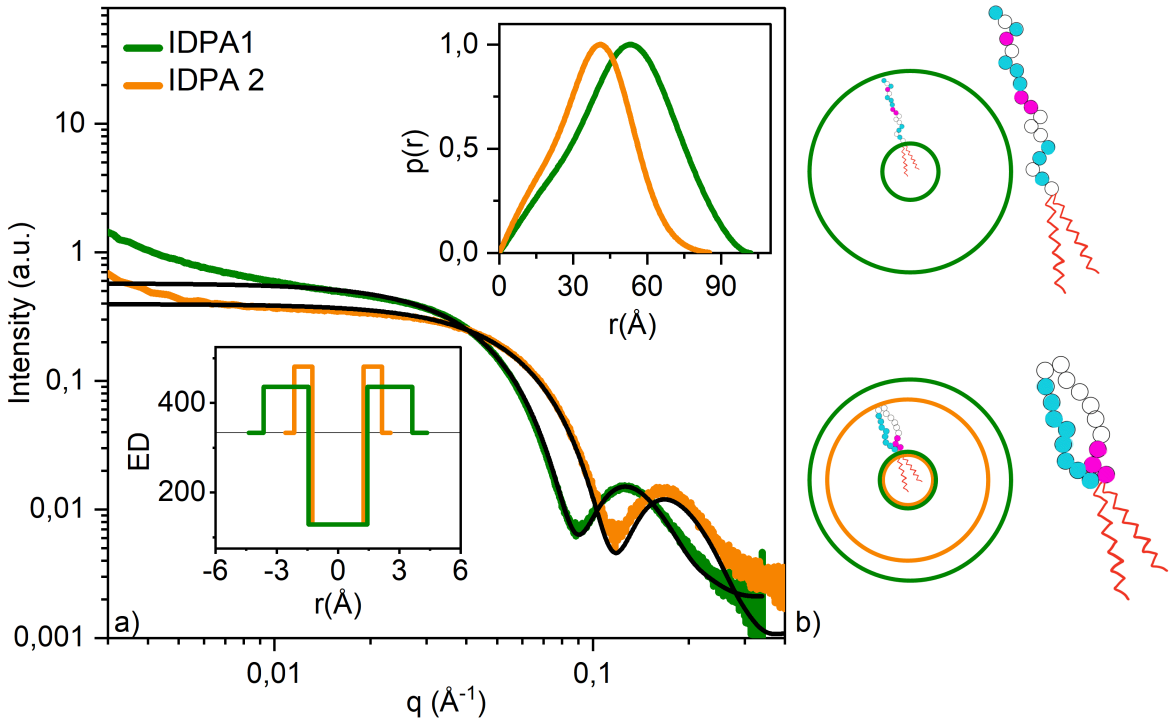

Figure 3.14: **IDP head conformation as a function of sequence.** a) SAXS profiles show smaller radii for IDPA1 2×12 (green) than IDPA2 2×12 (orange) 2×12 at pH $= 6.35 \pm 0.5$. Micellar core-shell form factor fits are shown in black line with parameters detailed in table 1. Lower inset: Electron density profile used in the fit. Upper inset: radius of gyration results of PDDF (q-range for fit: IDPA 1 2×12: 0.02-0.22^{-1}, IDPA2 2×12: 0.02-0.24^{-1}). b) Representation of micellar sphere with IDPA 1 2×12 (green) and IDPA 2 2×12 (orange) with significant different sizes of IDP coronas and illustration of backfolding in IDPA2 2×12 (lower cartoon) in comparison to IDPA 1 2×12 (upper cartoon). Pink circles indicate cationic, blue anionic and white – neutral amino acids.

that the peptide headgroup's charge patterning plays a significant role in their conformation and plasticity.

3.3.3 Phase transition and charge positioning

After comparing IDPA1 and IDPA2 2×12 at high pH, we took a closer look at the entire pH range. As charges are summing up to zero at the isoelectric point and thus there is minimal electrostatic repulsion between the amino acids, peptide-peptide interactions are favorable over peptide-water interactions [149, 150]. IDPs tend to collapse and become insoluble at this pH.

We analyzed the self-assembly of IDPA1 and 2 2×12 using Cryo-TEM, turbidity measure-

ments, and SAXS (Fig 3.15). IDPA1 and 2 2×12 are insoluble close to the isoelectric point and become soluble and form monodisperse nanoparticles (spherical and/or cylindrical micelles) in solution for higher and lower *p*Hs. We could confirm that in the vicinity of the isoelectric point, the IDPAs are collapsing into condensed phases. The SAXS data for IDPA1 2×12 shows vague peaks that point towards a hexagonal phase (Fig 3.15), thus we assumed these are bundles of hexagonal packed cylindrical micelles. This condensation shows a clear difference between IDPA1 and 2 2×12: IDPA1 2×12 has a relatively small interval of transition (*p*H 4.2-4.6), while IDPA2 2×12 shows a significantly more comprehensive range for the transition (*p*H 4.2-6.5). Thus, this transition is also sequence-dependent, and the charge patterning not only influences the peptide headgroup conformation at physiological pH but also pH-dependent phase transitions.

Considering our findings from high *p*H measurements and previous findings [89], an explanation for the broader transition for IDPA2 2×12 is that the more compact formation of the backfolded peptide is less-prone to interact with other IDPAs in an intimate environment. Moreover, if they interact, they need a complete overlap of the peptide to have attractive electrostatic interactions, while IDPA1 2×12 needs to be partially overlapping.

3.3.4 Spherical to rod-like micelle transition

In the next step, we took a deeper look into this phase transition from wormlike to spherical micelles. Here, the balance between the hydrophilic headgroup and the hydrophobic tail group plays an essential role [151] like already described by Israelchvili [74]. We wanted to understand how different hydrophobic tails can alter the transition and designed IDPA1 with three different tail lengths (2×12,2×14 and 2×16).

We measured IDPAs at different *p*Hs using SAXS. We saw a transition between two curve regimes - spherical and wormlike (Fig. 3.17). However, why are we so sure that one is a sphere and not a cylinder? Spherical and cylindrical form factors have different curve features, especially in the low *q*-region. Fig. 3.22 shows an excellent example of how a spherical form factor fits the SAXS data curves while a cylindrical form factor is not. Especially in the low *q*-region there is a

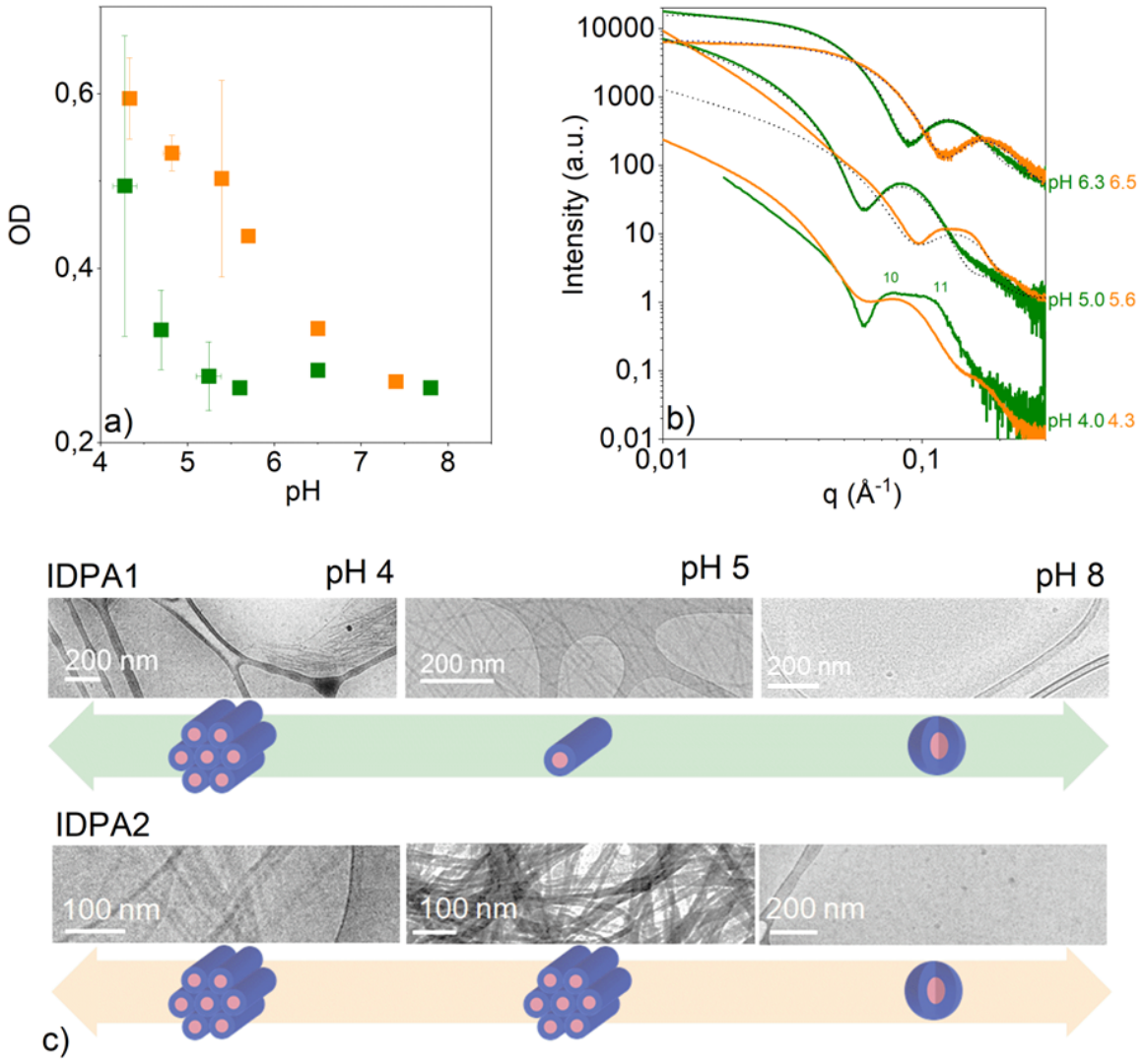

Figure 3.15: ***p*H dependent condensation of mesophases - from bulk to dispersed phase.** a) Absorbance measurement shows high absorbance at the vicinity of the isoelectric point (*p*H 4), IDPA2 2×12 (orange) shows a significantly milder slope than IDPA1 2×12 (green) when transitions between the two states b) SAXS scattering for IDPA1 (green) and 2 2×12 (orange) at various pHs. Dotted lines show spherical/worm-like core-shell form factors. IDPA1 2×12 at *p*H 4 shows humps that point towards a hexagonal phase. c) Cryo-TEM pictures for IDPA1 2×12. Phase transition from spherical to worm-like micelles at *p*H 5. Aggregation of worm-like monodisperse micelles to bundles at the vicinity of the isoelectric point (*p*H 4).

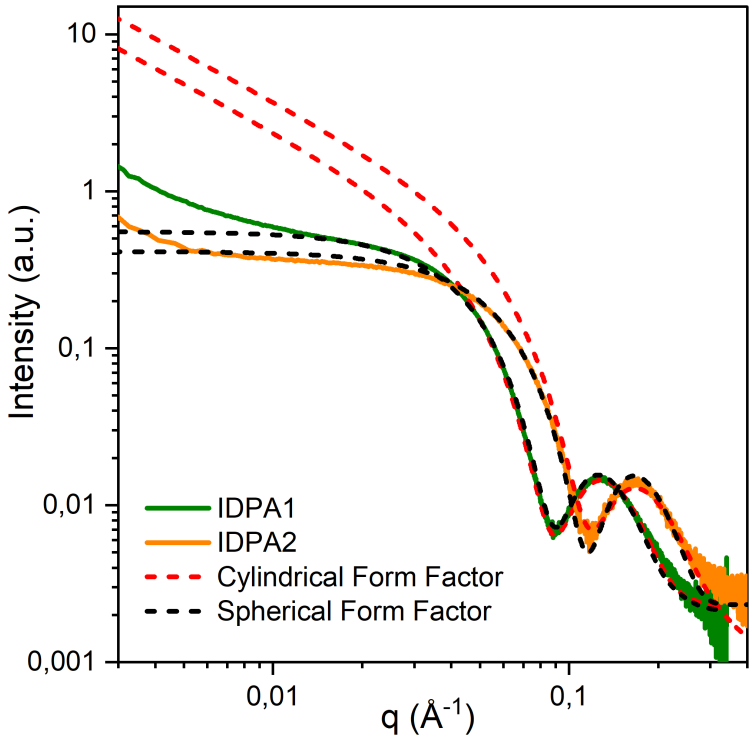

Figure 3.16: **Spherical and cylindrical form factor for IDPA1 and 2 2×12 at *p*H 6.** Especially for low q values, a spherical form factor captures the data very well. Small deviations in the spherical form factor are coming from interparticle interaction.

significant difference in form factors' slopes.

We found that the curve regimes can be fitted with a wormlike and spherical form factor, respectively, and the region in between as a superposition of both. We call the combination of the two mesophases the coexistence regime (Fig. 3.17. Interestingly, longer/shorter tails result in phase transition at higher pHs with a much broader/narrower range of transition (2×16: *p*H 4.7-7.8, 2×14: *p*H 4.7-7.5, 2×12: *p*H 5.7-6.0) between the two mesophases (Fig. 3.18).

We tested our hypothesis of a coexisting phase using singular value decomposition analysis. Following Asor et. al. [131] we calculated residuals, $R_k = \frac{1}{nm}\sum_{q_i=1}^{n}\sum_{p_j=1}^{m} R^2_{k,q_i,p_j}$, where m is the size of the scattering vector q and n are the number of *p*H steps, k are the singular vector components that were chosen to reconstruct the data matrix. Here, R_{k,q_i,p_j} was defined by $R_{k,q_i,p_j} = \frac{D_{q_i,p_j} - D_{kq_i,p_j}}{\sigma_{q:i,p_j}}$,

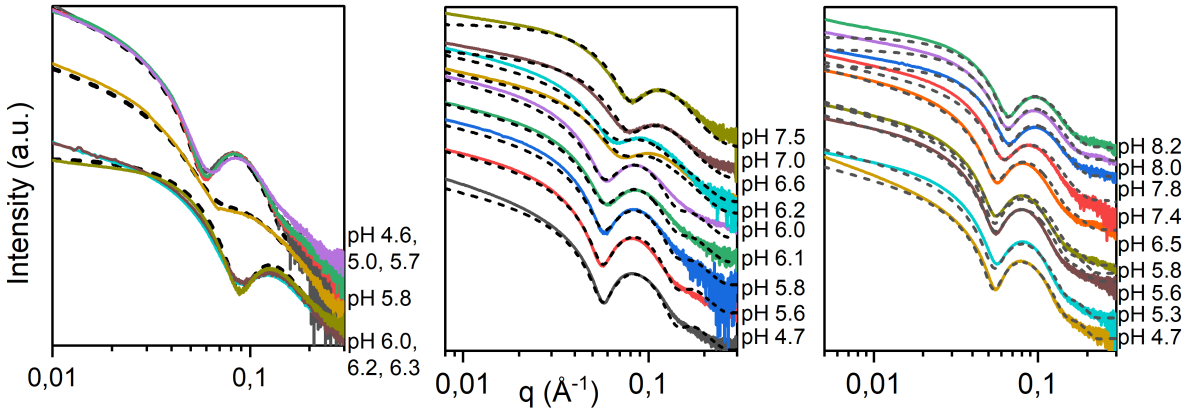

Figure 3.17: **Sphere to Cylinder transition.** Dotted lines show superposition of spherical (lowest line in each fit) and cylindrical form factors (highest line in each fit). Left panel: 2×12, middle panel: 2×14, right panel: 2×16

where D is the data matrix, in which each column represents a one dimensional scattering curve, $I(q,p)$ at every pH step p. D_k is the reconstructed data matrix using k singular orthonormal vectors, and each term (q_i, p_j) in the matrix σ corresponds to the measured standard error for the corresponding term in D. [131]. Cutoffs were taken for residuals, R, smaller as one as bigger values would mean that another vector is needed to represent the data. Thus we could show, how many distinct scattering patterns contribute to the polydisperse signal for the transition pH range described before. In our assumption, the SVD analysis is the upper bound of number of different phases in the coexistence regime.

But what is the origin of the coexistence? We conducted the results with the guidance of Prof. Michael Kozlov from the Sackler School of Medicine, Tel Aviv University. Previous research explained the phase transition from spheres and cylinders and the coexistence phase between them with an energy barrier that has to be overcome [152]. We can characterize cylindrical micelles by a mean length of L, depending on the excess energy of the two end caps of a micelle, E. In contrast, we assume E to be positive. Two tendencies compete over the mean length: One is to produce just one long micelle, which would minimize the number of endcaps in the system and the related energy. The second tendency is to break this long micelle into many smaller micelles. Such breakage would increase the number and, hence, the overall energy of the endcaps but allows for

distribution of the shorter micelles throughout the solution, the latter being entropically favorable. The endcaps of a cylindrical micelle and each half of the spherical micelles have two different energies and thus create an energy barrier. Thus between the two phases, there is an unfavorable but unavoidable transition region because of their different cross-sectional thicknesses [152]. The molecules in cylinders and micelles are packed differently and thus create other surface areas.

Upon the most straightforward approach, a micelle mean length will be exponential in E/kT (kT being a product of the Boltzmann constant and the absolute temperature), following $L\,exp(E/kT)$ The lower E, the shorter the micelles on average. Concise values of L thus correspond to spherical micelles.

We can now assume that as long as the average micelle length, L, is larger than some value, L_c, we identify the solution as consisting of only cylindrical micelles. And, we see the purely cylindrical micelle system for L going down to a small value of L_m. We can identify the range $L_m < L < L_c$ as a coexistence of cylinders and spheres.

However, under which condition is what favored? The answer lies in charge of the peptide monolayer. When the charge increases, spontaneous curvatures increase and make the endcap more energetically favorable, decreasing the energy barrier,E. To bring the endcap energy, E, to a small enough value, we have to generate a lipid charge density, S, which would produce an addition to the spontaneous background curvature. If we change the chain length, we decrease the thickness mismatch between the endcap and the cylindrical part of a micelle and, therefore, lower the initial energy barrier. Thus we need less charge to overcome the energy barrier and can ease up the cylinder-to-sphere transition. This explains why longer chains have a broader coexistence region. This coexistence region must be understood as a smooth transition between the two phases rather than a state of two existing independent species.

The coexistence region begins when the energy barrier of forming a spherical micelle out of a cylindrical one is such that the characteristic time of this event is comparable with the time of observation. When we reach the end of the observation region, the time for the transition must be now shorter than the observation time.

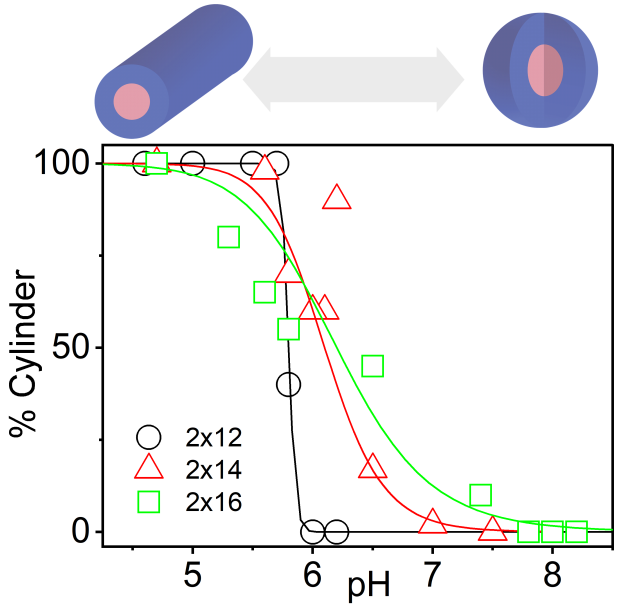

Figure 3.18: ***p*H dependent phase transition for different lipid chain length.** The *p*H dependent range of transition from worm-like (pH<4.7) to spherical micelles (pH>7.5) is broadening with increasing tail length (indicated in the legend). Phases in between are superposition of form factors and interpreted as coexistence. Lines represent a Hill function fit.

Our result shows that for the IDPA1 transitions, 2-3 coexisting scattering vectors are needed for proper reconstruction. For 2×12 and 2×16, there are up to three different phases, and for the 2×14 IDPA1, only two different phases are required by the SVD analysis (Fig. 3.19). Going back to our initial assumption of a coexistence phase, this result supports the model of a linear superposition of spherical and wormlike micelles. Nevertheless, what is the third phase for 2×12 and 2×16 remains unclear? One option can be an "in-between" phase, like an ellipsoidal phase, between rod and spherical phase, that did not captured by our fit even by synchrotron's SAXS data. Thus, tail length influences micellar to rod transitions and the width of the coexistence regions between those two phases.

3.3.5 Role of the tail size

After examining the influence of tail length alterations, we changed the number of hydrocarbon chains. We designed three IDPAs with a single tail that differ in tail lengths ((1×14, 1×16, 1×18).

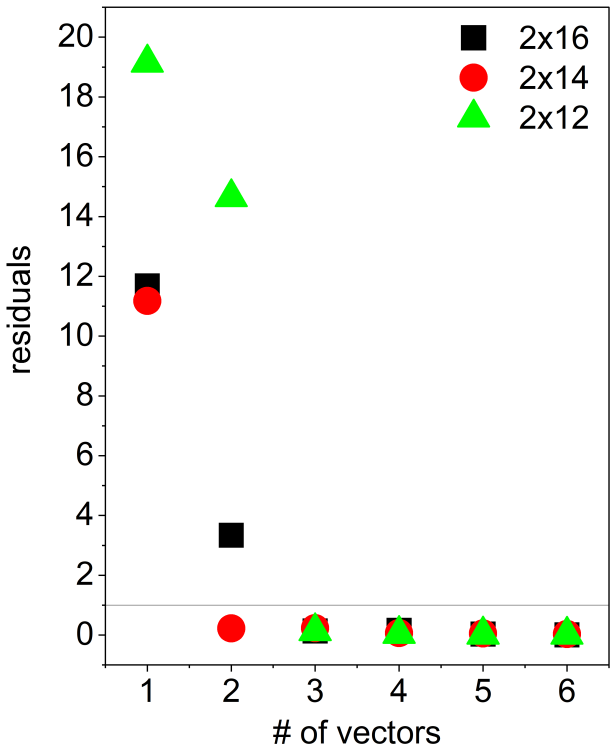

Figure 3.19: **Singular value decomposition (SVD) analysis.** SVD of *p*H dependent SAXS data for spherical to worm-like micelle transition. The black line indicates the cutoff where the residual is equal to 1. [131]

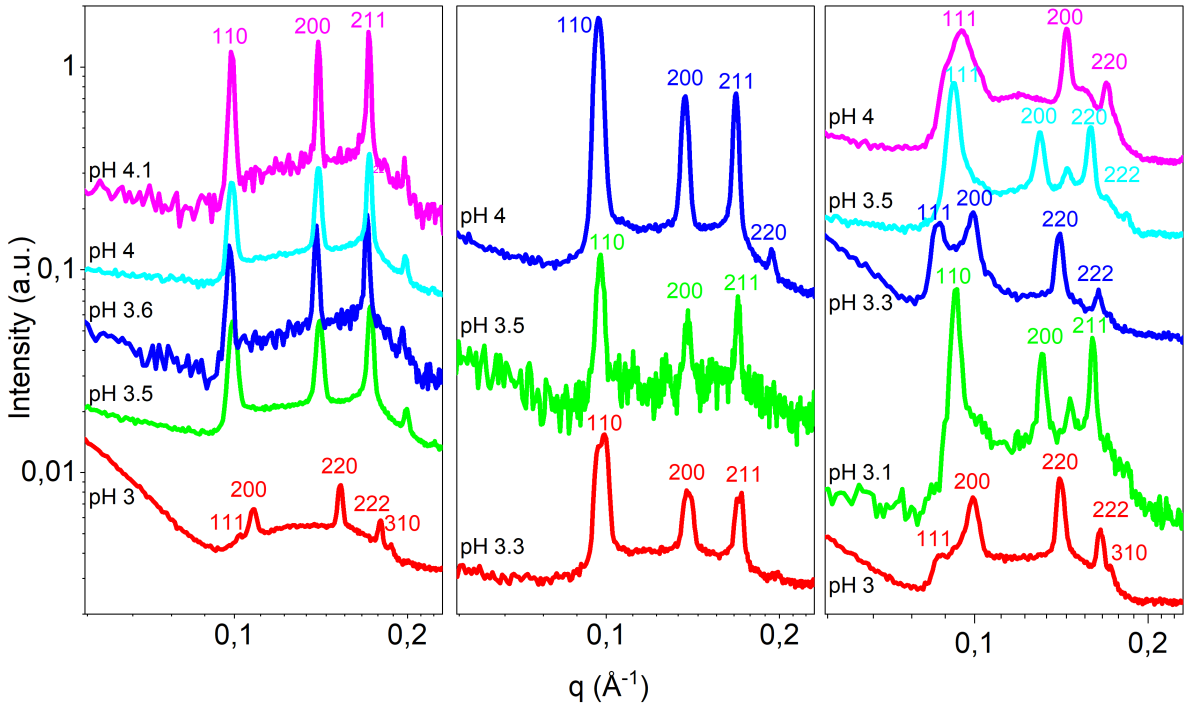

Figure 3.20: **Scattering Signal for single tailed IDPAs.** a) 1×14 b) 1×16 c) 1×18. Every IDPA was measured at different *p*H values, data was radially integrated and peak position was extracted using a Lorentian fit. Miller indices (see 1.5) are shown for BCC and FCC lattices.

All these IDPA had the same hydrophilic headgroup (IDPA1). When comparing two tails to one, we found that the scattering pattern in the vicinity of the isoelectric point points towards a strong scattering "spackle" pattern while the singled tailed IDPAs self-assemble into spherical micelles for lower and higher pHs. The scattering peaks fit the miller indices of Face Centered Cubic (FCC) and Body-Centered Cubic (BCC) Bravais lattices (Fig. 3.21b). When comparing the lattice distance of the crystals, we find that they are in good accordance with the calculated tail lengths ($\ell < \ell_{max} = (1.54 + 0.1265nm)$ using [74]). Specifically, the longer the tails it results with bigger lattices (Fig. 3.21c) and d).

Now, when we subtract the calculated hydrophobic core from the lattice parameter, we can extract the approximate size of the hydrophilic peptide domain. The hydrophobic core, ℓ, is calculated using $\ell < \ell_{max} = 1.54 + 0.1265nm$ as an approximation for hydrocarbon tail extension [74].

The calculated value of the hydrophilic peptide domain of 2.7*nm* is in the same order of magnitude but a little bit smaller than the IDP size of micellar spheres fitted (Fig. 3.22) at intermediate *p*H (see dashed lines in Fig. 3.21c) and d) and table 1). An overlap between the nearest neighbors within the crystal can explain the reduced value of the hydrophilic shell dimension. Supporting this result is the fact that there must be short-ranged attractive interactions between the peptides in the crystals to stabilize the crystalline structure in excess buffer. To conclude, reducing two tails to one tail results in a change in the crystalline self-assembly in the vicinity of the isoelectric point. Here single-tailed IDPAs are forming micellar spheres that are arranged in monodisperse crystals.

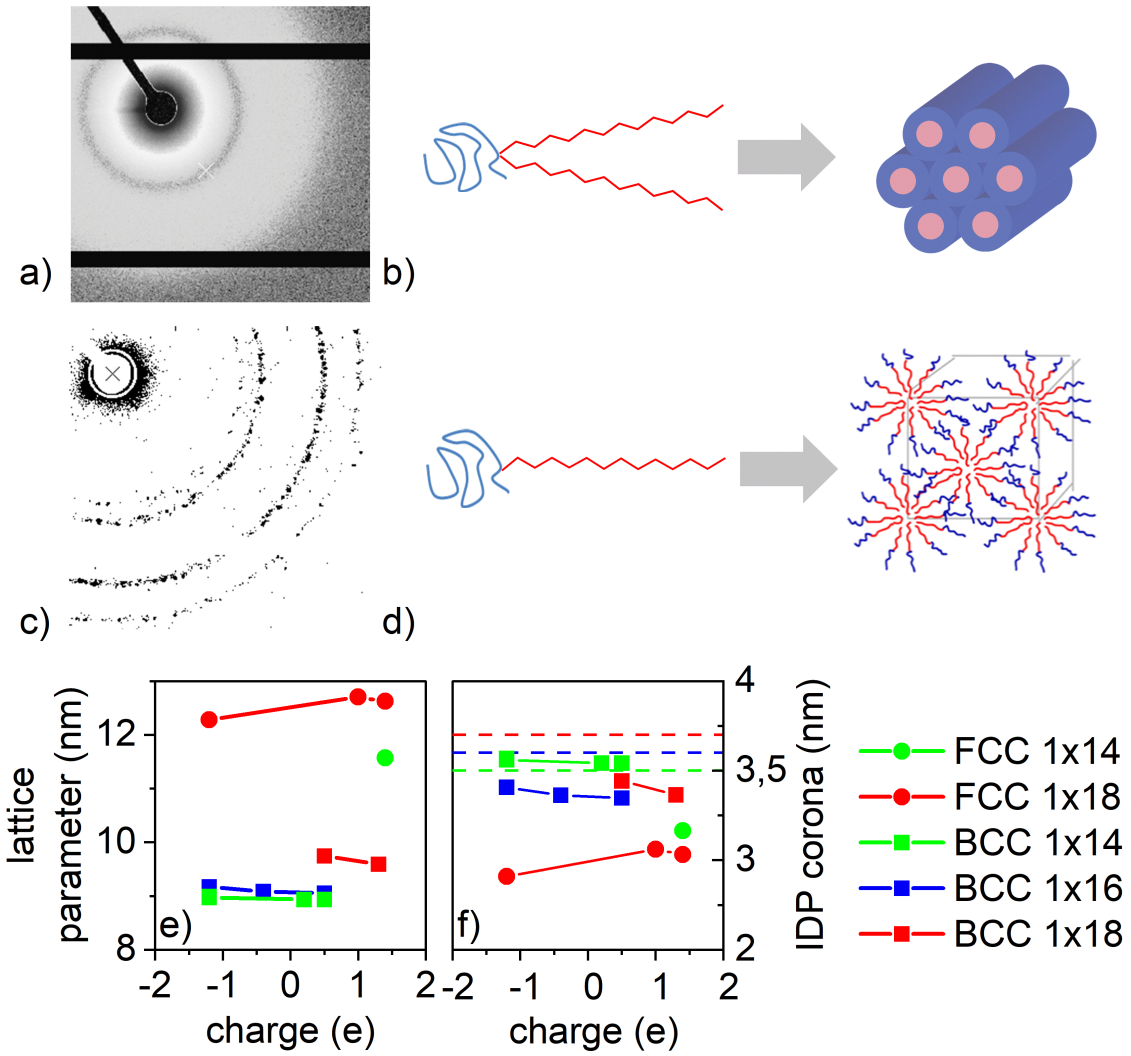

Figure 3.21: **Formation of liquid crystals at isoelectric point (*p*H 3.8) for single tailed IDPAs with different tail lengths.** 2D SAXS pattern for (a) double and single (c) tailed IDPAs at isoelectric point (*p*H 4) showing hexagonal and FCC phases (see 1.5). (b),and (d) are corresponding cartoons illustrating the formation of mesophases from the double and single tailed IDPAs, respectivly. Lattice parameters (d) for (e) BCC and (f) FCC phases from integrated 1D patterns for single tailed IDPAs near isolelectric point where found by extracting peak position via gaussian fit. Charge is calculated via summation of amino acids's charges at various pHs. Unit cell dimensions are directly measured from SAXS correlation peaks positions. Nearest neighbours (dashed lines) are extracted using $d\sqrt{2}/2$ for FCC and d for BCC. IDP headgroup layer sizes for 1×14, 1×16 and 1×18 IDPAs are extracted by subtracting the calculated tail length (ℓ_{max}, see text) from the lattice parameter.

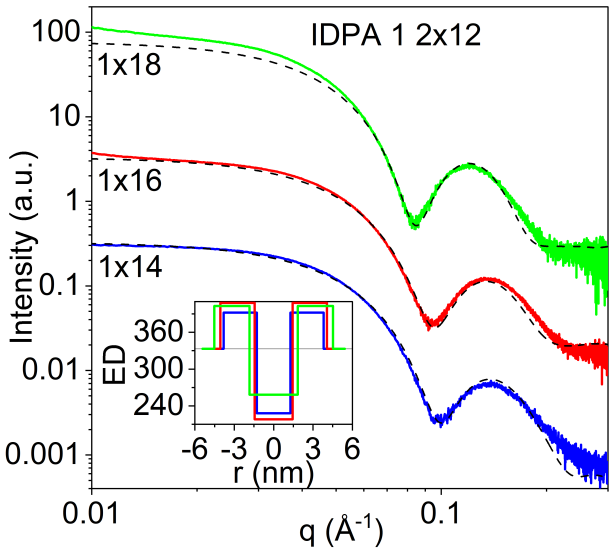

Figure 3.22: **SAXS signal and fits for single tailed IDPAs.** Dotted lines shows spherical form factor fit, Inset shows electron density profile for all three IDPAs. Data was fitted with X+ [128] using a spherical form factor.

3.3.6 Sequence Alterations

Next, we changed the sequence to a single amino acid. We found that if we exchange the histidine in IDPA1 2×12 for a glycine (IDPA3 2×12), the phase transition from spherical to wormlike micelles shifts from *p*H 5.4 to *p*H 5.8 (Fig. 3.23), but the observed phases remained the same. This can be explained by the slight shift of charge distribution at the *p*H regime; histidine has pK_a of 6.0 while glycine stays neutral. When comparing the net charge difference between IDPA1 and 3 2×12 we would expect the phase transition to happen at *p*H 4.9 for IDPA3 2×12 (Fig. 3.23a). Surprisingly, the experiments showed that the transition happen at *p*H 5.4 for IDPA3 2×12. The change in transition *p*H can be explained by a free energy model for electrostatic repulsion [89].

In our model, the energy associated with the hydrophilic region's charge density and the energetic price paid for inducing a curvature that deviates from the intrinsic one is competing. The net charge decreases when the *p*H is lowered, and the hydrophilic peptide can get denser. As a cylinder has a more favorable morphology for intrinsic curvatures, a more compressed peptide layer can facilitate the phase transition from the sphere to the cylinder when lowering the *p*H net charge. In our case, where we see two IPDAs transitioning at two different net charges, we need to understand

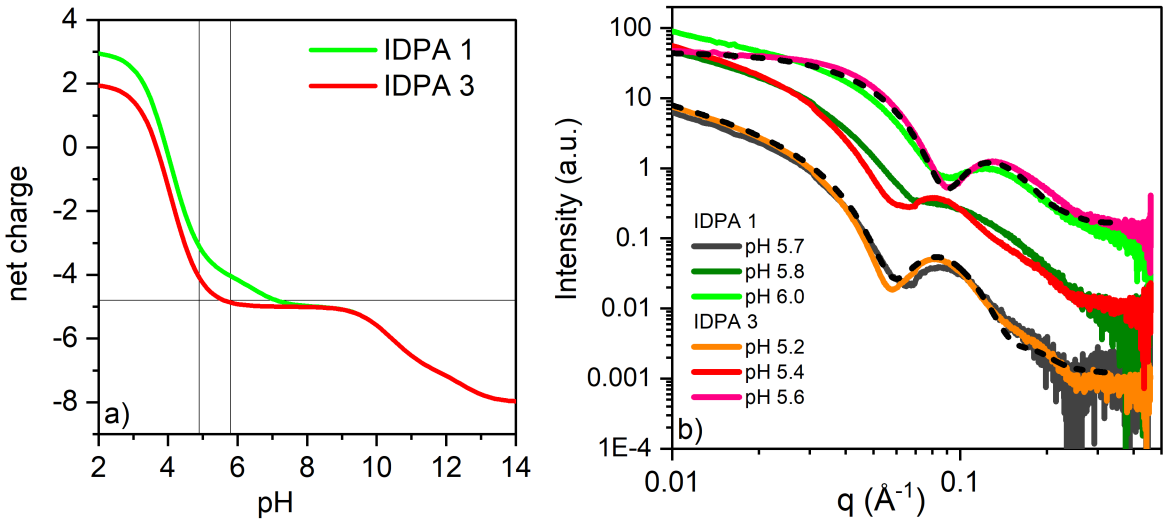

Figure 3.23: **Spherical to worm-like micelle transition for IDPA1 and 3 2×12.** a) *p*H dependent charge projection predicts IDPA3 2×12 to transition at *p*H 5.8 b) Experimental SAXS data shows transition at *p*H 5.4.

that the charge density is not just on the surface. However, each amino acid within the peptide contributes, depending on their vicinity to the peptide-tail interface. Thus, it makes a difference if we exchange either an amino acid at the very end of the peptide chain or, as in our case, in the middle of the sequence, which has a lower influence on the phase transition [89].

3.3.7 Salt alterations

So far, we have looked into phase transitions induced by altering the *p*H. Another method to tune self-assembly of charged molecules is salinity. Ions in solution screen the electrostatic interactions between charged amino acids and thus decrease repulsion. To analyze and quantify these interactions, we have used Kratky analysis. We found that the compactness of the IDPAs varies with increasing NaCl salt concentration. We found increasing slopes for high q values when increasing the chain lengths. High slopes stand for an unfolded domain that could be found for increasing salt concentration. The longer the tails get, the more pronounced the trend. Thus for higher salt concentration IDPAs are more unfolded than at low salt concentrations. Thus IDPA headgroups seem to expand for higher salt concentration. We relate the increase to inter-molecular charge

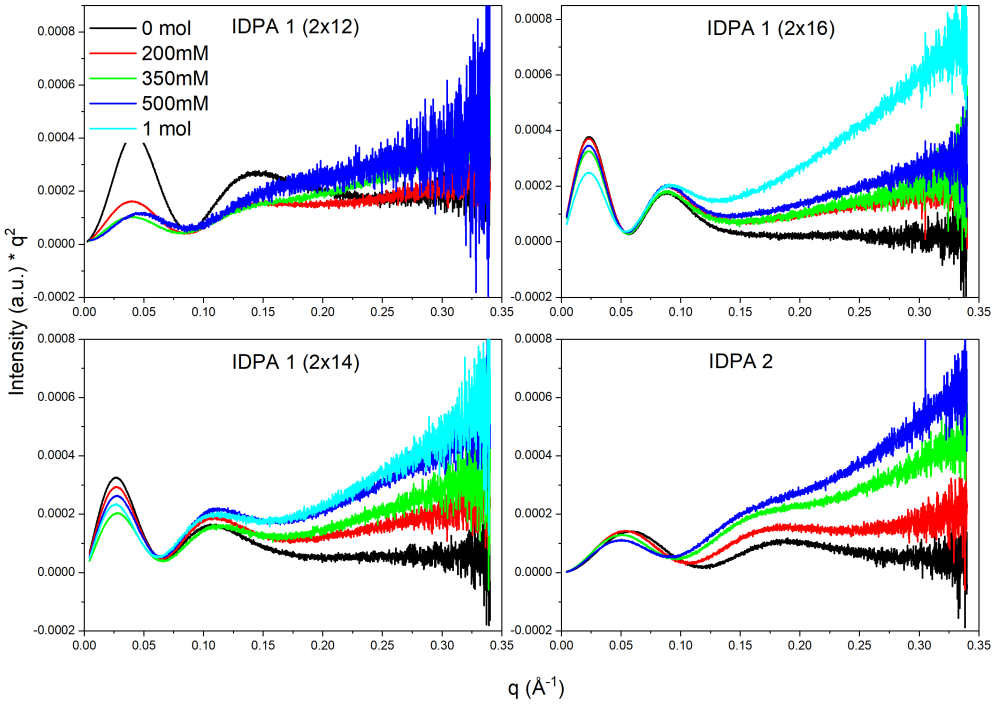

Figure 3.24: **Kratky Plots for IDPAs with different salt concentration-** Scattering in high angles become more pronounced with increasing salt. Higher chain length strengthens the trend. For low q, polydispersity between plots becomes more pronounced with increasing chain lengths.

screening, which enables intra-molecular stretching. Therefore, salt can change the plasticity and conformation of peptide headgroups.

3.3.8 Enzymatically induced phase transition

Our ultimate goal was to use the IDPAs we studied in biological applications. Our molecules can interact with enzymes; thus, we designed another IDPA (IDPA4 2×12) cleaved upon incubation with an enzyme to drastically change the IDPA self-assembly from the cleaved to uncleaved. We knew what a significant impact charge makes from previous experiments, so we decided to design the whole peptide to have all charged amino acids behind the cleavage side. Thus, upon cleavage, we remain with just neutral amino acids with IDPA4Δ 2×12. As expected, the disorder analysis show significant differences in the two sequences: neutral charged IDP4Δ is just on the disordered

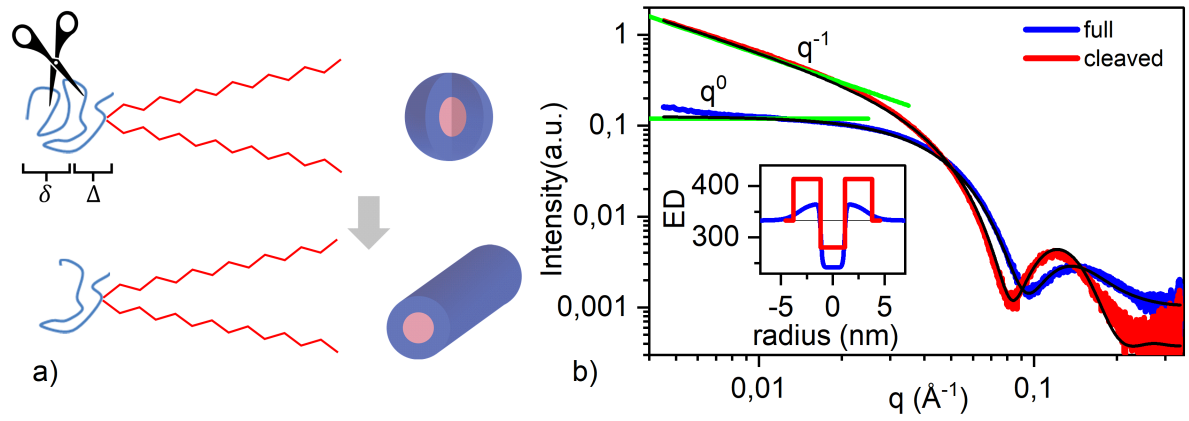

Figure 3.25: **SAXS data for cleavable IDPA.** a) Cartoon showing self-assembly of spherical and worm-like micelles for IDPA4 and IDPA4Δ 2×12. b) SAXS data and fit for the IDPAs (blue IDPA4 2×12, red IDPA4Δ 2×12) at physiological *p*H (*p*H 7). Inset shows electron density profiles. Green lines show small angle region fits used for initial structural determination.

threshold, and the whole IDP4 is disordered for all pHs.

First, we evaluated the self assembly at physiological *p*H using SAXS: full IDPA4 2×12 forms spherical micelles indicated through the flat slope in the low angles ($I(q \to 0) \sim q^0$), while the cleaved IDP4Δ is forming wormlike micelles ($I(q \to 0) \sim q^{-1}$) ((Fig 3.25a). [110]. To determine the exact size of the micelles, we fitted the data using a spherical core-shell model and a cylindrical core-shell model. Cleaving the peptide seems to smear out the peptide layer of the sphere toward higher radii with lower electron densities. At the same time, the hydrocarbon chains stay rather constant (Fig 3.25b). Here the different phases for cleaved and total peptides show strong potential to be used in drug nanocarriers. Phase transition can be used to target cargo release upon enzymatic cleavage [89].

After we evaluated the self-assembly at physiological pH, we looked into the entire *p*H range. IDPA4 2×12, with the chargeable amino acids, undergoes a phase transition while IDPA4Δ 2×12 stays in the cylindrical state. We assume to have polymer vesicles for IDPA4 2×12 at *p*H 5 in agreement with Takahashi et al. [153] (Fig. 3.26).

After we found that *p*H triggers phase transition for IDPA4 and not for IDPA4Δ, we wanted to evaluate how the *p*H influences just the peptide. Thus, just the IDP, without the tail, was measured at various pHs, and the R_g was extracted using Guinier analysis. For both IDPs the R_gs seem to be

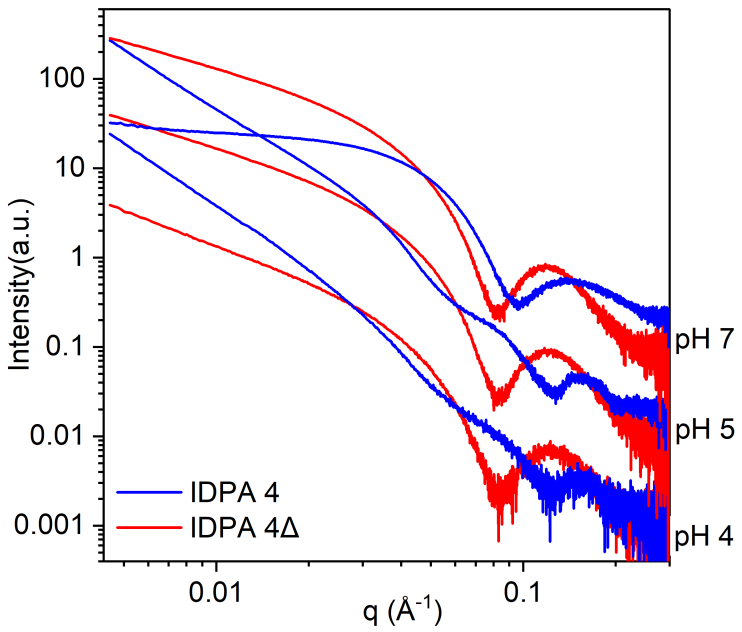

Figure 3.26: **SAXS signal for IDPA4 and IDPA4Δ 2×12.** Cleaved IDPA4Δ 2×12 remains at cylindrical form factor while IDPA4 undergoes phase transition. At physiological *p*H (*p*H 7) IDPA4 2×12 forms micelles. SAXS pattern for IDPA4 2×12 at *p*H 5 points towards the formation of polymer vesicles upon stretching of spherical micelles as shown by Takahashi et al. [153].

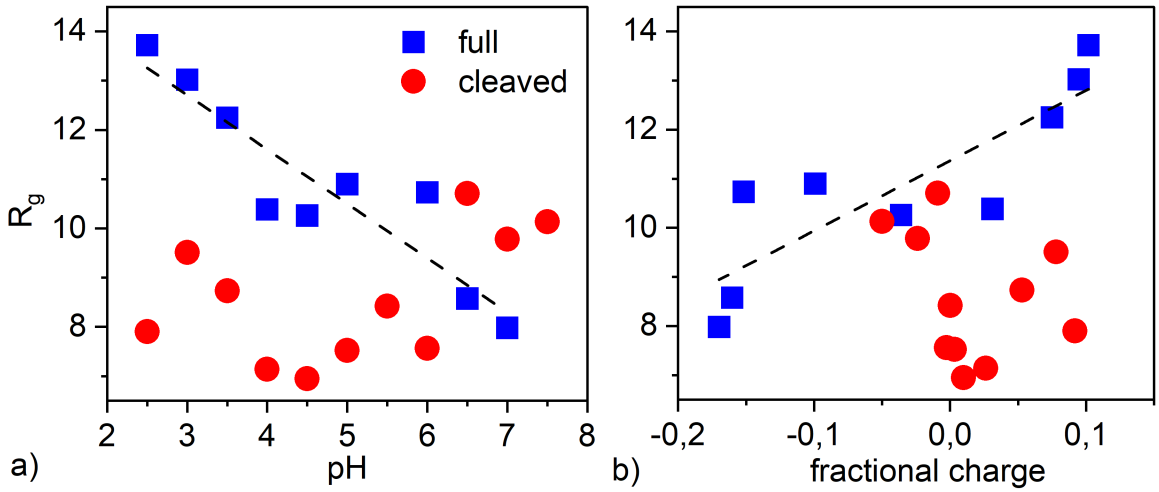

Figure 3.27: **Peptides' scaling.** a) R_g versus *p*H b) R_g versus fractional net charge. Line is a guide to the eye for tendency of IDP4.

rather constant (IDP4=$\sim$ 9 and IDP4Δ=$\sim$ 11) but for IDP4 there is a slight decrease for increasing pH (Fig. 3.27).

The ability of our IDPAs to self-assemble in various mesophases upon cleavage is of great interest for biomedical applications: our molecules need an enzymatic trigger to change their complete conformation. Additionally, the full IDPA4 is *p*H-responsive, as the IDPA contains protonable amino acids, whereas *p*H does not affect the cleaved peptide. This is similar to the IDPAs presented before and demonstrates the remarkably controllable, monodisperse nano-structures. Thus, with IDPA4 and IDPA4Δ, we can design both pH-dependent and independent structures, respectively, upon cleavage. We can combine enzymatic cleavage with *p*H-dependent phase transition in a single amphiphilic molecule.

3.4 3D printed SAXS chamber for controlled in-situ dialysis and optical characterization

In the previous chapter, I demonstrated how IDPAs can self-assemble *p*H-dependent in an exact and monodisperse way. Our previous experiments required a fresh sample for each *p*H experiment. On the one hand, this adds the unavoidable variable of slightly different samples and includes fluctuations from background to sample.

To overcome this difficulties, we designed a 3D-printed chamber that allows buffer exchange via in-situ SAXS dialysis[3]. Additionally, the chambers allow in-situ optical transmission spectroscopy. The chamber consists of cyclic olefin copolymers (COC), including COC X-ray windows providing an ultra-low SAXS background.

Up to now, the well-established window material Kapton is mostly for sample chambers, as it has a very known background signal. However, optical transparency is low, and as the chamber is often made of some plastic, Kapton needs adhesives for attachment to the chamber. In comparison to that, devices that are made out of COC can be simply 3D printed. As the chamber and windows are made out of COC, they can be annealed via heating. Another advantage is that COC is well-suited for X-ray application AND optical measurements [154]. In previous studies, [121] COC has compared Kapton windows with gold colloid measurements at two different synchrotron beamlines and showed that the background-subtracted scattering data of the COC device and the Kapton device agreed very well. So far, no dialysis chamber allowed buffer exchange for both aggregated and diluted samples and the interchange between them

The design integrates a membrane insert for in-situ dialysis of the 100 μl sample volume against a reservoir, which enables measurements of the same sample under multiple conditions using an in-house X-ray setup equipped with a 17.4 keV molybdenum source. We demonstrate the design's capabilities by measuring reversible structural changes in lipid and polymer systems as a function of salt concentration and *p*H. In the same chambers, optical light transmission spectroscopy

[3]The content of this chapter is based on our recently published article in Ref. [103]

was carried out to measure the optical turbidity of the mesophases and local *p*H values using pH-responsive dyes. Microfluidic exchange and optical spectroscopy combined with in-situ X-ray scattering enable vast applications for the study of responsive materials.

3.5 Chamber design

Designing a chamber that is easy to produce and combines all requirements was the biggest challenge in this project. It took us over 15 versions until we reached our final design. Of course, the most crucial feature of our design was the in-situ dialysis capabilities. Additionally, we wanted to create a chamber that is easy to reproduce and compatible with our in-house setup.

The biggest challenge we faced was creating a system that is, on the one hand, easy to handle and, on the other hand, properly sealed. Going from sealing rings combined with cut dialysis membranes fixed with screws, we finally designed our chamber using commercial dialysis inserts for Eppendorf cups (Slide-A-Lyzer™ MINI 0.1 mL, ThermoFisher) combined with a 3D printed chamber made out of COC. The chamber is designed "around" the dialysis inset and has a small sample chamber close to the dialysis membrane. Technical drawing of the chamber is given in Fig.3.28.

The reservoir for the buffer exchange has a total, standardized volume of 500 μl liquid and is very easy to handle. For faster buffer exchange, external syringe pumps can be applied. The insert has various pore sizes - for our experiment, we used a molecular weight cutoff of 3.5 kDa.

The chamber corpus is printed using the Ultimaker 3, which allows for the desired precision. We us 2.85 mm thick Creamelt^{TM} COC filament (Herz GmbH). On both sides we annealed transparent COC foils(50 μm thick TOPAS^{TM} 8007F-04 COC foil (Microfluidic ChipShop) with simply applying temperature (Fig. 3.29). This is possible as the chamber and the windows are made out of the same material. The profile for open-Source slicer-software Cura is openly available in `https://3dprint.nih.gov/discover/3dpx-016474`. All parameters used for printing the COC chamber are given in Table 3.2.

Printer	Ultimaker 3
Material	COC 2.85
Nozzle Size	0.4 mm
Slicing	Cura 4.6.1
Layer Height	0.15 mm
Wall Thickness	1.3 mm
Top/Bottom Thickness	1.2 mm
Horizontal Expansion	-0.05 mm
Infill Density	20 %
Printing Temperature	245 °C
Build Plate Temperature	80 °C
Printing Speed	60 mm/s
Generate Support	None
Build Plate Adhesion Type	Brim

Table 3.2: Parameter for 3D print of COC chamber

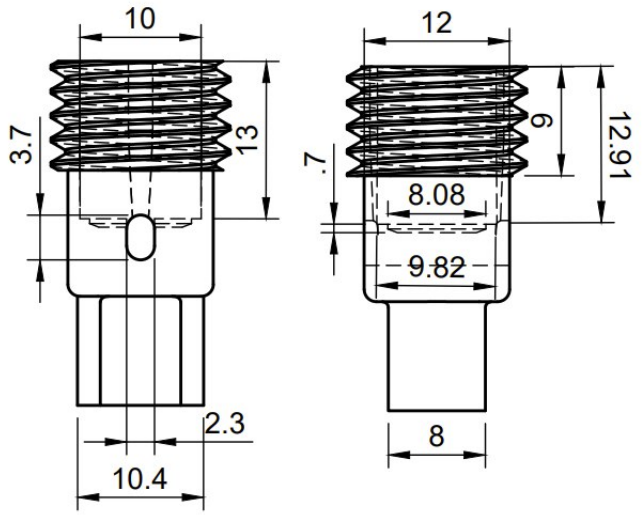

Figure 3.28: **Technical drawing of 3D printed chamber.** Front and side view of the chamber, dimensions are given in mm.

The assembly of our chamber is relatively simple- the chamber is filled (sample volume is around 100 μl) from the top, and then the dialysis inset is mounted. The whole chamber is closed with a cap to avoid evaporation. The thickness of the chamber is optimized for our in-house 17.4 keV molybdenum source.

Kapton is a well-known material for X-ray experiments due to its low and well-defined background. Even though Kapton is widely established when used as a sample chamber, there is a significant disadvantage: Kapton foil needs to be well glued to the sample chamber (PDMS, steel, COC, etc.). Self-adhesive "Kapton-tape" results in unintentional background scattering, and laser-ablated Kapton films are rather complicated and expensive to fabricate.

We benchmarked the COC with the Kapton windows by a signal-to-noise ratio measurement. We used unilamellar vesicles of SOPC at a sample concentration of 30mg/ml as a sample system. (Fig. 3.30). All bilayer parameters are obtained from model fits of the background-corrected total scattering intensity $I(q)$ to an electron density profile $\Delta\rho(z)$ composed of three Gaussians:

$$\Delta\rho(z) = \Delta\rho_H \exp\left[-\frac{(z-z_H)^2}{2\sigma_H^2}\right] + \Delta\rho_{CH} \exp\left[-\frac{z^2}{2\sigma_{CH}^2}\right] + \Delta\rho_H \exp\left[-\frac{(z+z_H)^2}{2\sigma_H^2}\right] \tag{3.1}$$

Here, $\Delta\rho_H$ is the scattering length contrast of the lipid head groups compared to water, i.e. $\Delta\rho(z) = \Delta\rho_H - \Delta\rho_w$. z_H is the spatial peak offset of the head centers concerning the center of the bilayer, and σ_H is the corresponding variance of the Gaussian functions. $\Delta\rho_{CH}$ is the scattering length contrast of the lipid chains, and σ_{CH} is the variance of the Gaussian function describing the chain region. Model fitting was achieved by running the software-internal Levenberg-Marquardt algorithm using the software package SasView (http://www.sasview.org/), fitting parameters are presented in table 3.3.

When both signals, Kapton and COC window, of the SOPC samples are compared, we found that the scattering signal of both window material is in agreement; just when measuring the pure chamber, we find that Kapton windows have a slightly stronger background signal than COC. The difference is evident in the q-regimes where Kapton is known to exhibit scattering, i.e., a broad peak

Data	z_H [Å]	$\rho_{C\|H}[a.u.]$	σ_{CH}[Å]	$\Delta\rho_H[a.u.]$	σ_H[Å]
COC	21.1	−0.002	8.6	0.004	4.3
Kapton	20.9	−0.003	9.6	0.005	4.5

Table 3.3: Parameters obtained from least-squares fitting of SAXS data of 100 nm extruded SOPS vesicles to asymmetrical flat bilayer model.

around $q = 0.09$ Å^{-1} as well as in the WAXS region with scattering at $q = 0.4$ Å^{-1} depending on the type of Kapton.

Buffer exchange kinetics

During dialysis, solvents (e.g., salt molecules) smaller than the membrane's pore size are diffuse due to a concentration gradient. The time scale for the diffusion is in the frame of a few hours and thus appropiate for the usual time scales of in-house experiments. To follow the dialysis and quantify the exact time scales of buffer exchange, we used the optical transparency of COC. As a pH-responsive indicator we used a ratio 1:2 of chlorophenol Red and Bromothymol Blue that changes its color from pink to blue in the *p*H range of 5 to 8. We made a calibration curve by measuring the transmission curve for each *p*H value with the dye (Fig. 3.31a). Then we measured the *p*H exchange using our dialysis chamber (Fig. 3.31b) and got a diffusion time of $t_{1/2} = 1$ h. Diffusion time scales can also be calculated via:

$$t = \frac{< x >^2}{2D}, \tag{3.2}$$

where x is the vertical diffusion path along the chamber ($x \approx 3mm$) and D the typical diffusion coefficient for buffer salts ($D \approx 10^{-5}\frac{cm^2}{s}$). The experimental result is in agreement with the calculated diffusion times ($t = 1.25h$).

Next we tested our chamber on two systems for SAXS. For that, we used our IDPA system (IDPA1, 2×12). We used the phase transition from spheres to cylinders shown in Fig. 3.17. Data was collected using an in-house Molybdenum X-ray SAXS source and a 2M Pilatus detector. One-

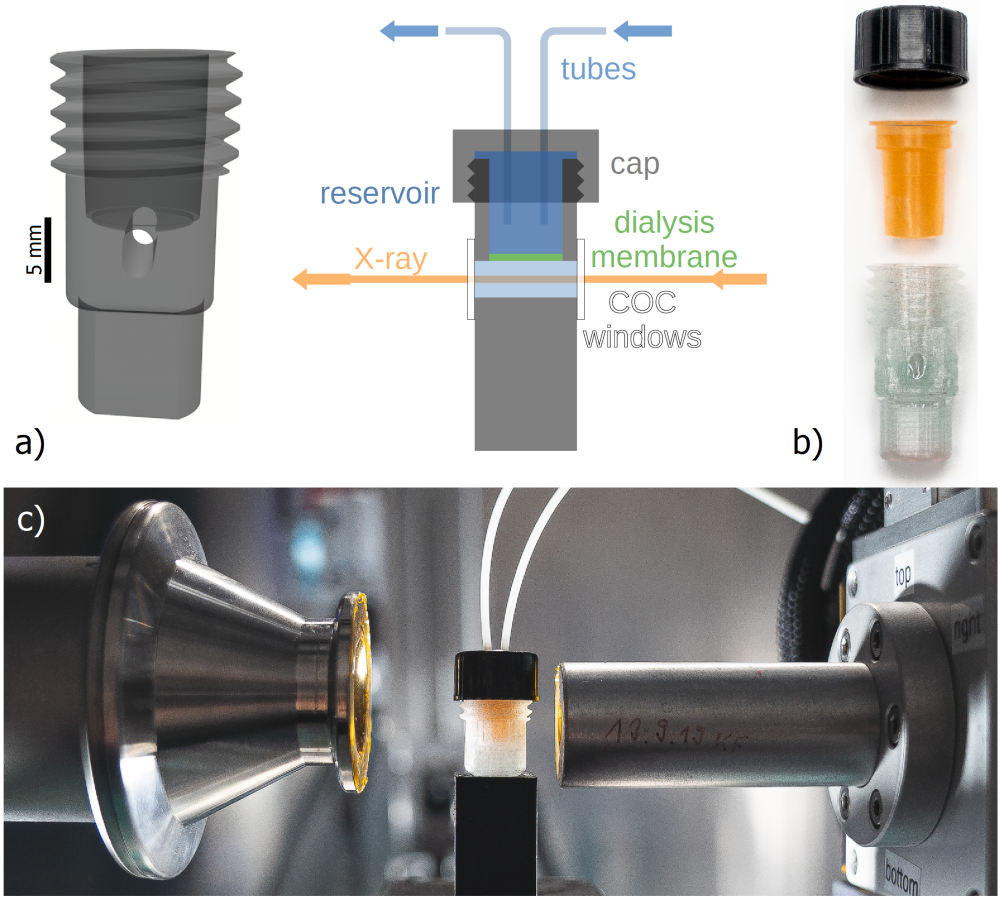

Figure 3.29: **Chamber design principle and implementation.** (a) Schematic drawing of the COC chamber. (b) Sample corpus is 3D printed out of COC to enclose the colored dialysis tube. Two COC X-ray windows allow for measurement of both condensed and and diluted phases. (c) Sample setup for in-situ measurements and dialysis using syringe pump systems.

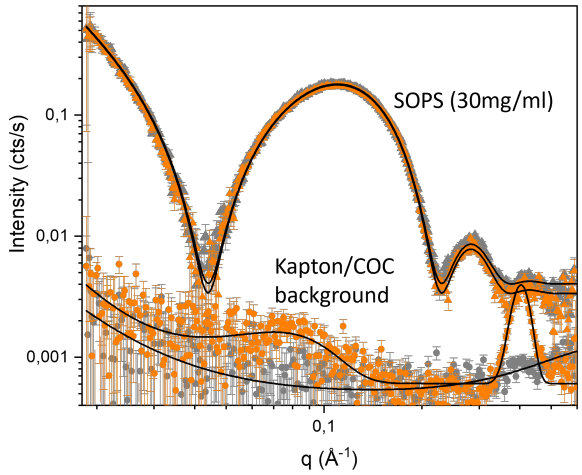

Figure 3.30: **In-house measurements with Kapton and COC windows.** Triangles: SAXS signal with errorbars (orange/grey: Kapton/COC windows) of SOPS LUVs with a diameter of 100 nm (30 mg/ml). Solid lines correspond to the best fit for flat symmetrical bilayers. Circles: SAXS signal with errorbars of the empty dialysis chamber with 50 μm thick Kapton (orange) and 100 μm thick COC windows (grey). Solid lines correspond to the best fit for a power law with one and two Gaussians. The samples were measured with an exposure time of one minute per frame and measured for 6 hours in total.

dimensional scattering curves were obtained by radial integration after normalization by the integrated intensity of the direct beam. Indeed, we were able to monitor this transition from cylindrical to spherical micelles and vice versa (pH 4.7 to pH 7.5) in our in-house apparatus. As we showed before, the diffusion time scales are in the range of hours and thus are more significant than the time resolution of the in-house SAXS device, and there is no need for a high-resolution synchrotron beam. There were no more changes after 6 hours in the IDPA self-assembly in our experiments. This makes measurement cycles efficient.

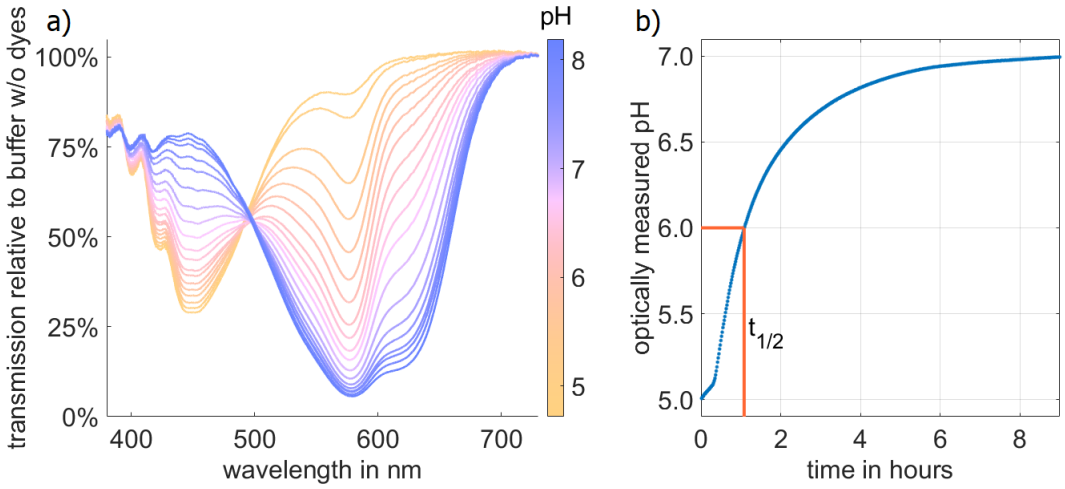

Figure 3.31: **Time scale of in-situ *p*H change.** a) pH-dependent transmission spectra of Bromothymol Blue and Chlorophynol Red mixed at a molar ratio of 2:1. b) Optical measurements of the *p*H inside the sample chamber during dialysis results in an approximate exchange halftime of $t_{1/2} = 1$ h.

After we demonstrated usability with *p*H exchange, we validated the performance of the 3D-printed dialysis chamber by measuring the response of a soft matter detergent system with known structural dependence on salt concentration. The chamber can be used for any buffer exchange where the diffusion molecules have a lower MW than the cutoff of the dialysis membrane. When using salt, experimenters can monitor and control the electrostatic interactions in biological SAXS experiments. Our chamber allows us to do these experiments with a single sample. We demonstrated this with L–phosphatidylcholine (Soy PC) doped with 5 wt% of 1,2-Dioleoyl-3-trimethylammoniumpropan (DOTAP) in a dialysis from 20 mM NaCl to 320 mM NaCl. The salt screens the charges, and the intermembrane distances shrink (300 mM:
6.0 nm, 20 mM: 5.7 nm). The dialysis is also reversible, as shown in Fig. 3.24.

The chamber can also be used for absorbance measurement in addition to SAXS experiments due to its high optical transparency. We screened the transition from micellar, monodisperse, non-turbid rods at intermediate *p*H into hexagonal packed rods at the isoelectric point (*p*H 4) shown in Fig. 3.15. Indeed we could show the transition as shown in Fig. 3.34.

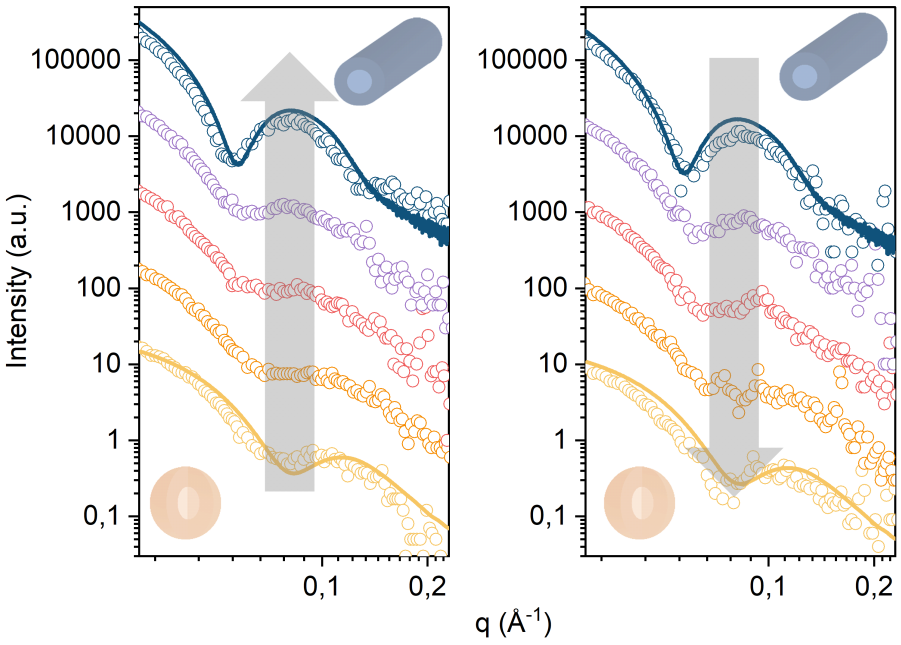

Figure 3.32: **pH-dependent phase transition in an amphiphilic peptide mesophase.** Left: Time-resolved in-house SAXS measurement (background corrected) of in-situ dialysis with 3D printed dialysis chamber from *p*H 7.5 to *p*H 4.7 of IDPAs shows a transition from micellar rods to spherical micelles in less than 6 hours. Scattering curves are snapshots at 0, 140, 160, 180, and 220 min with 20 min exposure time; Solid lines are convoluted reference scattering curves from high-resolution SAXS beamlines (Data was taken with an automated sample robot at DESY light source, Hamburg, Germany). Right: pH-dialysis back from *p*H 4.7 to *p*H 7.5 shows the reversibility of the transition in the dialysis chamber. Scattering curves are snapshots at 0, 260, 240, 340, and 520 min with a 20 min exposure time.

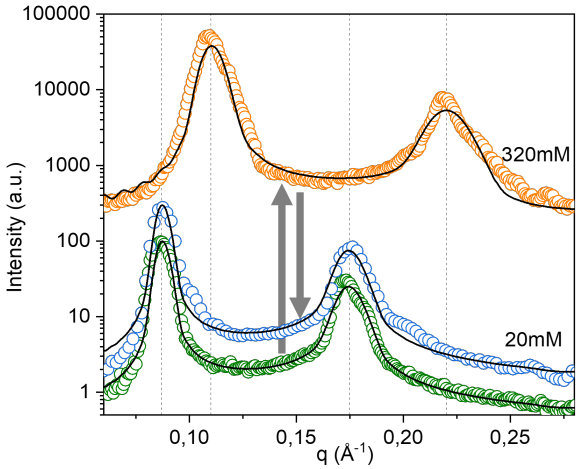

Figure 3.33: **Reversible exchange of ionic buffer conditions.** In-house SAXS SAXS signal of a charged lamellar phase (Soy PC doped with 5 wt% DOTAP) exhibits the shrinking and subsequent swelling of the intermembrane distance in response to increasing and decreasing salt concentrations. Black lines indicate fits of the data using the modified Caillé theory (MCT) combined with a Gaussian electron density representation, as proposed in [155]. The Sample was equilibrated for seven days.

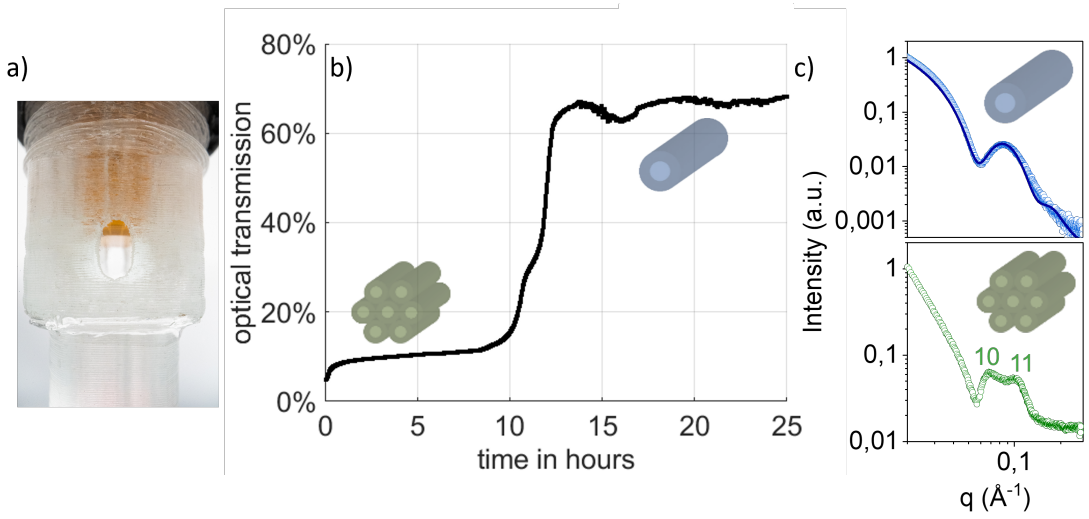

Figure 3.34: **In-situ optical turbidity measurements.** a) PhotograpH of the X-ray chamber showing the optical transparent X-ray window and the dialysis insert (orange). b) Optical turbidity across the X-ray chamber showing the structural transition from a condensed hexagonal to a dispersed cylindrical micelle phase. c) In-house SAXS signal of hexagonal-packed (green) and monodispersed micellar rods (blue) in solution min Data was taken with 20 min exposure time each. The solid line corresponds to spherical-core shell form factor (blue), Miller Indices show first, the second peak for hexagonal phase (repeat distance: 11.2nm)

Chapter 4

Conclusion and future work

~~After three years of living in two cultures, a worldwide pandemic, and hours of experiments in Munich, Tel Aviv, and almost all synchrotrons in Europe, I understood one thing - science answers questions. Science is essential. Science is saving lives. Furthermore- there are many more questions to be answered. I had the chance to answer some questions and hope that someday, another person can answer some more in my line of research presented here.~~ In my research, I wanted to find out how we can analyze the interactions of IDPAs down to the level of single amino acid. I performed experiments on the self-assembly of IDPAs to show that this system of amphiphilic molecules is an excellent platform for studying IDPs. In addition, we designed a 3D-printed chamber for in situ dialysis during SAXS experiments to expand the experimental possibilities for my IDPA system and many other pH-reactive nanomaterials.

We studied the self-assembly of five different sequences with different hydrocarbon chains. We found that the head group plays an essential role in triggering self-assembly. Environmental conditions such as salt and *p*H can trigger phase changes within a sequence. We can extend transitions and make small changes by modifying IDPAs through their hydrocarbon chains. We also found that permutations in the amino acid sequence lead to average conformations. So, not only the choice of amino acids but, more importantly, the order within the sequence plays an essential role. This is a great start to using intrinsically IDPAs to study the mutual interactions of IDPs. With

the knowledge gained in this thesis, we can design more sequences and study how they interact sequence-dependent in various mesophases. We used a sequence inspired by a neurofilament low protein, but as we already showed, functional sequences, like the cleavable sequence part, can be incorporated. Thus, with this platform, we might understand what role IDPs play in biological signaling processes, as in the Toc159 chloroplast, the cytoskeleton, or in diseases like Alzheimer's or Parkinson's. As our system is sensitive down to a single amino acid, even small changes in that system can be studied and analyzed.

Our IDPA system can be functionalized by enzymatic cleavage. IDPAs can be used as surface components of nanocarriers and then potentially respond to enzymatic triggers. This opens great opportunities for our system to be used in biomedical applications. In lipid nanoparticles, polyethylene glycol (PEG) is often used to stabilize the nanoparticles - IDPAs could replace these molecules. Since our IDPAs can respond to enzymatic triggers AND pH, they can be functionalized in two ways - release of charge upon a trigger and a *p*H change (for example, when they migrate through different cell compartments). In future work, this can be tested via cellular uptake measurements. An environmental condition that I have not targeted yet is temperature. All of my experiments were done at room temperature. This opens an entirely new variable that will give insights into entropy and energy in the system.

A major drawback of our and any pH-dependent experiments or an experiment where a sample is measured at different buffer conditions is that a new sample is needed for each condition. This is time-consuming and costly and leads to variations in the sample and background signals.

We have developed and characterized a 3D printed SAXS dialysis chamber made of COC to solve this problem. 3D printing allows the fabrication of many samples and is reliable and straightforward. The chamber can be connected to external syringe pumps allowing buffer exchange within a few hours.

We have demonstrated that this chamber is suitable for in-house SAXS measurements with various test systems. The half-life of buffer exchange has been determined using pH-sensitive dyes and is in a few hours, making it perfect for in-house setups.

We tested our COC chamber with the IDPAs and were able to show that our chamber does indeed perform the desired function - exchanging buffer from a low to a high *p*H and vice versa. In future work, it will be beneficial to study in situ dialysis in more detail to understand all phase transitions and, for example, to experimentally prove our hypothesis of the smooth transition region between spherical and worm-shaped micelles. Moreover, it is now possible to use different salt concentrations and study the electrostatic repulsion between micelles in a very controlled manner - in future experiments, the intermicellar interactions between individual IDPAs can be monitored interlamellar distances can be directly related to the electrostatic interactions.

The design of the chamber can not just be used for different samples but also be adapted for various experimental setups. For example, our chamber is also suitable for optical spectroscopy. This opens up further experiments with different samples. Optically responsive samples can be triggered in situ, and the phase change can be measured in the chamber. For the IDPA system, this also opens up the possibility of using enzymatic triggers and optical triggers that can induce phase transitions.

Chapter 5

Acknowledgments

After three years of living in two cultures, a worldwide pandemic, and hours of experiments in Munich, Tel Aviv, and almost all synchrotrons in Europe, I understood one thing - science answers questions. Science is essential. Science is saving lives. Furthermore- there are many more questions to be answered. I had the chance to answer some questions and hope that someday, another person can answer some more in my line of research presented here.

I am incredibly thankful for the opportunity to do and finish my Ph.D. at LMU and TAU. This would not have been possible without the support of my two supervisors, Joachim and Roy, and of both universities. At this point, I would also thank the DAAD and the LMU-TAU initiative for research exchange to support me financially during my Ph.D.

Roy, you always encouraged us not to stop experimenting until we find the tweek, until we find the reason that results are weird, until we can explain things and use this knowledge to discover new things. But most importantly, you are a great supporter. At all conferences, I went you always introduced me to everybody, and you gave me so many incredible options within the nano center that I will never forget.

I also want to thank my german supervisor Joachim, who supported me in all manners when I tried to go to a news conference, start a new project or adopt one more bachelor's student. Joachim also taught me a lot about paper writing and how I should think about science. I learned a lot!

When I started with my master thesis, I was the kid with great, experienced colleagues that helped me a lot, from understanding Israeli politics to learning all the spec commands. Guy and Ram, you were great older brothers, and I enjoyed our time in the student room and our travels to the synchrotrons. Both of you are great inspirations when it comes to science and in life.

I also want to thank the Beck group's second generation, especially Hila and Gil. Even though we did not meet in person during the pandemic, I always felt part of the group. A special thanks go to Hila and Gil, who supported me a lot in the IDPA project, and Sagi, who helped me during the synchrotron run during the pandemic.

But also, my german group and the entire Rädler chair were great company. A special thanks to two generations of the Unicorn Office, who always kept my mood up and never let me leave without a smile on my face. Thanks to our bachelor students, Luis, David, Martin, Miriam, Achim, and Denise, who helped a lot during COVID with our COC chamber project. And of course, Julian, who was a great colleague in that project, always reminded me a bit of an impulsive and creative mind on how structured research works. Special thanks also to Gerlinde- without you, we would be a mess. Thanks for reminding us how to clean lab work works! Also, big thanks to Bert, Kilian, and Tina, who always helped me when I got lost in SAXS questions.

Big thanks go to all my physics friends! Without you life had been just half of the fun. Sophia, Adina, Sebastian, and Samuel - thanks for everything, especially for the pasta machine. Big, big thank you to the best study friends one can imagine - Lucas, Kevin, Sandro, Bene and Jana; you made my bachelor's and master's bearable and sometimes even enjoyable. And of course, thanks to all of the other non-physics friends and sports mates who always gave me the compensation I needed. Many thanks also to my boyfriend, Nik, who supported me during that last period of my Ph.D. I am so happy that you came with me to Tel Aviv for my final presentation, and I am finally able to show you the city that became my second home during my Ph.D.

Last but most importantly, thanks to my family. For your endless support during my time in Germany and Tel Aviv, for all the times you came and picked me up when I lost my keys, and for all the feedback and encouragement you gave me. Viki, Mama, and Papa - you are the very best!

Bibliography

[1] Neil A Campbell, Jane B Reece, Lisa A Urry, Michael L Cain, Steven A Wasserman, Peter V Minorsky, and Robert Jackson. *Campbell biologie*. Pearson, 2016.

[2] Kaj Ulrik Linderstrøm-Lang. *Lane medical lectures: proteins and enzymes*, volume 6. Stanford University Press, 1952.

[3] Ranjan V Mannige, Joyjit Kundu, and Stephen Whitelam. The ramachandran number: an order parameter for protein geometry. *PloS one*, 11(8):e0160023, 2016.

[4] . Stereochemistry of polypeptide chain configurations. *J. mol. Biol*, 7:95–99, 1963.

[5] M Michael Gromiha. *Protein bioinformatics: from sequence to function*. academic press, 2010.

[6] John E McMurry. *Organic chemistry with biological applications*. Cengage Learning, 2014.

[7] Mauro Bringas, Ariel A Petruk, Darío A Estrin, Luciana Capece, and Marcelo A Martí. Tertiary and quaternary structural basis of oxygen affinity in human hemoglobin as revealed by multiscale simulations. *Scientific reports*, 7(1):1–10, 2017.

[8] Jeung-Hoi Ha and Stewart N Loh. Protein conformational switches: from nature to design. *Chemistry–A European Journal*, 18(26):7984–7999, 2012.

[9] Tamara Ehm, Hila Shinar, Sagi Meir, Amandeep Sekhon, Vaishali Sethi, Ian L Morgan, Gil Rahamim, Omar A Saleh, and Roy Beck. Intrinsically disordered proteins at the nano-scale. *Nano Futures*, 2021.

[10] Vladimir N Uversky. The mysterious unfoldome: structureless, underappreciated, yet vital part of any given proteome. *BioMed Research International*, 2010, 2009.

[11] Bo He, Kejun Wang, Yunlong Liu, Bin Xue, Vladimir N Uversky, and A Keith Dunker. Predicting intrinsic disorder in proteins: an overview. *Cell research*, 19(8):929–949, 2009.

[12] Vladimir N Uversky. Intrinsically disordered proteins in overcrowded milieu: Membrane-less organelles, phase separation, and intrinsic disorder. *Current opinion in structural biology*, 44:18–30, 2017.

[13] Peter E Wright and H Jane Dyson. Intrinsically unstructured proteins: re-assessing the protein structure-function paradigm. *Journal of molecular biology*, 293(2):321–331, 1999.

[14] Ming-Tzo Wei, Shana Elbaum-Garfinkle, Alex S Holehouse, Carlos Chih-Hsiung Chen, Marina Feric, Craig B Arnold, Rodney D Priestley, Rohit V Pappu, and Clifford P Brangwynne. Phase behaviour of disordered proteins underlying low density and high permeability of liquid organelles. *Nature Chemistry*, 9(11):1118, 2017.

[15] H Jane Dyson and Peter E Wright. Intrinsically unstructured proteins and their functions. *Nature reviews Molecular cell biology*, 6(3):197–208, 2005.

[16] Yi Xue, Tairan Yuwen, Fangqiang Zhu, and Nikolai R Skrynnikov. Role of electrostatic interactions in binding of peptides and intrinsically disordered proteins to their folded targets. 1. nmr and md characterization of the complex between the c-crk n-sh3 domain and the peptide sos. *Biochemistry*, 53(41):6473–6495, 2014.

[17] Xingcheng Lin, Prakash Kulkarni, Federico Bocci, Nicholas P Schafer, Susmita Roy, Min-Yeh Tsai, Yanan He, Yihong Chen, Krithika Rajagopalan, Steven M Mooney, et al. Structural and dynamical order of a disordered protein: molecular insights into conformational switching of page4 at the systems level. *Biomolecules*, 9(2):77, 2019.

[18] Johnny Habchi, Peter Tompa, Sonia Longhi, and Vladimir N Uversky. Introducing protein intrinsic disorder. *Chemical reviews*, 114(13):6561–6588, 2014.

[19] Vladimir N Uversky. Intrinsically disordered proteins from a to z. *The international journal of biochemistry & cell biology*, 43(8):1090–1103, 2011.

[20] Diana Ekman, Sara Light, Åsa K Björklund, and Arne Elofsson. What properties characterize the hub proteins of the protein-protein interaction network of saccharomyces cerevisiae? *Genome biology*, 7(6):1–13, 2006.

[21] Francois-Xavier Theillet, Lajos Kalmar, Peter Tompa, Kyou-Hoon Han, Philipp Selenko, A Keith Dunker, Gary W Daughdrill, and Vladimir N Uversky. The alphabet of intrinsic disorder: I. act like a pro: On the abundance and roles of proline residues in intrinsically disordered proteins. *Intrinsically Disordered Proteins*, 1(1):e24360, 2013.

[22] RM Williams, Zoran Obradovic, V Mathura, W Braun, EC Garner, J Young, S Takayama, Celeste J Brown, and A Keith Dunker. The protein non-folding problem: amino acid determinants of intrinsic order and disorder. In *Biocomputing 2001*, pages 89–100. World Scientific, 2000.

[23] Micha Kornreich, Ram Avinery, Eti Malka-Gibor, Adi Laser-Azogui, and Roy Beck. Order and disorder in intermediate filament proteins. *FEBS letters*, 589(19 Pt A):2464–76, sep 2015.

[24] V N Uversky and A K Dunker. Understanding protein non-folding. *Biochimica Et Biophysica Acta-Proteins and Proteomics*, 1804(6):1231–1264, 2010.

[25] Vladimir N. Uversky. Intrinsically disordered proteins from a to z. *The International Journal of Biochemistry & Cell Biology*, 43(8):1090–1103, aug 2011.

[26] Vladimir N. Uversky. Introduction to Intrinsically Disordered Proteins (IDPs). *Chemical Reviews*, 114(13):6557–6560, jul 2014.

[27] Vladimir N. Uversky. Intrinsically disordered proteins and their "mysterious" (meta)physics. *Frontiers in Physics*, 7:10, 2019.

[28] Vladimir N Uversky, Joel R Gillespie, and Anthony L Fink. Why are "natively unfolded" proteins unstructured under physiologic conditions? *Proteins: structure, function, and bioinformatics*, 41(3):415–427, 2000.

[29] Valery Ozenne, Robert Schneider, Mingxi Yao, Jie-rong Huang, Loïc Salmon, Markus Zweckstetter, Malene Ringkjøbing Jensen, and Martin Blackledge. Mapping the potential energy landscape of intrinsically disordered proteins at amino acid resolution. *Journal of the American Chemical Society*, 134(36):15138–15148, 2012.

[30] Rahul K Das, Kiersten M Ruff, and Rohit V Pappu. Relating sequence encoded information to form and function of intrinsically disordered proteins. *Current opinion in structural biology*, 32:102–112, 2015.

[31] Albert H Mao, Nicholas Lyle, and Rohit V Pappu. Describing sequence–ensemble relationships for intrinsically disordered proteins. *Biochemical Journal*, 449(2):307–318, 2013.

[32] Rahul K Das and Rohit V Pappu. Conformations of intrinsically disordered proteins are influenced by linear sequence distributions of oppositely charged residues. *Proceedings of the National Academy of Sciences*, 110(33):13392–13397, 2013.

[33] DE Koshland Jr. Application of a theory of enzyme specificity to protein synthesis. *Proceedings of the National Academy of Sciences of the United States of America*, 44(2):98, 1958.

[34] Luca Mollica, Luiza M Bessa, Xavier Hanoulle, Malene Ringkjøbing Jensen, Martin Blackledge, and Robert Schneider. Binding mechanisms of intrinsically disordered proteins: theory, simulation, and experiment. *Frontiers in molecular biosciences*, 3:52, 2016.

[35] Munehito Arai, Kenji Sugase, H Jane Dyson, and Peter E Wright. Conformational propensities of intrinsically disordered proteins influence the mechanism of binding and folding. *Proceedings of the National Academy of sciences*, 112(31):9614–9619, 2015.

[36] A Keith Dunker, J David Lawson, Celeste J Brown, Ryan M Williams, Pedro Romero, Jeong S Oh, Christopher J Oldfield, Andrew M Campen, Catherine M Ratliff, Kerry W Hipps, et al. Intrinsically disordered protein. *Journal of Molecular Graphics and Modelling*, 19(1):26–59, 2001.

[37] Yassmine Chebaro, Andrew J Ballard, Debayan Chakraborty, and David J Wales. Intrinsically disordered energy landscapes. *Scientific reports*, 5(1):1–12, 2015.

[38] Robert Konrat. Nmr contributions to structural dynamics studies of intrinsically disordered proteins. *Journal of Magnetic Resonance*, 241:74–85, 2014.

[39] Gottfried Otting. Protein nmr using paramagnetic ions. *Annual review of biophysics*, 39:387–405, 2010.

[40] Gerald Platzer, Andreas Schedlbauer, Angela Chemelli, Przemyslaw Ozdowy, Nicolas Coudevylle, Renate Auer, Georg Kontaxis, Markus Hartl, Andrew J Miles, Bonnie A Wallace, et al. The metastasis-associated extracellular matrix protein osteopontin forms transient structure in ligand interaction sites. *Biochemistry*, 50(27):6113–6124, 2011.

[41] François Ferron, Sonia Longhi, Bruno Canard, and David Karlin. A practical overview of protein disorder prediction methods. *Proteins: Structure, Function, and Bioinformatics*, 65(1):1–14, 2006.

[42] Bálint Mészáros, Gábor Erdős, and Zsuzsanna Dosztányi. Iupred2a: context-dependent prediction of protein disorder as a function of redox state and protein binding. *Nucleic acids research*, 46(W1):W329–W337, 2018.

[43] Indrani Chakraborty, Gil Rahamim, Ram Avinery, Yael Roichman, and Roy Beck. Nanoparticle mobility over a surface as a probe for weak transient disordered peptide–peptide interactions. *Nano letters*, 19(9):6524–6534, 2019.

[44] Yongdae Shin and Clifford P Brangwynne. Liquid phase condensation in cell physiology and disease. *Science*, 357(6357), 2017.

[45] Sushmita Basu and Ranjit Prasad Bahadur. A structural perspective of rna recognition by intrinsically disordered proteins. *Cellular and Molecular Life Sciences*, 73(21):4075–4084, 2016.

[46] Peter E Wright and H Jane Dyson. Intrinsically disordered proteins in cellular signalling and regulation. *Nature Reviews Molecular Cell Biology*, 16(1):18–29, 2015.

[47] Hagai Marmor Kollet, Aviad Siany, Nancy Kedersha, Naama Knafo, Natalia Rivkin, Yehuda M Danino, Tsviya Olender, Nir Cohen, Thomas Moens, Adrian Higginbottom, et al. Spatio-temporal proteomic analysis of stress granule disassembly using apex reveals regulation by sumoylation and links to als pathogenesis. *Molecular Cell*, 2020.

[48] A Keith Dunker, Marc S Cortese, Pedro Romero, Lilia M Iakoucheva, and Vladimir N Uversky. Flexible nets: the roles of intrinsic disorder in protein interaction networks. *The FEBS journal*, 272(20):5129–5148, 2005.

[49] Stefano Gianni, Jakob Dogan, and Per Jemth. Coupled binding and folding of intrinsically disordered proteins: what can we learn from kinetics? *Current Ppinion in Structural Biology*, 36:18–24, 2016.

[50] Stive Pregent, Amir Lichtenstein, Ram Avinery, Adi Laser-Azogui, Fernando Patolsky, and Roy Beck. Probing the interactions of intrinsically disordered proteins using nanoparticle tags. *Nano letters*, 15(5):3080–7, may 2015.

[51] Adi Laser-Azogui, Micha Kornreich, Eti Malka-Gibor, and Roy Beck. Neurofilament assembly and function during neuronal development. *Current Opinion in Cell Biology*, 32:92–101, feb 2015.

[52] Cyrus R Safinya, Joanna Deek, Roy Beck, Jayna B Jones, Cecilia Leal, Kai K Ewert, and Youli Li. Liquid crystal assemblies in biologically inspired systems. *Liquid crystals*, 40(12):1748–1758, jan 2013.

[53] Mainak Guharoy, Beata Szabo, Sara Contreras Martos, Simone Kosol, and Peter Tompa. Intrinsic Structural Disorder in Cytoskeletal Proteins. *Cytoskeleton*, 70(10):550–571, oct 2013.

[54] Peter J. Chung, Chaeyeon Song, Joanna Deek, Herbert P. Miller, Youli Li, Myung Chul Choi, Leslie Wilson, Stuart C. Feinstein, and Cyrus R. Safinya. Tau mediates microtubule bundle architectures mimicking fascicles of microtubules found in the axon initial segment. *Nature Communications*, 7(1):12278, dec 2016.

[55] Micha Kornreich, Eti Malka-Gibor, Ben Zuker, Adi Laser-Azogui, and Roy Beck. Neurofilaments Function as Shock Absorbers: Compression Response Arising from Disordered Proteins. *Physical Review Letters*, 117(14):148101, sep 2016.

[56] Lynne Chang and Robert D. Goldman. Intermediate filaments mediate cytoskeletal crosstalk. *Nature Reviews Molecular Cell Biology*, 5(8):601–613, aug 2004.

[57] Eti Malka-Gibor, Micha Kornreich, Adi Laser-Azogui, Ofer Doron, Irena Zingerman-Koladko, Jan Harapin, Ohad Medalia, and Roy Beck. Phosphorylation-Induced Mechanical Regulation of Intrinsically Disordered Neurofilament Proteins. *Biophysical Journal*, 112(5):892–900, mar 2017.

[58] Roy Beck, Joanna Deek, Jayna B. Jones, and Cyrus R. Safinya. Gel-expanded to gel-condensed transition in neurofilament networks revealed by direct force measurements. *Nature Materials*, 9(1):40–46, jan 2010.

[59] Lynn GL Richardson, Masoud Jelokhani-Niaraki, and Matthew D Smith. The acidic domains of the toc159 chloroplast preprotein receptor family are intrinsically disordered protein domains. *BMC Biochemistry*, 10(1):1–8, 2009.

[60] Haruka Chino, Tomohisa Hatta, Tohru Natsume, and Noboru Mizushima. Intrinsically disordered protein tex264 mediates er-phagy. *Molecular Cell*, 74(5):909–921, 2019.

[61] Jianhong Zhou, Christopher J Oldfield, Wenying Yan, Bairong Shen, and A Keith Dunker. Intrinsically disordered domains: Sequence disorder function relationships. *Protein Science*, 28(9):1652–1663, 2019.

[62] Mioara Larion, Roberto Kopke Salinas, Lei Bruschweiler-Li, Brian G Miller, and Rafael Brüschweiler. Order–disorder transitions govern kinetic cooperativity and allostery of monomeric human glucokinase. *PLoS Biology*, 10(12):e1001452, 2012.

[63] C. P. Brangwynne, C. R. Eckmann, D. S. Courson, A. Rybarska, C. Hoege, J. Gharakhani, F. Julicher, and A. A. Hyman. Germline P Granules Are Liquid Droplets That Localize by Controlled Dissolution/Condensation. *Science*, 324(5935):1729–1732, jun 2009.

[64] Martín Carballo-Pacheco and Birgit Strodel. Comparison of force fields for alzheimer's a: A case study for intrinsically disordered proteins. *Protein Science*, 26(2):174–185, 2017.

[65] Orkid Coskuner-Weber and Vladimir N Uversky. Insights into the molecular mechanisms of alzheimer's and parkinson's diseases with molecular simulations: Understanding the roles of artificial and pathological missense mutations in intrinsically disordered proteins related to pathology. *International journal of molecular sciences*, 19(2):336, 2018.

[66] Carmine Ceraolo and Federico M Giorgi. Genomic variance of the 2019-ncov coronavirus. *Journal of Medical Virology*, 92(5):522–528, 2020.

[67] Jasmine Cubuk, Jhullian J. Alston, J. Jeremias Incicco, Sukrit Singh, Melissa D. Stuchell-Brereton, Michael D. Ward, Maxwell I. Zimmerman, Neha Vithani, Daniel Griffith, Jason A. Wagoner, Gregory R. Bowman, Kathleen B. Hall, Andrea Soranno, and Alex S. Holehouse. The sars-cov-2 nucleocapsid protein is dynamic, disordered, and phase separates with rna. *bioRxiv*, 2020.

[68] Gregory L Dignon, Wenwei Zheng, Young C Kim, Robert B Best, and Jeetain Mittal. Sequence determinants of protein phase behavior from a coarse-grained model. *PLoS Computational Biology*, 14(1):e1005941, 2018.

[69] Huan-Xiang Zhou, Valery Nguemaha, Konstantinos Mazarakos, and Sanbo Qin. Why do disordered and structured proteins behave differently in phase separation? *Trends in Biochemical Sciences*, 43(7):499–516, 2018.

[70] Soumen Saha, Samagya Banskota, Stefan Roberts, Nadia Kirmani, and Ashutosh Chilkoti. Engineering the architecture of elastin-like polypeptides: From unimers to hierarchical self-assembly. *Advanced therapeutics*, 3(3):1900164, 2020.

[71] Michael Dzuricky, Bradley A Rogers, Abdulla Shahid, Paul S Cremer, and Ashutosh Chilkoti. De novo engineering of intracellular condensates using artificial disordered proteins. *Nature Chemistry*, 12(9):814–825, 2020.

[72] Felipe Garcia Quiroz, Nan K Li, Stefan Roberts, Patrick Weber, Michael Dzuricky, Isaac Weitzhandler, Yaroslava G Yingling, and Ashutosh Chilkoti. Intrinsically disordered proteins access a range of hysteretic phase separation behaviors. *Science Advances*, 5(10):eaax5177, 2019.

[73] Jayesh A Kulkarni, Johnathan Layne Myhre, Sam Chen, Yuen Yi C Tam, Adrian Danescu, Joy M Richman, and Pieter R Cullis. Design of lipid nanoparticles for in vitro and in vivo delivery of plasmid dna. *Nanomedicine: Nanotechnology, Biology and Medicine*, 13(4):1377–1387, 2017.

[74] Jacob N Israelachvili, D John Mitchell, and Barry W Ninham. Theory of self-assembly of lipid bilayers and vesicles. *Biochimica et Biophysica Acta (BBA)-Biomembranes*, 470(2):185–201, 1977.

[75] Peter Berndt, Gregg B Fields, and Matthew Tirrell. Synthetic lipidation of peptides and amino acids: monolayer structure and properties. *Journal of the American Chemical Society*, 117(37):9515–9522, 1995.

[76] John B Matson, Christina J Newcomb, Ronit Bitton, and Samuel I Stupp. Nanostructure-templated control of drug release from peptide amphiphile nanofiber gels. *Soft Matter*, 8(13):3586–3595, 2012.

[77] Yani Zhao, Robinson Cortes-Huerto, Kurt Kremer, and Joseph F Rudzinski. Investigating the conformational ensembles of intrinsically disordered proteins with a simple physics-based model. *The Journal of Physical Chemistry B*, 124(20):4097–4113, 2020.

[78] Huihui Kuang, Sook Hee Ku, and Efrosini Kokkoli. The design of peptide-amphiphiles as functional ligands for liposomal anticancer drug and gene delivery. *Advanced drug delivery reviews*, 110:80–101, 2017.

[79] Honggang Cui, Matthew J Webber, and Samuel I Stupp. Self-assembly of peptide amphiphiles: From molecules to nanostructures to biomaterials. *Peptide Science: Original Research on Biomolecules*, 94(1):1–18, 2010.

[80] Krista L Niece, Jeffrey D Hartgerink, Jack JJM Donners, and Samuel I Stupp. Self-assembly combining two bioactive peptide-amphiphile molecules into nanofibers by electrostatic attraction. *Journal of the American Chemical Society*, 125(24):7146–7147, 2003.

[81] Xiubo Zhao, Fang Pan, Hai Xu, Mohammed Yaseen, Honghong Shan, Charlotte AE Hauser, Shuguang Zhang, and Jian R Lu. Molecular self-assembly and applications of designer peptide amphiphiles. *Chemical Society Reviews*, 39(9):3480–3498, 2010.

[82] Efrosini Kokkoli, Anastasia Mardilovich, Alison Wedekind, Emilie L Rexeisen, Ashish Garg, and Jennifer A Craig. Self-assembly and applications of biomimetic and bioactive peptide-amphiphiles. *Soft Matter*, 2(12):1015–1024, 2006.

[83] Yurong Zhao, Wei Yang, Cuixia Chen, Jiqian Wang, Limin Zhang, and Hai Xu. Rational design and self-assembly of short amphiphilic peptides and applications. *Current Opinion in Colloid & Interface Science*, 35:112–123, 2018.

[84] Tyson J Moyer, Hussein A Kassam, Edward SM Bahnson, Courtney E Morgan, Faifan Tantakitti, Teng L Chew, Melina R Kibbe, and Samuel I Stupp. Shape-dependent targeting of injured blood vessels by peptide amphiphile supramolecular nanostructures. *Small*, 11(23):2750–2755, 2015.

[85] H-W Jun, Virany Yuwono, Sergey E Paramonov, and Jeffrey D Hartgerink. Enzyme-mediated degradation of peptide-amphiphile nanofiber networks. *Advanced Materials*, 17(21):2612–2617, 2005.

[86] Yin-Jia Cheng, Ai-Qing Zhang, Jing-Jing Hu, Feng He, Xuan Zeng, and Xian-Zheng Zhang. Multifunctional peptide-amphiphile end-capped mesoporous silica nanoparticles for tumor targeting drug delivery. *ACS applied materials & interfaces*, 9(3):2093–2103, 2017.

[87] Aikaterini Lalatsa, Andreas G Schätzlein, Mariarosa Mazza, Thi Bich Hang Le, and Ijeoma F Uchegbu. Amphiphilic poly (l-amino acids)—new materials for drug delivery. *Journal of Controlled Release*, 161(2):523–536, 2012.

[88] Zhenhua Song, Xing Chen, Xinru You, Keqing Huang, Arvind Dhinakar, Zhipeng Gu, and Jun Wu. Self-assembly of peptide amphiphiles for drug delivery: the role of peptide primary and secondary structures. *Biomaterials science*, 5(12):2369–2380, 2017.

[89] Guy Jacoby, Merav Segal Asher, Tamara Ehm, Inbal Abutbul Ionita, Hila Shinar, Salome Azoulay-Ginsburg, Dganit Danino, Michael M Kozlov, Roey J Amir, and Roy Beck. Order from disorder with intrinsically disordered peptide amphiphiles. *arXiv preprint arXiv:2103.10131*, 2021.

[90] Joscha Breibeck and Arne Skerra. The polypeptide biophysics of proline/alanine-rich sequences (pas): Recombinant biopolymers with peg-like properties. *Biopolymers*, 109(1):e23069, 2018.

[91] Lihong Liu, Kun Guo, Jia Lu, Subbu S Venkatraman, Dan Luo, Kian Chye Ng, Eng-Ang Ling, Shabbir Moochhala, and Yi-Yan Yang. Biologically active core/shell nanoparticles

self-assembled from cholesterol-terminated peg–tat for drug delivery across the blood–brain barrier. *Biomaterials*, 29(10):1509–1517, 2008.

[92] Timothy S Burkoth, T LS Benzinger, Volker Urban, David G Lynn, Stephen C Meredith, and P Thiyagarajan. Self-assembly of a betasub 10–35-peg block copolymer fibrils. *Journal of the American Chemical Society*, 121(32), 1999.

[93] Stanislav Kler, Roi Asor, Chenglei Li, Avi Ginsburg, Daniel Harries, Ariella Oppenheim, Adam Zlotnick, and Uri Raviv. Rna encapsidation by sv40-derived nanoparticles follows a rapid two-state mechanism. *Journal of the American Chemical Society*, 134(21):8823–8830, 2012.

[94] Haydyn DT Mertens and Dmitri I Svergun. Structural characterization of proteins and complexes using small-angle x-ray solution scattering. *Journal of structural biology*, 172(1):128–141, 2010.

[95] Veronica Chappa, Yuliya Smirnova, Karlo Komorowski, Marcus Müller, and Tim Salditt. The effect of polydispersity, shape fluctuations and curvature on small unilamellar vesicle small-angle x-ray scattering curves. *Journal of Applied Crystallography*, 54(2), 2021.

[96] Martha E Brennich, Ulla Vainio, Tatjana Wedig, Susanne Bauch, Harald Herrmann, and Sarah Köster. Mutation-induced alterations of intra-filament subunit organization in vimentin filaments revealed by saxs. *Soft matter*, 15(9):1999–2008, 2019.

[97] Greg L Hura, Helen Budworth, Kevin N Dyer, Robert P Rambo, Michal Hammel, Cynthia T McMurray, and John A Tainer. Comprehensive macromolecular conformations mapped by quantitative saxs analyses. *Nature methods*, 10(6):453–454, 2013.

[98] Guy Jacoby, Keren Cohen, Kobi Barkan, Yeshayahu Talmon, Dan Peer, and Roy Beck. Metastability in lipid based particles exhibits temporally deterministic and controllable behavior. *Scientific reports*, 5:9481, 2015.

[99] M Kornreich, E Malka-Gibor, A Laser-Azogui, O Doron, H Herrmann, and R Beck. Composite bottlebrush mechanics: α-internexin fine-tunes neurofilament network properties. *Soft Matter*, 11(29):5839–5849, 2015.

[100] Cyrus R Safinya, Joanna Deek, Roy Beck, Jayna B Jones, and Youli Li. Assembly of biological nanostructures: isotropic and liquid crystalline phases of neurofilament hydrogels. *Annu. Rev. Condens. Matter Phys.*, 6(1):113–136, 2015.

[101] Micha Kornreich, Eti Malka-Gibor, Ben Zuker, Adi Laser-Azogui, and Roy Beck. Neurofilaments function as shock absorbers: compression response arising from disordered proteins. *Physical review letters*, 117(14):148101, 2016.

[102] Alexey G Kikhney and Dmitri I Svergun. A practical guide to small angle x-ray scattering (saxs) of flexible and intrinsically disordered proteins. *FEBS letters*, 589(19):2570–2577, 2015.

[103] Tamara Ehm, Julian Philipp, Martin Barkey, Martina Ober, Achim Theo Brinkop, David Simml, Miriam von Westphalen, Bert Nickel, Roy Beck, and Joachim O Rädler. 3d-printed saxs chamber for controlled in situ dialysis and optical characterization. *Journal of Synchrotron Radiation*, 29(4), 2022.

[104] Linh Nguyen, Mihir Dass, Martina F Ober, Lucas V Besteiro, Zhiming M Wang, Bert Nickel, Alexander O Govorov, Tim Liedl, and Amelie Heuer-Jungemann. Chiral assembly of gold–silver core–shell plasmonic nanorods on dna origami with strong optical activity. *ACS nano*, 14(6):7454–7461, 2020.

[105] Angelina Angelova, Borislav Angelov, Rada Mutafchieva, Vasil M Garamus, Sylviane Lesieur, Sérgio S Funari, Regine Willumeit, and Patrick Couvreur. Swelling of a sponge lipid phase via incorporation of a nonionic amphiphile: Sans and saxs studies. *Trends in colloid and interface science XXIV*, pages 1–6, 2011.

[106] Bing Hong, Jonathan Lai, Loïc Leclercq, Marion Collinet-Fressancourt, Jean-Marie Aubry, Pierre Bauduin, and Veronique Nardello-Rataj. Binary and ternary phase behaviors of short double-chain quaternary ammonium amphiphiles: surface tension, polarized optical microscopy, and saxs investigations. *The Journal of Physical Chemistry B*, 117(47):14732–14742, 2013.

[107] Kurt Stubenrauch, Christian Moitzi, Gerhard Fritz, Otto Glatter, Gregor Trimmel, and Franz Stelzer. Precise tuning of micelle, core, and shell size by the composition of amphiphilic block copolymers derived from romp investigated by dls and saxs. *Macromolecules*, 39(17):5865–5874, 2006.

[108] Anton Paar. The principles of dynamic light scattering.

[109] Stefano Da Vela and Dmitri I Svergun. Methods, development and applications of small-angle x-ray scattering to characterize biological macromolecules in solution. *Current Research in Structural Biology*, 2020.

[110] André Guinier, Gérard Fournet, and Kenneth L Yudowitch. Small-angle scattering of x-rays. 1955.

[111] John B Hayter and Jeff Penfold. An analytic structure factor for macroion solutions. *Molecular Physics*, 42(1):109–118, 1981.

[112] Michel HJ Koch, Patrice Vachette, and Dmitri I Svergun. Small-angle scattering: a view on the properties, structures and structural changes of biological macromolecules in solution. *Quarterly reviews of biophysics*, 36(2):147–227, 2003.

[113] Christopher D Putnam, Michal Hammel, Greg L Hura, and John A Tainer. X-ray solution scattering (saxs) combined with crystallography and computation: defining accurate macromolecular structures, conformations and assemblies in solution. *Quarterly reviews of biophysics*, 40(3):191–285, 2007.

[114] Benjamin Abécassis, Fabienne Testard, Olivier Spalla, and Philippe Barboux. Probing in situ the nucleation and growth of gold nanoparticles by small-angle x-ray scattering. *Nano letters*, 7(6):1723–1727, 2007.

[115] Hiroshi Kihara. Stopped-flow apparatus for x-ray scattering and xafs. *Journal of Synchrotron Radiation*, 1(1):74–77, 1994.

[116] Kurinji Krishnamoorthy, Sumit Kewalramani, Ali Ehlen, Liane M Moreau, Chad A Mirkin, Monica Olvera de la Cruz, and Michael J Bedzyk. Enzymatic degradation of dna probed by in situ x-ray scattering. *ACS nano*, 13(10):11382–11391, 2019.

[117] Clement E Blanchet, Alessandro Spilotros, Frank Schwemmer, Melissa A Graewert, Alexey Kikhney, Cy M Jeffries, Daniel Franke, Daniel Mark, Roland Zengerle, Florent Cipriani, et al. Versatile sample environments and automation for biological solution x-ray scattering experiments at the p12 beamline (petra iii, desy). *Journal of applied crystallography*, 48(2):431–443, 2015.

[118] Magda Skou, Søren Skou, Thomas G Jensen, Bente Vestergaard, and Richard E Gillilan. In situ microfluidic dialysis for biological small-angle x-ray scattering. *Journal of applied crystallography*, 47(4):1355–1366, 2014.

[119] Niels Junius, Sofia Jaho, Yoann Sallaz-Damaz, Franck Borel, Jean-Baptiste Salmon, and Monika Budayova-Spano. A microfluidic device for both on-chip dialysis protein crystallization and in situ x-ray diffraction. *Lab on a Chip*, 20(2):296–310, 2020.

[120] K Nørgaard Toft, Bente Vestergaard, Søren S Nielsen, Detlef Snakenborg, Mads G Jeppesen, Jes K Jacobsen, Lise Arleth, and Jorg P Kutter. High-throughput small angle x-ray scattering from proteins in solution using a microfluidic front-end. *Analytical Chemistry*, 80(10):3648–3654, 2008.

[121] Manuela Denz, Gerrit Brehm, Clément YJ Hémonnot, Heidi Spears, Andrew Wittmeier, Chiara Cassini, Oliva Saldanha, Eleonora Perego, Ana Diaz, Manfred Burghammer, et al.

Cyclic olefin copolymer as an x-ray compatible material for microfluidic devices. *Lab on a Chip*, 18(1):171–178, 2018.

[122] Frank Schwemmer, Clement E Blanchet, Alessandro Spilotros, Dominique Kosse, Steffen Zehnle, Haydyn DT Mertens, Melissa A Graewert, Manfred Rössle, Nils Paust, Dmitri I Svergun, et al. Labdisk for saxs: a centrifugal microfluidic sample preparation platform for small-angle x-ray scattering. *Lab on a Chip*, 16(7):1161–1170, 2016.

[123] Sarah Koester and Thomas Pfohl. X-ray studies of biological matter in microfluidic environments. *Modern physics letters B*, 26(26):1230018, 2012.

[124] Bruno FB Silva, Miguel Zepeda-Rosales, Neeraja Venkateswaran, Bretton J Fletcher, Lester G Carter, Tsutomu Matsui, Thomas M Weiss, Jun Han, Youli Li, Ulf Olsson, et al. Nematic director reorientation at solid and liquid interfaces under flow: Saxs studies in a microfluidic device. *Langmuir*, 31(14):4361–4371, 2015.

[125] Aghiad Ghazal, Josiane P Lafleur, Kell Mortensen, Jörg P Kutter, Lise Arleth, and Grethe V Jensen. Recent advances in x-ray compatible microfluidics for applications in soft materials and life sciences. *Lab on a Chip*, 16(22):4263–4295, 2016.

[126] Harm-Jan Steenhuis, Xin Fang, and Tolga Ulusemre. Global diffusion of innovation during the fourth industrial revolution: the case of additive manufacturing or 3d printing. In *Emerging Issues And Trends In Innovation And Technology Management*, pages 333–368. World Scientific, 2022.

[127] Aroa Duro-Castano, Inmaculada Conejos-Sánchez, and María J Vicent. Peptide-based polymer therapeutics. *Polymers*, 6(2):515–551, 2014.

[128] Tal Ben-Nun, Avi Ginsburg, Pablo Székely, and Uri Raviv. X+: a comprehensive computationally accelerated structure analysis tool for solution x-ray scattering from supramolecular self-assemblies. *Journal of Applied Crystallography*, 43(6):1522–1531, 2010.

[129] Kenneth Levenberg. A method for the solution of certain non-linear problems in least squares. *Quarterly of applied mathematics*, 2(2):164–168, 1944.

[130] Roger Penrose. A generalized inverse for matrices. In *Mathematical proceedings of the Cambridge philosophical society*, volume 51, pages 406–413. Cambridge University Press, 1955.

[131] Roi Asor, Christopher John Schlicksup, Zhongchao Zhao, Adam Zlotnick, and Uri Raviv. Rapidly forming early intermediate structures dictate the pathway of capsid assembly. *Journal of the American Chemical Society*, 142(17):7868–7882, 2020.

[132] HI Silman and Arthur Karlin. Effect of local ph changes caused by substrate hydrolysis on the activity of membrane-bound acetylcholinesterase. *Proceedings of the National Academy of Sciences of the United States of America*, 58(4):1664, 1967.

[133] Tamas Lazar, Elizabeth Martínez-Pérez, Federica Quaglia, András Hatos, Lucía B Chemes, Javier A Iserte, Nicolás A Méndez, Nicolás A Garrone, Tadeo E Saldaño, Julia Marchetti, Ana Julia Velez Rueda, Pau Bernadó, Martin Blackledge, Tiago N Cordeiro, Eric Fagerberg, Julie D Forman-Kay, Maria S Fornasari, Toby J Gibson, Gregory-Neal W Gomes, Claudiu C Gradinaru, Teresa Head-Gordon, Malene Ringkjøbing Jensen, Edward A Lemke, Sonia Longhi, Cristina Marino-Buslje, Giovanni Minervini, Tanja Mittag, Alexander Miguel Monzon, Rohit V Pappu, Gustavo Parisi, Sylvie Ricard-Blum, Kiersten M Ruff, Edoardo Salladini, Marie Skepö, Dmitri Svergun, Sylvain D Vallet, Mihaly Varadi, Peter Tompa, Silvio C E Tosatto, and Damiano Piovesan. PED in 2021: a major update of the protein ensemble database for intrinsically disordered proteins. *Nucleic Acids Research*, 12 2020.

[134] Fang Xu, Lu Wei, Zhixing Chen, and Wei Min. Frustrated fret for high-contrast high-resolution two-photon imaging. *Optics Express*, 21(12):14097–14108, 2013.

[135] Hagen Hofmann, Andrea Soranno, Alessandro Borgia, Klaus Gast, Daniel Nettels, and Benjamin Schuler. Polymer scaling laws of unfolded and intrinsically disordered proteins quan-

tified with single-molecule spectroscopy. *Proceedings of the National Academy of Sciences of the United States of America*, 109(40):16155–60, oct 2012.

[136] Asaf Grupi and Elisha Haas. Segmental Conformational Disorder and Dynamics in the Intrinsically Disordered Protein α-Synuclein and Its Chain Length Dependence. *Journal of Molecular Biology*, 405(5):1267–1283, feb 2011.

[137] Sharon M Kelly, Thomas J Jess, and Nicholas C Price. How to study proteins by circular dichroism. *Biochimica et Biophysica Acta (BBA)-Proteins and Proteomics*, 1751(2):119–139, 2005.

[138] Zsuzsanna Dosztányi. Prediction of protein disorder based on iupred. *Protein Science*, 27(1):331–340, 2018.

[139] Zsuzsanna Dosztányi, Bálint Mészáros, and István Simon. Anchor: web server for predicting protein binding regions in disordered proteins. *Bioinformatics*, 25(20):2745–2746, 2009.

[140] Alex S Holehouse, James Ahad, Rahul K Das, and Rohit V Pappu. Cider: classification of intrinsically disordered ensemble regions. *Biophysical Journal*, 108(2):228a, 2015.

[141] Karthikeyan Gnanasekaran, HanByul Chang, Paul JM Smeets, Joanna Korpanty, Franz M Geiger, and Nathan C Gianneschi. In situ ni2+ stain for liposome imaging by liquid-cell transmission electron microscopy. *Nano Letters*, 2020.

[142] Eti Malka-Gibor, Micha Kornreich, Adi Laser-Azogui, Ofer Doron, Irena Zingerman-Koladko, Jan Harapin, Ohad Medalia, and Roy Beck. Phosphorylation-induced mechanical regulation of intrinsically disordered neurofilament proteins. *Biophysical journal*, 112(5):892–900, 2017.

[143] Adi Laser-Azogui, Micha Kornreich, Eti Malka-Gibor, and Roy Beck. Neurofilament assembly and function during neuronal development. *Current opinion in cell biology*, 32:92–101, 2015.

[144] Tamara Ehm, Hila Shinar, Guy Jacoby, Sagi Meir, Gil Koren, Merav Segal, Joanna Korpannty, Matthew Thompson, Nathan C. Gianneschi, Michael M. Kozlov, Salome Azoulay-Ginsburg, Roey J. Amir, Joachim O. Rädler, and Roy Beck. Self-assembly of tunable intrinsically disordered peptide amphiphiles. *submitted to PNAS*, 2022.

[145] Marco R Oggioni, Guido Memmi, Tiziana Maggi, Damiana Chiavolini, Francesco Iannelli, and Gianni Pozzi. Pneumococcal zinc metalloproteinase zmpc cleaves human matrix metalloproteinase 9 and is a virulence factor in experimental pneumonia. *Molecular microbiology*, 49(3):795–805, 2003.

[146] David T Jones and Domenico Cozzetto. Disopred3: precise disordered region predictions with annotated protein-binding activity. *Bioinformatics*, 31(6):857–863, 2015.

[147] Michael Schantz Klausen, Martin Closter Jespersen, Henrik Nielsen, Kamilla Kjaergaard Jensen, Vanessa Isabell Jurtz, Casper Kaae Soenderby, Morten Otto Alexander Sommer, Ole Winther, Morten Nielsen, Bent Petersen, et al. Netsurfp-2.0: Improved prediction of protein structural features by integrated deep learning. *Proteins: Structure, Function, and Bioinformatics*, 87(6):520–527, 2019.

[148] Robin Van Der Lee, Marija Buljan, Benjamin Lang, Robert J Weatheritt, Gary W Daughdrill, A Keith Dunker, Monika Fuxreiter, Julian Gough, Joerg Gsponer, David T Jones, et al. Classification of intrinsically disordered regions and proteins. *Chemical reviews*, 114(13):6589–6631, 2014.

[149] Joseph R Luft, Jennifer R Wolfley, and Edward H Snell. What's in a drop? correlating observations and outcomes to guide macromolecular crystallization experiments. *Crystal growth & design*, 11(3):651–663, 2011.

[150] Gary L Gilliland. A biological macromolecule crystallization database: a basis for a crystallization strategy. *Journal of crystal growth*, 90(1-3):51–59, 1988.

[151] Qingbin Meng, Yingying Kou, Xin Ma, Yuanjun Liang, Lei Guo, Caihua Ni, and Keliang Liu. Tunable self-assembled peptide amphiphile nanostructures. *Langmuir*, 28(11):5017–5022, 2012.

[152] Pinaki R Majhi, Paul L Dubin, Xianhua Feng, Xuhong Guo, FAM Leermakers, and Christophe Tribet. Coexistence of spheres and rods in micellar solution of dodecyldimethylamine oxide. *The Journal of Physical Chemistry B*, 108(19):5980–5988, 2004.

[153] Rintaro Takahashi, Theyencheri Narayanan, Shin-ichi Yusa, and Takahiro Sato. Formation kinetics of polymer vesicles from spherical and cylindrical micelles bearing the polyelectrolyte complex core studied by time-resolved usaxs and saxs. *Macromolecules*, 2022.

[154] Sudipto Guha, Sarah L Perry, Ashtamurthy S Pawate, and Paul JA Kenis. Fabrication of x-ray compatible microfluidic platforms for protein crystallization. *Sensors and Actuators B: Chemical*, 174:1–9, 2012.

[155] Georg Pabst, Michael Rappolt, Heinz Amenitsch, and Peter Laggner. Structural information from multilamellar liposomes at full hydration: Full q-range fitting with high quality x-ray data. *Physical Review E*, 62(3):4000–4009, 2000.

Abstract in Hebrew

סיכום

פפטידים לא מקופלים אמפיפיליים (IDPAs) הם סוג מיוחד של מולקולות בעלות פוטנציאל להיות ננו-נשאיות. ה-IDPAs הן שילוב של שרשראות פחממניות שמקורן בשומנים טבעיים ביחד עם פפטידים לא מסודרים שאינם יכולים להתקפל למבנה קבוע במרחב ועוברים בין מספר קונפורמציות לאורך הזמן. המבנה האמפיפילי הזה גורם ל-IDPAs לבצע הרכבה עצמית לפאזה מזוסקופית או להתגבש בתמיסה. מספר האפשרויות להרכבת רצף חומצות האמינו של הפפטיד המחובר לשרשראות הפחמימניות הינו רחב, וקיים מחקר מועט ביותר על השפעת אפשרויות סידור הרצף על המבנים שנוצרים מהרכבה העצמית של מולקולות אלו.

בדוקטורט שלי, למדתי כיצד לפענח את ההשפעה של הרכב הרצף והקונפורמציות ולספק את הבסיס ליישומים עתידיים של IDPAs. חקרתי ארבעה IDPAs שונים עם רצף שונה של חומצות אמינו. השתמשנו ב- SAXS, TEM ובמדידות עכירות על מנת לנתח את המבנה הננוסקופי שנוצר מההרכבה העצמית. הראנו שפרמוטציות (תמורות) והתפלגות המטען החשמלי לאורך הפפטיד משפיעה בצורה ניקרת על הקונפורמציות של קבוצת הראש. כתוצאה מכך, ניתן לקשר מעברי פאזה התלויים ב-pH בין צורות כדוריות, גליליות של מיצלות ופאזות מעובות של משושים לשינוי הרצף של חומצות האמינו. הראנו שאפילו שמוטציה בודדת בחומצת אמינו אחת יכולה לשנות את מעבר הפאזה. לבסוף, הראנו שהמערכת שלנו יכולה לבצע מעברי פאזה עבור IDPAs המסוגלים להחיתך על ידי אינזימים. בסך הכל הראנו ש-IDPAs מאפשרים ישום של אפליקציות רבות עבור מערכות של ננו-חלקיקים שומניים על ידי שילוב של IDPAs עם התכונות המתאימות ובכך להוסיף פונקציונאליות רבה.

עבור רוב הניסויים, השתמשתי בפיזור X-ray מזויות קטנות (SAXS). כדי לאפשר מדידות במספר תנאים עם תא מדידה יחיד, פיתחנו תא מדידה שהודפס באמצעות מדפסת תלת-מימד ועשוי מפלסטיק COC. תא המדידה כולל חלון X-ray עשוי מ-COC שמאפשר רקע SAXS אולטרא נמוך. עיצוב התא מאפשר לבצע מדידות תוך כדי החלפת בופר וספקטרוסקופיית העברה אופטית. לכן תא מדידה זה יישים עבור אפליקציות רבות אחרות. העיצוב כולל ממברנה לצורך ביצוע דיאלזיה עבור דגימה בנפח 100 מיקרוליטר. הדגמנו את תיפקוד תא המדידה על ידי מדידות שונות של מערכת ה-IDPA שלנו ב-pH-ים ומערכות פולימריות שונות כתלות בריכוז המלח. עיצוב התא שלנו מאפשר מדידות במערכות SAXS פרטיות (לא סינכרוטרונים). העיצוב הוכח כיעיל ונמצא בשימוש תמידי במעבדתי ב-LMU עבוד ניסויים תלויי pH.

בפרויקט הדוקטורט שלי, למדתי על הרכבה עצמית של IDPAs הניתנים לשליטה ועל תכונותיהם תחת תנאי סביבה שונים. פיתחנו תא מדידה שהודפס במדפסת תלת מימד שמפאשר מדידות תוך כדי שמירה על ריכוז הדגימה והחלפת בופר (דיאליזה) באותו התא.

הרכבה עצמית של פפטידים אמפיפילים לא מסודרים

חיבור לשם קבלת התואר "דוקטור לפילוסופיה"

מאת

תמרה אהם

בהנחיית

פרופסור רועי בק-ברקאי

פרופסור יואכים רדלר

הוגש לסנאט של אוניברסיטת תל-אביב

יוני 2022